INVESTIGATION OF JAMMING PHENOMENON IN A DRI FURNACE PELLET FEED SYSTEM USING THE DISCRETE ELEMENT METHOD AND COMPUTAIONAL FLUID DYNAMICS

by

John Gregory Rosser

A Thesis

Submitted to the Faculty of Purdue University

In Partial Fulfillment of the Requirements for the degree of

Master of Science in Mechanical Engineering

Department of Mechanical and Civil Engineering

Hammond, Indiana

May 2023

THE PURDUE UNIVERSITY GRADUATE SCHOOL
STATEMENT OF COMMITTEE APPROVAL

Dr. Chenn Zhou, Chair

Department of Mechanical and Civil Engineering

Dr. Harvey Abramowitz

Department of Mechanical and Civil Engineering

Dr. Xiuling Wang

Department of Mechanical and Civil Engineering

Approved by:

Dr. Xiuling Wang

Dedicated to all the people who supported me

ACKNOWLEDGMENTS

I would like to thank my advisor Dr. Chenn Zhou for giving me the opportunity to conduct research at the Center for Innovation through Visualization and Simulation, and for providing me the guidance and necessary resources to complete my project. I would like to thank her for being my professor and serving on my examining committee, along with Dr. Xiuling, and Dr. Abramowitz.

I would also like to express my gratitude to Dr. Tyamo Okosun, Dr. Armin Silaen, and Dr. Orlando Ugarte, for mentoring me, challenging me, and for demanding nothing short of excellence in my work. Likewise, I would like to thank those on the ironmaking committee, particularly Sam Nielson for his consistent technical support and mentorship.

I would like to thank my coworkers for their support and creating a great environment to conduct research in, and the Mechanical Engineering Department at Purdue Northwest for their reliable support during both my undergraduate and graduate studies.

Finally, I want to thank my friends and family for their continual support while completing this extensive program.

TABLE OF CONTENTS

LIST OF TABLES

LIST OF FIGURES

NOMENCLATURE

m_i: mass of particle i

v_i: velocity of particle i

t: time

F_{ij}: contact force between particle i and particle or wall j

F_g: force of gravity

F_n: normal component of the contact force

F_t: tangential component of the contact force

K_n: normal spring stiffness

d_n: normal overlap between two particles

d_t: tangential overlap between two particles

N_n: normal dampening

C_{fs}: static friction coefficient

v_n: velocity in the normal direction

I_i: mass moment of inertia of particle i

ω_i: angular acceleration of particle i

τ_{ij}: torque exerted on particle i from particle j

r_{ij}: radial distance from particle i to j

m_p: mass of particle p

c_p: specific heat

T_p: temperature of particle p

Q_t: rate of convective heat transfer

Q_{rad}: rate of radiative heat transfer

Q_s: other heat sources such as conduction or generation

h: convective heat transfer coefficient

A: area of surface (eq. 8), cross sectional bond area (eqs. 20, 21)

T: temperature of nearby fluid

T_p: temperature of particle

Nu_p: Nusselt number

k: thermal conductivity (eqs. 9, 32), effective thermal conductivity (eqs. 11, 12), turbulent kinetic energy (eq. 34)

D_p: particle diameter

Pr: Prantel number

Re_p: particle Reynold's number

q_{ij}: conduction heat transfer from particle j to i

T_j: temperature of particle j

T_i: temperature of particle i

k_i: thermal conductivity of particle i

k_j: thermal conductivity of particle j

τ_1: Rayleigh wave propagation time

τ_2: impact duration time

τ_3: particle transit time

τ_{scale}: user defined time scale

τ_{max}: maximum DEM timestep

$V_{Rayleigh}$: velocity of the Rayleigh wave

R: particle radius (eqs. 13, 15, 17), bond radius (eqs. 20-24)

ρ: density

E: Young's modulus

v_{impact}: velocity of impact

$v_{particle}$: velocity of particle

υ: Poisson's ratio

$F_{cohesion}$: force of cohesion

R_{min}: minimum radius of particles in contact

W: work of cohesion

δ_m: max shear stress experienced by bond

δ_{max}: limit of max shear stress before failure

σ_m: max tensile stress experienced by bond

σ_{max}: limit of max tensile stress before failure

F_n: normal component of force

F_s: shear component of force

M_s: shear component of torque

M_n: normal component of shear

I: second moment of inertia

J: second polar moment of inertia

F_d: drag force

C_d: drag coefficient

A_p: projected area of particle

v_s: slip velocity

ϵ: nearby void fraction

ζ: unnamed term in Di Felice drag coefficient relation

u_i: velocity of fluid in i direction

u_j: velocity of fluid in j direction

τ: stress tensor

Φ: energy dissipation rate

x_j: position in j direction

F: body force exerted on fluid

g_i: gravitational force in i direction

$\bar{v}$: mean velocity

ε: energy dissipation rate

ε_0: ambient turbulence value

μ_t: turbulent eddy viscosity

σ_ε: model coefficient

σ_k: model coefficient

$C_{\varepsilon 1}$: model coefficient

$C_{\varepsilon 1}$: model coefficient

S_k: user defined turbulent kinetic energy source kinetic term

S_ε: user defined energy dissipation rate source term

P_k: kinetic production

P_ε: dissipation production

f_2: damping function

$C_{\varepsilon 3}$: model constant

T_e: eddy timescale

T_0: timescale associated with ambient turbulence value

f_c: curvature correction value

G_k: turbulent production

G_b: buoyancy production

Υ_M: compressibility modification

S: modulus of the mean strain rate tensor

Bo: bond number

$F_{l,max}$: max total force exerted by liquid on particle

F_w: gravitational force on particle

γ_s: surface tension of liquid

ρ_p: density of particle

g: gravitational acceleration

$c_{p,wet}$: mass weighted average specific heat of a wet pellet

$c_{p,icy}$: mass weighted average specific heat of an icy pellet

$c_{p,water}$: specific heat of water

$c_{p,ice}$: specific heat of ice

$c_{p,modified}$: specific heat of an icy pellet modified to include phase change energy requirement near the melting point

α: moisture mass fraction

v: fluid velocity

μ: kinematic viscosity

X: total moisture percentage in charge

M_{icy}: percent icy pellets in charge

M_{wet}: percent wet pellets in charge

ABSTRACT

An iron ore pellet feed system for a direct reduction ironmaking furnace is jamming during winter operation. The pellets are jamming in a hopper at the top of the feed system above the furnace, and a hot gas, that seals off the furnace flue gas, flows counter to the pellets. A computational model of the feed system is built utilizing the discrete element method and computational fluid dynamics, using Siemen's commercial multiphysics software Star-CCM+, to study the conditions that cause the jam to occur. The study is divided into six parts: pellet bulk flow calibration, computational cost reduction, modeling of the baseline operation, modeling the effect of moisture, development of a thermal model, and investigation of the minimal amount of icy and wet material to jam the system. The findings show that the location of jamming during operation matches the area in the simulation where it is most likely to occur, and that moisture alone is unlikely to result in jamming. Results indicate that the system will jam when charged with a minimum of 15% icy pellets, and when charged with 10% icy together with 5% wet pellets. Experimental work is recommended to validate the findings and to calibrate the simulations accordingly.

1. INTRODUCTION

1.1 Jamming in a Direct Reduction Furnace Pellet Feed System

Direct reduction ironmaking has gained popularity as a low carbon alternative to the typical blast furnace route. A popular method of producing direct reduced iron is through the reduction of iron ore pellets in a reduction shaft furnace. Critical to this process is the use of a reliable continuous pellet feed system to provide a steady flow of pellets to the furnace. Therefore, any disruption in pellet flow can have a significant negative impact on the production rate of iron.

A common problem associated with continuous feed systems is jamming of the material being fed, as is the case for DRI pellet feed systems. Jamming is the obstruction and blockage of material flow, and can be related to various factors such as material properties and operating conditions. Jamming is a complex physical phenomenon and there is an active body of research looking to model and elucidate the mechanisms behind jam formation.

This study aims to investigate the causes of jamming in a Midrex DRI feed system using computational modeling techniques. For the system analyzed, it has been reported by operators that the system jams during freezing winter conditions in a hopper at the top of the feed system where the pellets are charged. Therefore, this study will model baseline operating conditions within the feed system, and attempt to replicate jamming conditions occurring in winter to better understand why the system jams. It is important to note that there is a hot counter-flowing gas that flows through the hopper to seal off the furnace gasses.

The outcome of this study will provide valuable insights to operators of the DRI furnace, and provide key metrics for when jamming is likely to occur. The findings of this study will also provide data for future experimental work to better understand and predict when jamming will occur, ensuring continuous operation of the furnace.

1.2 Literature Review

1.2.1 Demand for Steel and Emission Concerns

Steel is an important component of modern society that has allowed for the development of present-day technologies and standards in transportation, infrastructure, and manufacturing.

However, according to the international energy agency (IEA) the steel industry in 2020 is one of world's largest emitters of carbon dioxide (CO_2), emitting 7% of global CO_2 emissions from the energy system, and consuming 8% of world energy demand [1]. With economic growth continuing globally, the IEA predicts the demand for steel to increase 50% by the year 2050.

The steel making process is a highly carbon intensive process due to the energy requirements and the chemistry involved in the process. Due to concerns about the global environmental impact of CO2 emissions and the expected political actions to reduce emissions such as a carbon tax. The steel making industry is taking measures to lower its carbon footprint.

1.2.2 Steelmaking and Ironmaking process

The primary steel making process starts with collection of iron ore. Iron ore is rock with a high iron oxide content that can be used to produce iron. The iron is extracted from the ore by removing the oxygen from the iron which is termed reduction. Reduction of the iron oxides takes place in the presence of reduction gases when in a high temperature environment. The primary reduction gases are carbon monoxide (CO) and hydrogen (H_2).

The reduction of iron ore typically takes place in a large counter current reactor called a blast furnace. Layered iron ore and coke, which is a porous rock produced from coal that supplies carbon, is charged into the top of a blast furnace and descends downward. Hot reducing gases are supplied in the lower portion of the furnace and flow upward through the solid material. As the coke descends it supplies carbon monoxide which reduces the ore, producing CO_2. The iron oxide is heated and reduced through the furnace until it is liquid iron.

The next step of the process is to remove excess carbon within the liquid iron in a basic oxygen furnace (BOF). The liquid iron is placed in a BOF and oxygen is injected into the iron. The carbon oxidizes forming CO_2 that exits the liquid and the end product is liquid iron with a low carbon content.

The liquid iron is then moved to a ladle furnace where it is reheated by electrodes and the liquid temperature is homogenized through injection of inert gasses. The chemistry of the liquid iron is modified by the removal of impurities and addition of alloy metals until the chemistry matches that of the specific steel quality being produced. At the end of the ladle process the liquid iron and metal alloys have become liquid steel.

The liquid steel is then cooled to a liquid state in a process called continuous casting. The liquid steel is poured into a mold that is cooled by water which hardens the steel into a specified shape. The solidified steel is drawn out and further cooled by spray cooling with water. The solidified steel end product is a homogenous solid steel product.

The solid steel is then reheated in a reheat furnace to increase the steels ductility and prepare the steel to be rolled down to a smaller steel product. Once the steel is rolled down to the desired product size the steel making process is completed.

1.2.3 Direct Reduction Ironmaking and Emissions

The most carbon intensive step of the primary steelmaking process is the separation of iron from iron ore in the blast furnace [2]. Blast furnaces are responsible for ~70% of carbon emissions across the ironmaking process, and typically emit 1.5 kg of carbon per 1 kg of hot metal (liquid iron) [3]. Because of the high amount of CO_2 produced, an alternative ironmaking technique with a lower carbon output called direct reduction ironmaking (DRI) has risen in popularity.

Direct reduction ironmaking is the process of reducing iron ore lumps or pellets using reduction gasses such as CO or H_2. There are two primary types of DRI processes [4]. The first type is a gas-based reactor that uses high CO and H_2 reducing gas generated by reforming a mixture of natural gas and the off gas from the furnace. The two popular technologies using this process are the MIDREX and HYL. The second is a coal/oil-based process that primarily uses coal and sometimes oil and natural gas to generate the reducing gas in a reduction zone of the furnace. Examples of this process are the SL/RN and ACCAR processes. The MIDREX process accounts for 59.9% of world's DRI as of 2021 [5] and is the DRI process that is referenced throughout this review.

Unlike the blast furnace the DRI process does not involve the use of coke or melting of the iron, resulting in a solid iron product rather than hot metal. The solid iron is often charged with scrap into an electric arc furnace, along with scrap steel to produce liquid steel [3]. The product can also be charged into a blast furnace to increase hot metal production and lower coke consumption [6]. Direct reduction ironmaking coupled with the electric arc furnace reduces carbon emissions, producing only 62% the CO_2 that is produced using the blast furnace and BOF [3]. Performing the DRI process with only H_2 as the reductant has been proposed as a method of eliminating CO_2 emissions all together, while still producing a high-quality solid iron product [7].

The MIDREX furnace is a shaft furnace that receives a continuous feed of iron ore pellets through a feed system above the shaft. The ore pellets are charged into a large hopper where they descend at a controlled rate into the furnace. Before the pellets are charged they are stored in an ore field and are exposed to the local weather conditions, which significantly vary by region and time of year. Pellets in some climates are rained and snowed on while in the ore field and are able to hold up to 5.5% their mass in water [8]. The variation in moisture content impacts the heating properties of the pellets, and based on geological studies [9] on wet rocks likely significantly impacts the friction between the pellets. Fines produced by the pellets when wet experience a cohesive force between them due to the surface tension strength of the water being significant relative to their weight and size, and thus have a reduced flowability [10]. Pellets that are wet and exposed to freezing conditions may freeze together and form clumps.

Continuous solid material feed systems are, in general, prone to jamming of the flow, which for a DRI furnace greatly disrupts furnace operation. Jamming of iron ore pellets within the hopper is reported to be a recurring problem during the winter months for midwestern steel plants. In the Midwest, winter months can experience significant precipitation and average temperatures below 0 Celsius [11].

1.2.4 Hopper Use and Clogging Dynamics

The granular flow of bulk materials through a hopper at a controlled rate is a common situation found in multiple industries including the powder, chemical, agricultural, and steel industries. Hoppers vary significantly in their shape and size ranging from a few milliliters to thousands of liters [12]. They are used in multiple ways including for storage, as feed systems, or for transportation [12]. Hopper design is of great importance to ensure a controlled rate of flow of material, and to ensure that the material flow rate distribution inside the hopper is such that the material exits in a desired manner.

Granular flow through hoppers is classified into two flow patterns [13]. The first pattern is called funnel flow and is characterized by the flow of material along the centerline and out the hopper with stagnant material towards the walls of the hopper. The stagnant material in the hopper stays entrapped in the hopper until the material along the centerline of the hopper leaves, creating a first in last out effect [13]. The second flow pattern found in hopper flow is called mass flow. Mass flow is characterized by motion of the entire bed descending down and out of the hopper.

Unlike funnel flow, mass flow does not contain any entrapped material and has a first in first out effect [13]. The factors that are understood to contribute to which flow pattern takes place are the friction between particles, friction between the particles and the hopper walls, and the geometry of the hopper [12].

A problem commonly found in industry with granular flow through hoppers is jamming or clogging that stops the flow of material and interrupts operations. To mitigate this problem various anti-clogging devices have been developed but there is no good way to avoid clogging entirely [14]. Jamming in hoppers is therefore often studied in terms of the probability that a flow will jam [15]. Jamming is a complex problem and the factors that impact jamming probability have been found to include: particle size and granular characteristics [16], particle shape and roughness [17-20], outlet type [21-23], outlet size [24, 25], silo geometry [26-28], and packing of particles [29]. In some studies, the probability of jamming in a hopper is assumed to be constant independent of the number of particles remaining in the hopper [30-32]. This is because Janssen showed in his research that when the number of particles in a hopper is sufficiently large the pressure on the bottom walls of the hopper remains constant independent of the filling height [33]. This phenomenon has been coined the "Janssen effect". When the pressure is constant due to the Janssen effect the frictional forces between the particles and walls become constant. In Park's research it is seen that in cases where the number of particles in a hopper is smaller, and below the critical fill height where the Janssen effect takes over, the probability of jamming is positively correlated to the pressure around the hopper outlet [15].

Xiao's research showed that the way in which particles flowing through a bottleneck transition from flowing to jammed is by formation of an arch around the outlet [14], and Park's research showed that an increase in pressure around the hopper outlet increases the probability of arch formation [15]. When particles are flowing out the hopper there is a region near the outlet with large kinematic fluctuations among the particles that is referred to as the dynamic arch [14]. Xiao identified two clogging mechanisms in relationship to the dynamic arch [14]. The first mechanism is found to be through collision dissipation, and is mainly affected by the dynamic characteristics above the outlet. The primary factors contributing to this mechanism of clogging are the geometry of the outlet structure and the outlet size. The second mechanism is not related to the dynamic conditions of the particles near the outlet, but instead related to the particle properties and the packing fraction [14].

A unified theory of jamming posed by Lu posited that the state variables that govern an isothermal state of jamming are the pressure, shear rate, and the free volume [34]. The isothermal property of the material is in reference to a non-thermal temperature, essentially describing the "fluffiness" of the mixture. Lu's work agrees with other studies on clogging through hoppers in that he identified the pressure as an important factor in predicting jamming [15]. The shear rate may agree with studies that have identified interparticle and particle-wall friction coefficients as important in predicting flow type and jamming [17-20]. Also, the free volume is likely in agreement with studies showing that the volume fraction of the flowing particles is an important parameter in the whether or not a granular flow will jam [29].

1.2.5 Discrete Element Method Research

As computational power has increased the number of computer-based simulations of granular flow has also increased. A common way to simulate the dynamics of granular materials is by use of the discrete element method (DEM). The Discrete Element Method is a numerical method that models individual particles, tracking their position, orientation, movement, and interactions with other particles and objects. This is accomplished by performing a force balance on each discrete particle, applying the laws of motion described by Newton and the laws of rotational motion described by Euler [35].

Because DEM computationally tracks the dynamics of individual particles it allows for gathering of metrics that are difficult or even impossible to obtain via experimental procedures [12, 36-38]. For example, Natsui modeled the behavior of fines within a blast furnace [37], a place that is particularly difficult to obtain measurements. He was able to show fine distribution within the furnace, along with the stresses and the void fraction within the clusters of fines. Further, pressure drop calculations using the void fractions yielded results in agreement with experimental results. It is also often the case that it is far more cost effective to perform simulations rather than experiments.

Specifically, with regard to granular flow through hoppers, DEM has been successfully used to predict the mass flow index of different materials and validated against Jenki charts [12, 26]. Not only does this validate the use of DEM for simulating the bulk flow behavior of particles in granular flows, but it provides further value in that the simulations can be used to gather data relevant to hopper flow that would otherwise be difficult to obtain experimentally.

Because of the ability for DEM to describe individual particle metrics, it has also been used to investigate what parameters are relevant in clogging phenomenon [14]. Studies using DEM have been performed investigating how arch formation takes place and what parameters are important in predicting arch formation [15]. Discrete Element Modeling is further used to determine the probability that a flow will jam. [15].

A limitation in using DEM simulations is that it is computationally expensive [36], this constraint limits the size of the simulation and number of particles. Physical parameters can be changed to cut computational expense, but the bulk flow of the particles need to be calibrated such that the simulation results match experimental results [36, 37]. It is commonly the case that the geometry of the particles is approximated as perfectly spherical which is not the case in many physical situations, therefor contact parameters, such as interparticle rolling and sliding friction coefficients, need to be calibrated such that the simulated bulk flow matches experimental bulk flow [37].

Coupled Computational Fluid Dynamics and Discrete Element Method

Two phase flows containing a granular flow and a fluid flow can be modeled by using DEM coupled with Computational Fluid Dynamics (CFD) to simulate a fluid flow field that effects the particles and vice versa. This can be accomplished using a technique referred to as two-way coupling. Two-way coupling is when mass, momentum, and energy are exchanged between the CFD flow field and the DEM particles during simulation and is often important in describing the flow field state when there is a large amount of particles present [38].

One limitation in the use of DEM-CFD coupling is that in order to fully resolve the fluid flow field between particles a high number of cells per particle need to be present to capture the boundary layer details between the particles, which in most instances is prohibitively computationally expensive [39]. Another limitation is that the CFD domain's mesh cell size should be larger than the largest particle size [40], this is so that a cell is not completely covered by a particle which would prevent solving of the fluid equations in that cell. These limitations result in a course mesh for the fluid domain.

Despite these limitations two-way coupled DEM-CFD simulations have been successful in describing granular and fluid flow dynamics, heat and mass transfer, and chemical reactions when compared to experimental results [39, 41-43]. A study by Che et al., showed that two-way coupled

DEM-CFD is able to replicate the dynamics of non-spherical particles flowing in a spouted bed by replicating experimental data gathered by tracking the particles [41]. To better elucidate the mechanisms of heat transfer between particles in a fluidized bed, Wang et al. used the two-way coupled method and found that heat transfer is dominated by particle fluid convection while conduction is negligible [42]. They validated their model against experimental results found in the literature, [42, 44] showing that the rate and mode of heat transfer could accurately be modeled. Kinaci et al. used two-way coupling to model the direct reduction of iron in a fluidized bed accounting for mass, momentum, and energy exchange between the gas and iron ore particles. The simulation results showed that the degree of reduction and the time to reduction agreed with experimental data, and that the rate limiting step agreed with other literature results [39].

Discrete Element Method for Ice Break Up Modeling

The discrete element method is capable of modeling bonding between particles and allows for controlling of the bond strength by defining the tensile and shear strength of the bond. This technique has been used to accurately capture the physics of ice break up [45]. De et al., performed a study modeling the forces required to break up arctic sheet ice using multiple sloped cone surfaces and the results were validated against ISO sea ice force standards [45]. The same technique has been used by Jou et al. to investigate ice breaking by icebreaker ships and concluded that the bonded DEM model can be used to accurately describe complex ice fracture phenomenon [46].

Given the success of DEM coupled with CFD in modeling bulk granular flow, clogging dynamics, and ice breakup, along with the exchange of mass, momentum, and energy, and given its previous use in DRI and blast furnace modeling, DEM is presumed to be an appropriate tool for investigating the reasons for why clogging is occurring during winter months in a DRI feed system.

2. METHODOLOGY

The study is divided into 6 distinct smaller studies to model the flow of iron ore pellets in a DRI feed system, and investigate why jamming of the material is occurring. The first is the calibration study, where the bulk flow of the pellets in the simulation is calibrated to that which is observed in experimental results. The second is the computational expense study, where the pellet parameters are parameterized to reduce the computational expense while maintaining the relevant bulk flow characteristics. The third is the baseline case study where the normal operation of the feed system is modeled and important flow metrics are measured. The fourth is the moisture/high friction study, where the baseline case is run with much higher friction between the particles to determine if the higher friction due to moisture content causes jamming. The fifth is the development of a thermal model, and testing of that model on multiple small test cases, for the implementation in the feed system model to capture the freezing and heating of the pellets. The sixth is the minimum icy material study, where the amount of icy/wet material is parameterized to determine the minimal amount to jam the system.

Presented in the following sections is the background, methodology, results, and conclusions for each of the six distinct parts of this study, along with any other necessary information. At the end of the six sections a final discussion and conclusions section is presented.

Exact values for pellet size distributions, geometry dimensions, and operational gas and pellet flow rates and temperatures are not disclosed in this thesis.

3. COMPUTATIONAL MODELS

3.1 Discrete Phase

The Hertz-Mindlin contact model is used to calculate the normal and tangential components of the forces acting on each particle. The normal and tangential components of each force acting on a particle are modeled as a pair of spring-dashpot oscillators, shown in figure 1. The spring accounts for the elastic component and the dashpot accounts for the energy dissipating component of a collision. The normal component of the force is calculated using Hertz's contact theory while the tangential is using Mindlin's no-slip model.

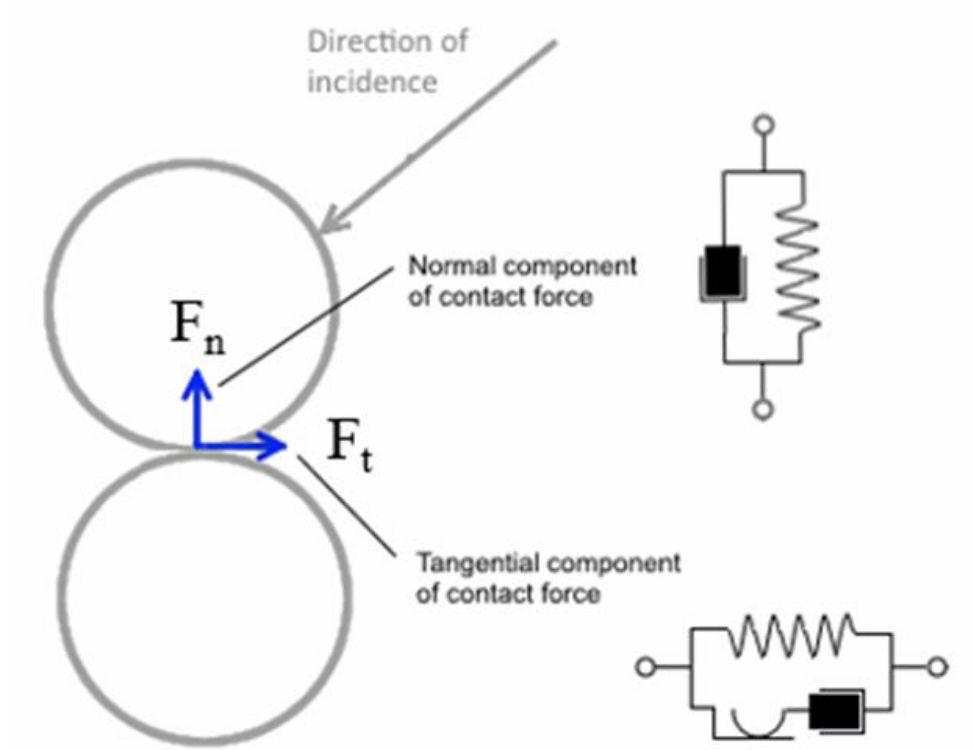

Figure 1. Normal and Tangential Components of the Force during Particle collision [47]

Conservation of momentum is applied to each particle given as:

$$m_i \frac{dv_i}{dt} = \sum_j F_{ij} + F_g \tag{1}$$

Where subscript i represents particle i and subscript j represents particles or wall in contact with particle i. Variables m_i and v_i represent the mass and velocity of particle i respectively, F_g represents the force of gravity applied to particle i, and F_{ij} represents the contact force between particle i and particle or wall j, and is given as:

$$F_{ij} = F_n + F_t \tag{2}$$

Where F_n and F_t are the normal and tangential forces shown in figure x, and are equal to:

$$F_n = -K_n d_n - N_n v_n \tag{3}$$

$$F_t = \frac{|K_n d_n| C_{fs} d_t}{|d_t|} \tag{4}$$

Where d_n and d_t are the normal and tangential overlaps of the particles, respectively. K_n and N_n are the normal spring stiffness and the normal damping, respectively, and C_{fs} is the static friction coefficient.

The particles are free to rotate and thus the conservation of angular momentum is also applied as:

$$\frac{d}{dt} I_i \omega_i = \sum_j \tau_{ij} \tag{5}$$

The terms I_i and ω_i are the mass moment of inertia and the angular velocity respectively, and the term τ_{ij} is the torque given as:

$$\tau_{ij} = r_{ij} F_{ij} \tag{6}$$

Where r_{ij} is the distance from the center of particle i to point of contact with j.

Conservation of energy is applied to each particle with the general equation of the form:

$$m_p c_p \frac{dT_p}{dt} = Q_t + Q_{rad} + Q_s \tag{7}$$

Where m_p is the mass of the particle, c_p is the specific heat, $\frac{dT_p}{dt}$ is the time rate of change of the particle temperature, Q_{rad} the rate of radiative heat transfer, and Q_s is other heat sources such as conduction or heat generation. The rate of convective heat transfer is Q_t and given as:

$$Q_t = hA\left(T - T_p\right) \tag{8}$$

With A as the surface area of the particle, T and T_p as the local continuous phase and particle temperature, respectively, and h as the heat transfer coefficient. The heat transfer coefficient for each particle is solved for by calculation of the particle Nusselt number relation which is defined exactly as:

$$Nu_p \equiv \frac{hD_p}{k} \tag{9}$$

With D_p representing the particle diameter and k the thermal conductivity of the fluid phase. The Nusselt number relation chosen for granular flow is:

$$Nu_p = 2.0 + 1.2{Re_p}^{1/2}Pr^{1/3} \tag{10}$$

This specific Nusselt number relation has been used in simulations to study fluidized and packed bed convective heat transfer and produce validated results [48].

Heat transfer due to radiation in a packed bed of spheres has been shown to be very low when the sphere temperature is below 100°C [48]. Because gas temperatures are below freezing and gas temperatures are not above 100°C in this study the radiative heat transfer is neglected and no radiation model is applied.

Heat exchange between the particles in the form of conduction is defined as:

$$q_{ij} = 4r_c k\left(T_j - T_i\right) \tag{11}$$

Where q_{ij} is the heat transfer from particle *j* to *i*, r_c is contact area radius, k is the equivalent thermal conductivity, and T_j and T_i are the temperatures of particle *j* and *i* respectively. The equivalent thermal conductivity between particle *j* and *i* is defined as:

$$\frac{1}{k} = \frac{1}{k_i} + \frac{1}{k_j} \tag{12}$$

With the thermal conductivity of particles *j* and *i* denoted as k_j and k_i respectively.

The DEM time-step is determined from the minimum of three time-step criterion, the Rayleigh wave criterion, the impact duration criterion, and the particle transit time. Each criterion is applied to ensure that the time step enables the simulation to capture an aspect of the particle movement and interactions.

A Rayleigh wave is an undulating wave that travels across the surface of a solid. The timestep required to model particle interactions is constrained by how long it takes for a Rayleigh wave to travel from one end of a particle's surface to the other and affect the surrounding particles. Assuming the particles are perfectly spherical the Rayleigh wave propagation time is given as:

$$\tau_1 = \pi \frac{R}{V_{Rayleigh}} \tag{13}$$

The velocity of the Rayleigh wave is denoted as $V_{Rayleigh}$. The Rayleigh wave timestep criterion is:

$$\tau_{max} < t_{scale}\tau_1 \tag{14}$$

The multiplier t_{scale} is a user defined time scale used to control the time step.

The duration of the impact of two perfectly elastic particles is another constraint on the DEM time-step as the time step needs to be able to capture the duration of the collisions. Using the Hertz contact theory the impact duration criterion is:

$$\tau_2 = 2.94\left(\frac{5\sqrt{2}\pi\rho}{4}\frac{1-v^2}{E}\right)^{0.4}\frac{R}{\sqrt[5]{v_{impact}}} \tag{15}$$

The density, Young's modulus, Poisons ratio, particle radius, and impact velocity are assigned as ρ, E, v, R, and v_{impact}, respectively. The time step criterion based on the impact duration is:

$$\tau_{max} < 0.1\tau_2 \tag{16}$$

Another limitation on the DEM timestep size is the particle transit time. It is assumed that the particles should not move excessively in a time step. This assumption ensures that particle contacts are detected and interactions are captured. The timestep is limited such that a minimum of 10 timesteps are required for the particle to travel the distance of its radius.

$$\tau_3 = \frac{R}{v_{particle}} \tag{17}$$

With the time step criterion being:

$$\tau_{max} < 0.1\tau_3 \tag{18}$$

The final particle time step is the minimum of the calculated time step criterion: t_{scale} τ_1, $0.1\tau_2$, $0.1\tau_3$.

The modeling of interparticle cohesive forces introduces an attractive force between the particles. The appropriate variant of the cohesive force model used is the JKR model. The JKR model limits the cohesive force between particle to those that are in direct contact and is given as:

$$F_{cohesion} = R_{min}W\pi\frac{3}{2} \tag{19}$$

Where W is the work of cohesion and R_{min} is the minimal radius of the particles in contact.

The bond model is a model that defines a bond between two particles when they come into contact, and is capable of tracking the tensile and shear forces that the bond experiences. The bond tensile and shear stresses are calculated assuming that the bond is a massless circular cross-sectional beam between the particles that is capable of transmitting force and torque to the particles, shown in figure 2.

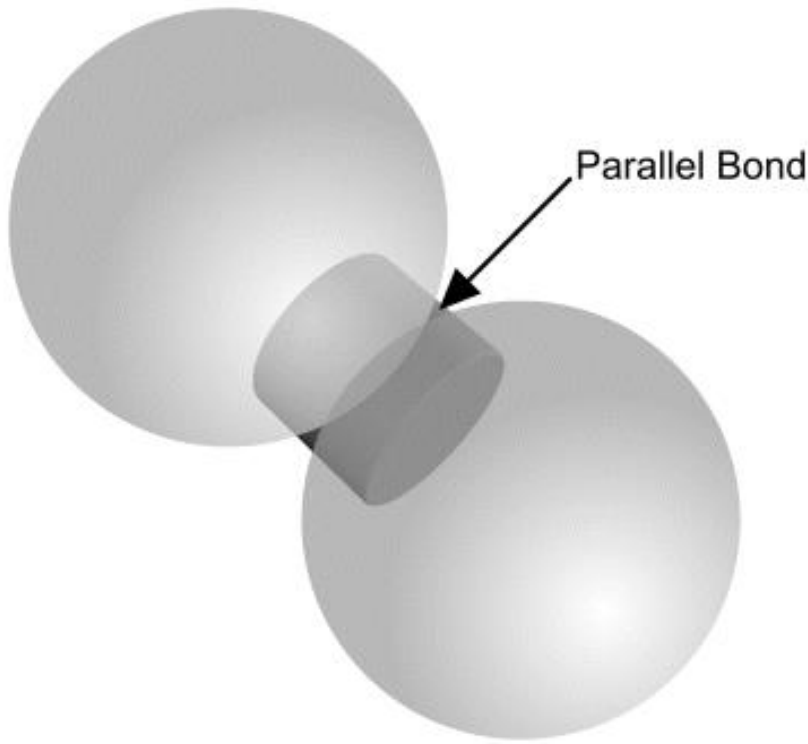

Figure 2. Parallel bond between two particles in contact [47]

The maximal tensile stress the bond experiences is:

$$\delta_m = \frac{-F_n}{A} + \frac{|M_s|R}{I} \tag{20}$$

The maximal shear stress the bond experiences is:

$$\sigma_m = \frac{|F_s|}{A} + \frac{|M_n|R}{J} \tag{21}$$

With F_n and M_n as the normal components of force and torque, respectively, and F_s and M_s as the shear components of the force and torque, respectively. The radius is defined as R, and the area, second moment of area, and second polar moment of area are denoted as A, I, and J respectively and defined as:

$$A = \pi R^2 \tag{22}$$

$$I = \frac{1}{4}\pi R^4 \tag{23}$$

$$J = \frac{1}{2}\pi R^4 \tag{24}$$

Failure occurs when the tensile or shear stress surpass a defined maximal strength:

$$\delta_m > \delta_{max} \text{ or } \sigma_m > \sigma_{max} \tag{25}$$

The drag force on the particles are modeled using the Di Felice drag coefficient method. The method accounts for the drag effect of particles being near each other. The drag force is defined as:

$$F_d = \frac{1}{2} C_d \rho A_p |v_s| v_s \tag{26}$$

The drag coefficient for the Di Felice method is defined as:

$$C_d = \left(0.63 + \frac{4.8}{\sqrt{\epsilon Re_p}}\right)^2 \epsilon^{2-\zeta} \tag{27}$$

$$\zeta = 3.7 - 0.65 exp\left[-0.5\left(1.5 - log\left[\epsilon Re_p\right]\right)^2\right] \tag{28}$$

With the void fraction near the particle defined as ϵ.

3.2 Continuous Phase

The fluid phase in the simulations is modeled using CFD. For each simulation the principles of mass and momentum conservation are applied to the continuous phase, and phase state is solved for using a coupled implicit scheme. For simulations where the heat transfer between the solid and gas phases are simulated the energy conservation principle is also applied.

Mass Conservation:

$$\frac{\partial \rho}{\partial t} + \nabla.(\rho u_i) = 0 \tag{29}$$

Momentum conservation:

$$\frac{\partial}{\partial x}(\rho u_i) + \nabla.(\rho u_i u_i) = -\nabla_p + \nabla.(\tau) + \rho g_i + F \tag{30}$$

With the stress tensor defined as:

$$\tau = \mu\left(u_i u_j + u_i u_j^T\right) - \frac{2}{3}\nabla.u_i I \tag{31}$$

Energy conservation:

$$\rho c \frac{DT}{Dt} = k\nabla^2 T + \Phi \tag{32}$$

With energy dissipation rate defined as:

$$\Phi = \mu\left(\frac{\partial u_i}{\partial u_j} + \frac{\partial u_j}{\partial u_i}\right)\frac{\partial u_i}{\partial x_j} \tag{33}$$

The turbulence model used is the realizable k-epsilon model. The k-epsilon turbulence model has been shown to be suitable for modeling flow through a packed bed in CFD-DEM coupled simulations [49]. The k-epsilon model represents turbulence by means of two transport equations. The first transport equation is denoted k and represents the turbulent kinetic energy, while the second is ε and represent the dissipation of the kinetic energy.

k-equation:

$$\frac{\partial}{\partial t}(\rho k) + \nabla.(\rho k \bar{v}) = \nabla.\left[\left(\mu + \frac{\mu_t}{\sigma_k}\right)\nabla k\right] + P_k - \rho(\varepsilon - \varepsilon_0) + S_k \tag{34}$$

ε-equation:

$$\frac{\partial}{\partial t}(\rho \varepsilon) + \nabla.(\rho \varepsilon \bar{v}) = \nabla.\left[\left(\mu + \frac{\mu_t}{\sigma_\varepsilon}\right)\nabla \varepsilon\right] + \frac{1}{T_e} C_{\varepsilon 1} P_\varepsilon - C_{\varepsilon 2} f_2 \rho \left(\frac{\varepsilon}{T_e} + \frac{\varepsilon_0}{T_0}\right) + S_\varepsilon \tag{35}$$

The terms P_k and P_ε are the kinetic and dissipation production, respectively defined as:

$$P_k = f_c G_k + G_b + \Upsilon_M \tag{36}$$

$$P_\varepsilon = f_c S k + C_{\varepsilon 3} G_b \tag{37}$$

Where the terms G_k, G_b, and Υ_M are the turbulent production, buoyancy production, and the compressibility modification, respectively.

4. BULK FLOW CALIBRATION

4.1 Background

Iron ore pellets are typically in the shape of irregular spheres. For modeling using DEM the ore pellets are modeled as perfect spheres. This is an idealization of the pellet shape that is necessary so that the simulation is not too computationally expensive.

Simulations using the idealized sphere shape change the bulk flow characteristics of the pellets when compared to experimental results. This is because the geometries of the individual pellets are not accounted for during collisions. To overcome the change in bulk flow behavior the contact variables need to be parameterized such that the bulk flow matches experimental results.

Experimental results measuring the repose angle of iron ore after it is dropped have been previously published by Li et al [50]. The repose angle is the angle that a material is stably piled or stacked without collapsing due to the force of gravity. Li's work compared DEM simulation results to experimental results and found that the repose angle is dependent on the kinetic energy dissipation rate of the pellets, and that the kinetic energy dissipation rate is directly related to the sliding and rolling coefficients. This work found that the friction coefficients could be modified to match the experimental bulk pellet behavior.

4.2 Methodology

To calibrate the bulk flow behavior of iron ore pellets a drop test set up was created in STAR CCM+ to match that of the experimental set up performed by Li et al, shown in figure 3.

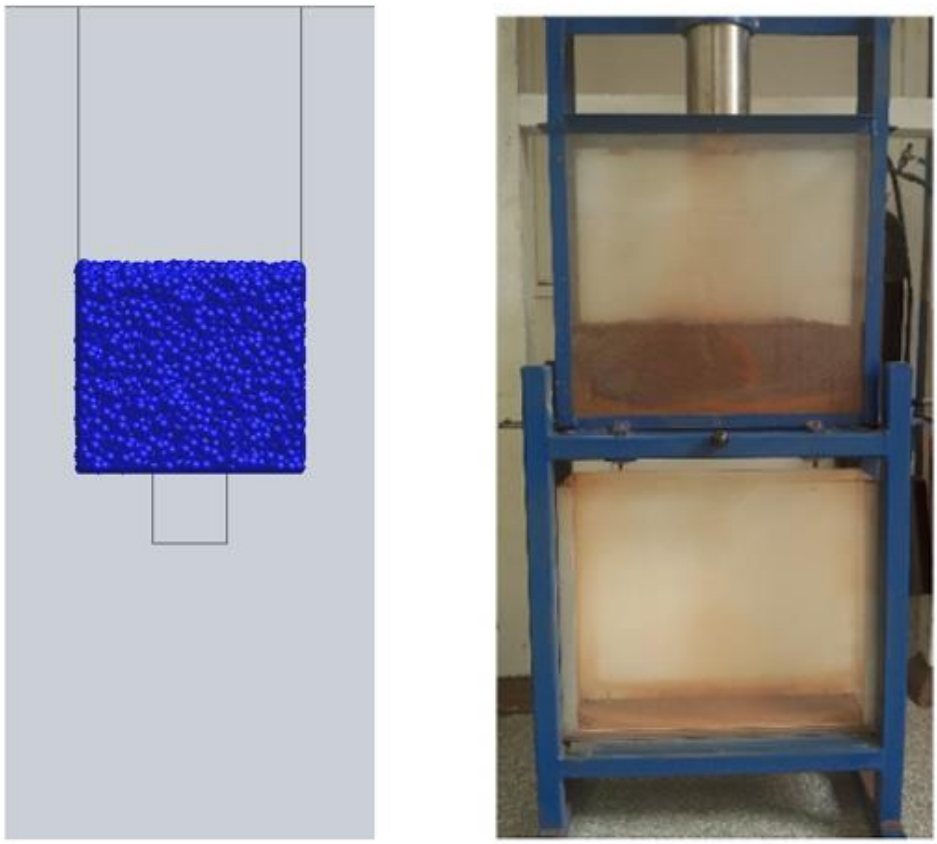

Figure 3. Drop test with blue pellets (left) and experimental set up performed by Li et al. [50] (right)

The test is replicated by first charging the upper portion of the drop test with pellets with the drop door set as a wall boundary. To begin the drop, the drop door is changed from a baffle boundary to an internal interface boundary allowing the pellets to freely flow through. When the pellets are settled at the bottom of the domain the repose angle is measured, the steps of the process are shown in figure 4.

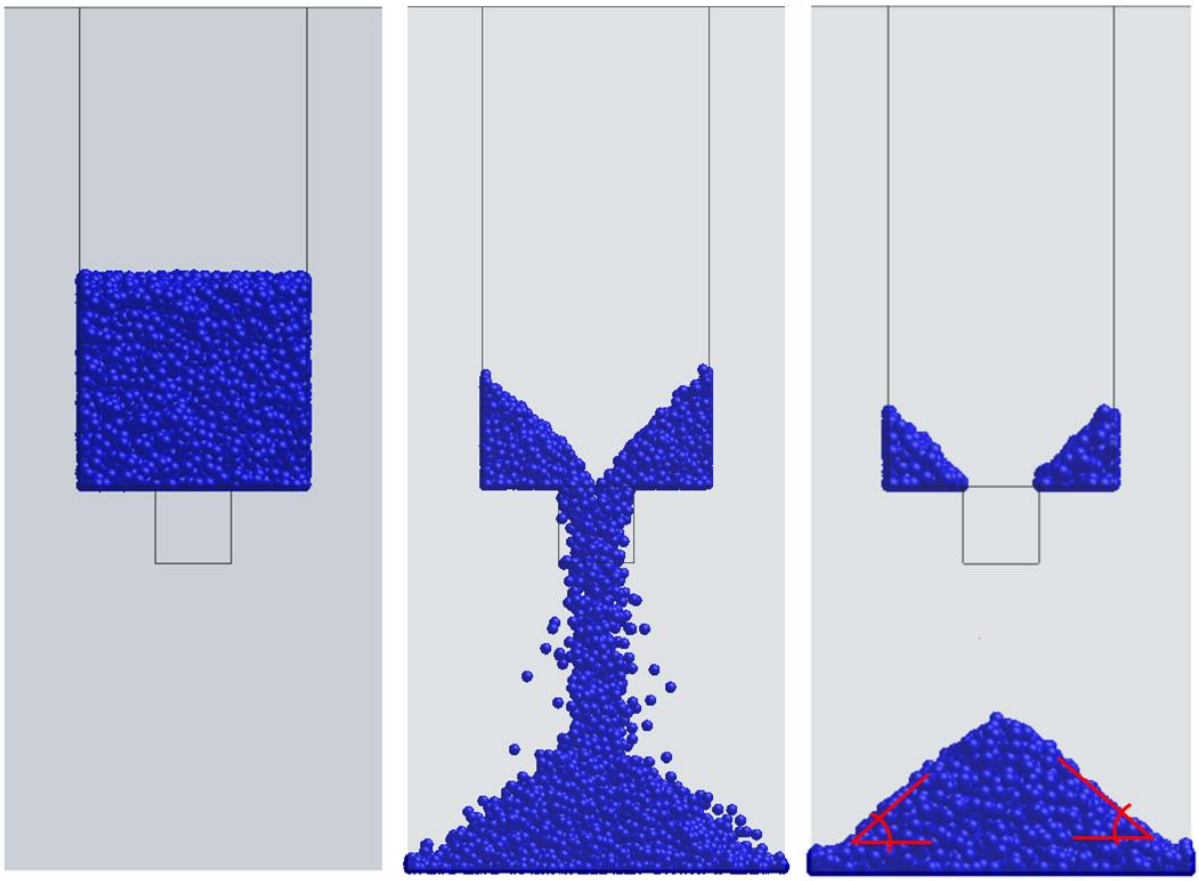

Figure 4. Pellets charged into domain with door closed (left), door opened and pellets free to drop (middle), end of test with pellets repose angles shown

The test is performed varying the static and rolling friction parameters until the slope of the repose angle matches the experimental results. Once the results match, the test is repeated 5 times, and the 5 left and right angle of repose results are averaged. This is done for 3 different pellet sizes, 5.5, 7, and 9mm, and compared against the experimental results. If the angle of repose is within 1 degree the bulk motion of the pellets is considered validated.

4.3 Computational Domain

The dimensions of the dropping region match the experimental set up and are shown in figure 5. A mesh with a cell size of 0.01 m and containing 9256 elements was generated for the domain. The mesh and boundary conditions are shown in figure 6.

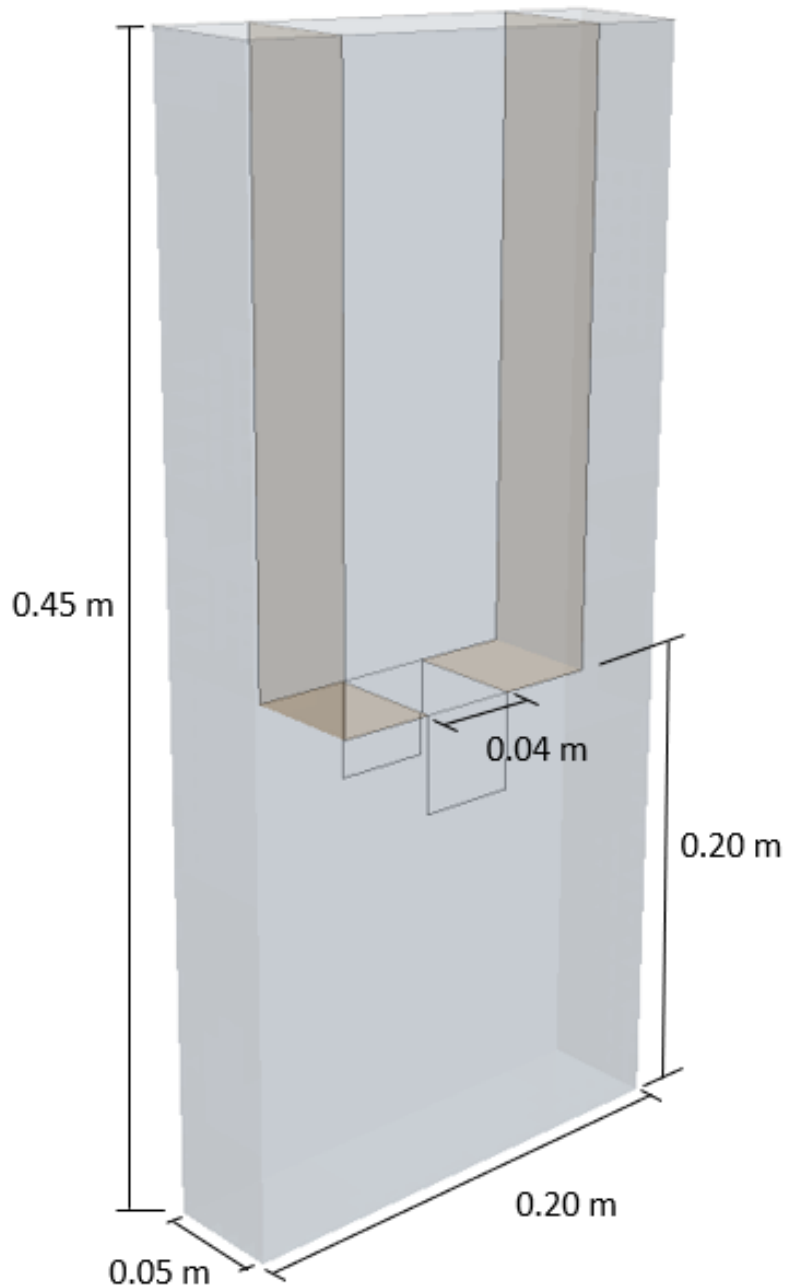

Figure 5. Dimensions of drop test domain

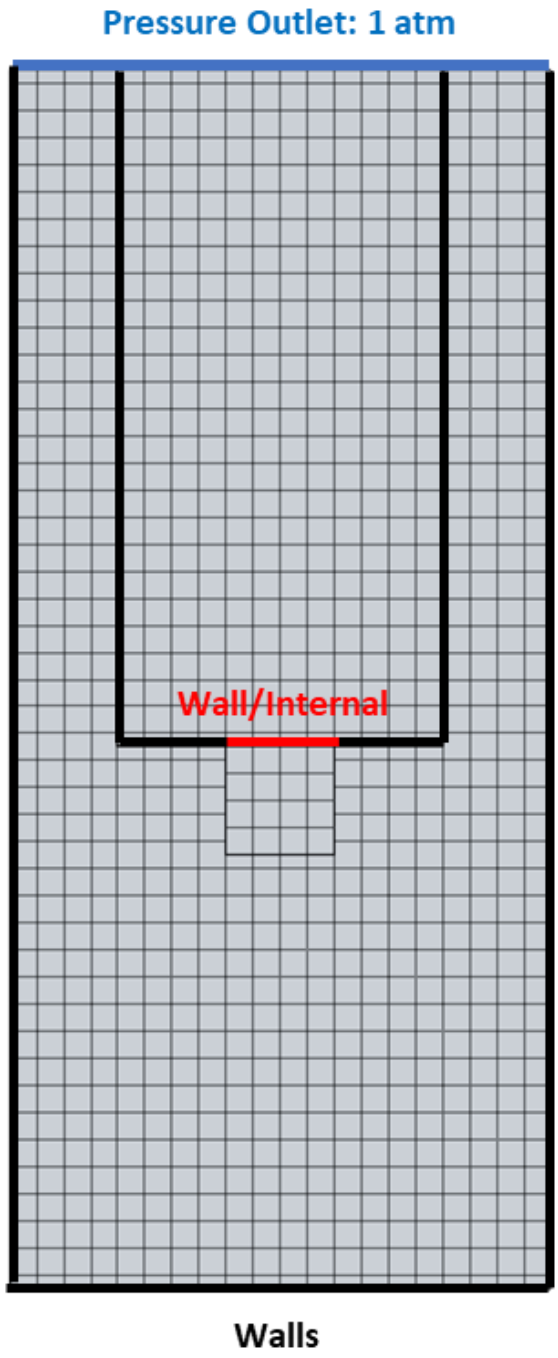

Figure 6. Mesh and boundary conditions

4.4 Pellet Material Properties

The gas phase is air with a density of 1.18 kg/m^3 and dynamic viscosity of 1.855E-5 Pa-s. The pellet material properties and pellet contact parameters used are shown in tables 1 and 2 respectively.

Table 1. Iron ore pellet material properties

Iron Ore Pellet Material Properties	
Property	**Value**
Poisson's Ratio	0.25
Young's Modulus	40 MPa
Density	3948 kg/m^3

Table 2. Pellet contact parameters

	Pellet-Pellet	**Steel-Pellet**
Coefficient of Static Friction	Varied	varied
Coefficient of Rolling Friction	Varied	varied
Coefficient of Restitution	0.48	0.39

4.5 Results

The friction parameters that were found to result in accurate repose angles when implemented are shown in table 3.

Table 3. Static and rolling friction coefficients that resulted in accurate repose angles

	Pellet-Pellet	**Steel-Pellet**
Coefficient of Static Friction	0.50	0.40
Coefficient of Rolling Friction	0.20	0.25

The pellet sizes simulated and the corresponding average left and right repose angles are shown in table 4 along with the experimental repose angles.

Table 4. Pellet size and average left and right repose angles for 5 drops

	Experiment		**Simulation**	
Diameter (mm)	**Left**	**Right**	**Left**	**Right**
5.0	36.66	36.48	---	---
5.5	---	---	37.03	36.84
7.0	34.96	34.75	34.94	35.69
9.0	33.55	33.39	33.19	33.12

The average left and right-angle results are plotted against the experimental results in figures 7 and 8, and are within 1 degree of the experimental results, showing agreement between the experimental and simulation results.

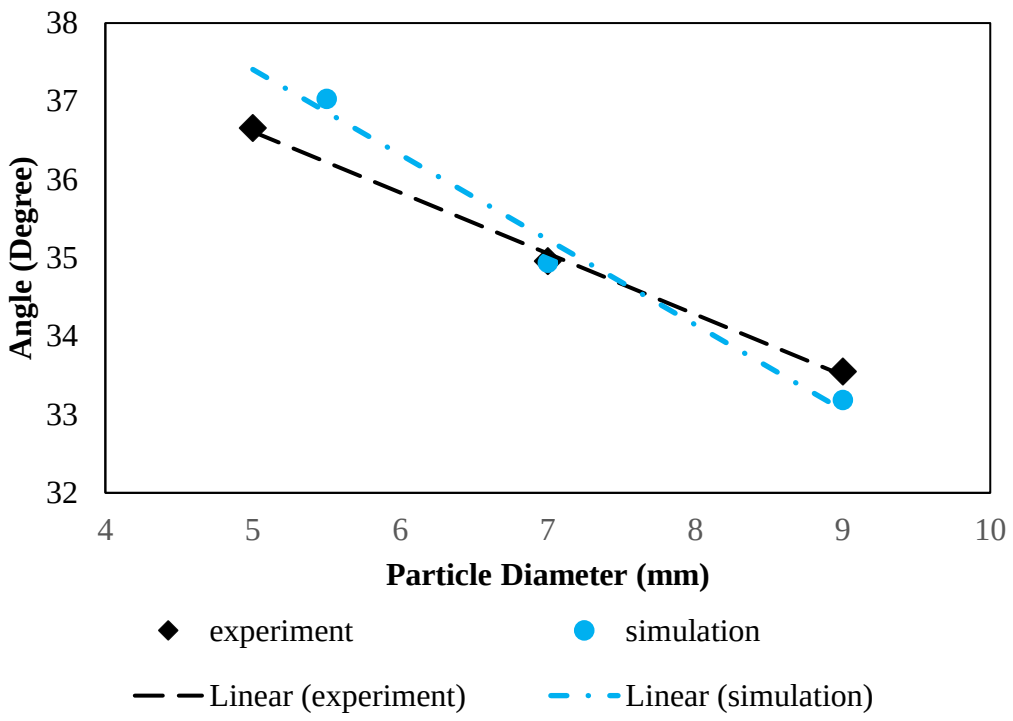

Figure 7. Left angle of repose vs particle size

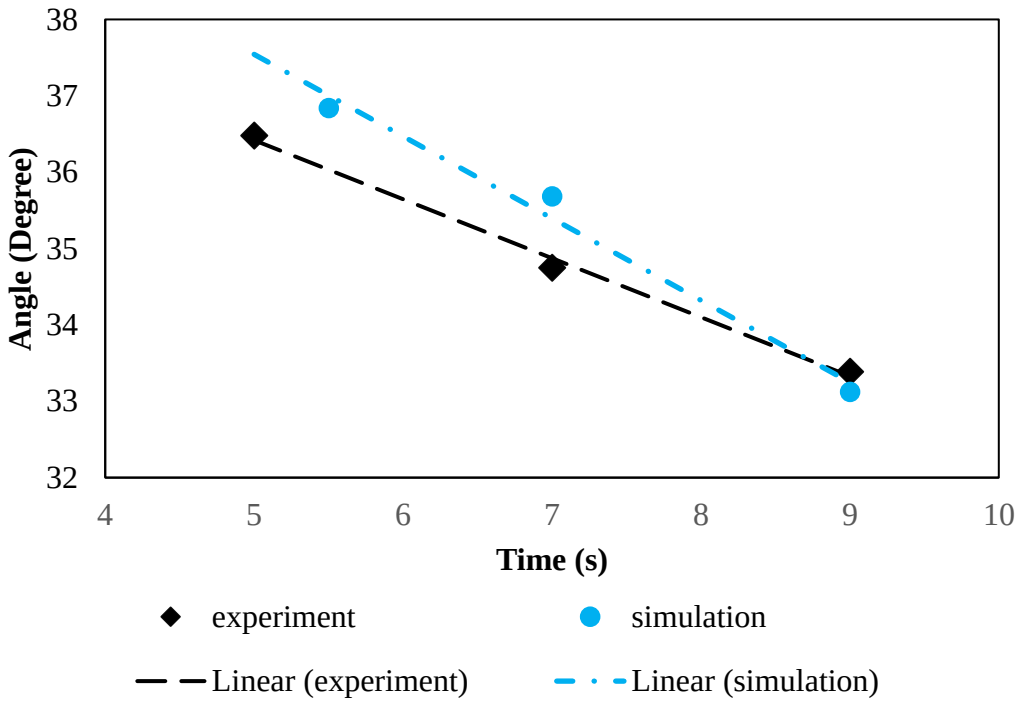

Figure 8. Right angle repose angle vs particle size

4.6 Discussion

To model the motion of iron ore pellets in a DRI feed system using DEM, perfect spheres are used in place of the individual irregular geometries of the pellets. A limitation of using perfect spheres is that the impact of individual pellet geometries during pellet collisions are not accounted for. To overcome this limitation, the bulk flow is calibrated against experimental results by modifying the static and rolling friction coefficients.

Using a static friction coefficient of 0.5 and a rolling friction coefficient of 0.2, the simulated angle of repose agrees with experimental results, suggesting that the pellet contact parameters are calibrated so that the bulk flow behavior of the pellets is represented, validating the bulk flow behavior of the pellets.

The bulk flow behavior of the pellets is important to accurately represent, in order to model the DRI feed system, and for capturing why jamming of the material may be occurring. The angle of repose after a drop test describes the energy dissipation of the pellets and how the pellets stably stack under the force of gravity, therefore the pellets are calibrated against this parameter. The pellet friction parameters are used for all of the following sections to ensure proper bulk flow behavior of the pellets.

5. COMPUTATIONAL COST REDUCTION

5.1 Background

When simulating a large number of particles using DEM computational cost becomes a limiting factor in the feasibility of a given simulation. This is because DEM models the position, orientation, contacts of, and the forces acting on the particles. The primary method of reducing the computational cost of a DEM simulation with a large number of particles is to reduce the number of particles while maintaining relevant the bulk flow characteristics of the flow. The ways in which this is accomplished include increasing the particles size, changing the particle size distribution, and modeling only portions of the domain that are of interest.

It is important when changing parameters of the particles and domain of the simulation to ensure that the new bulk flow characteristics of the flow match that of the original bulk flow. For jamming the bulk flow characteristics that are important are maintaining the void between the particles and their velocity.

5.2 Methodology

A small axisymmetric conical hopper geometry is created and charged completely with iron ore pellets, shown in figures 9 and 10. The pellets are sized using an industrial size distribution and the contact parameters from the previous validation work are applied. The hopper is discharged with a counter current gas flowing through the pellets and out the top of the hopper.

Figure 9. Generic axisymmetric conical hopper shape created

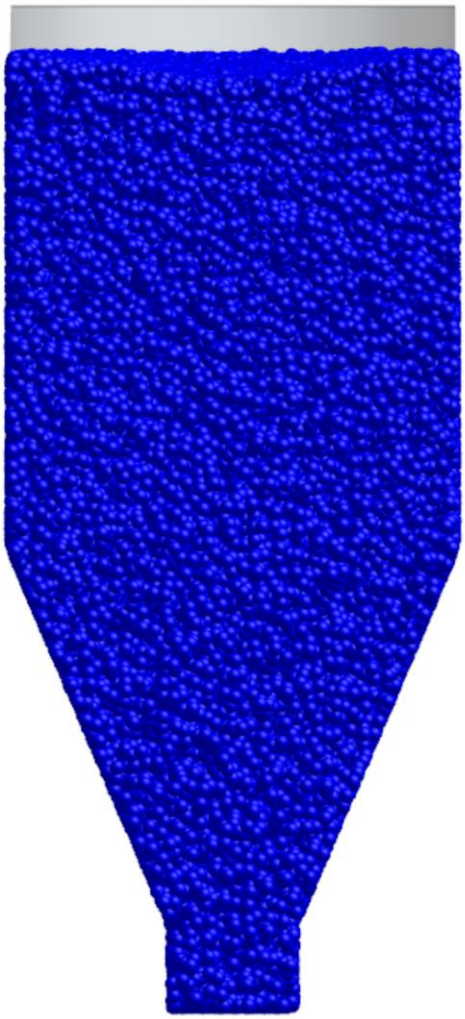

Figure 10. Generic hopper Filled with pellets

Within the narrowing portion of the hopper, shown in figure 11, the average void fraction and the average velocity of the particles are tracked, along with the volume average gas velocity and pressure. The time elapsed per iteration of the simulation is recorded using xx processors for 50 iterations. This case serves as a baseline case.

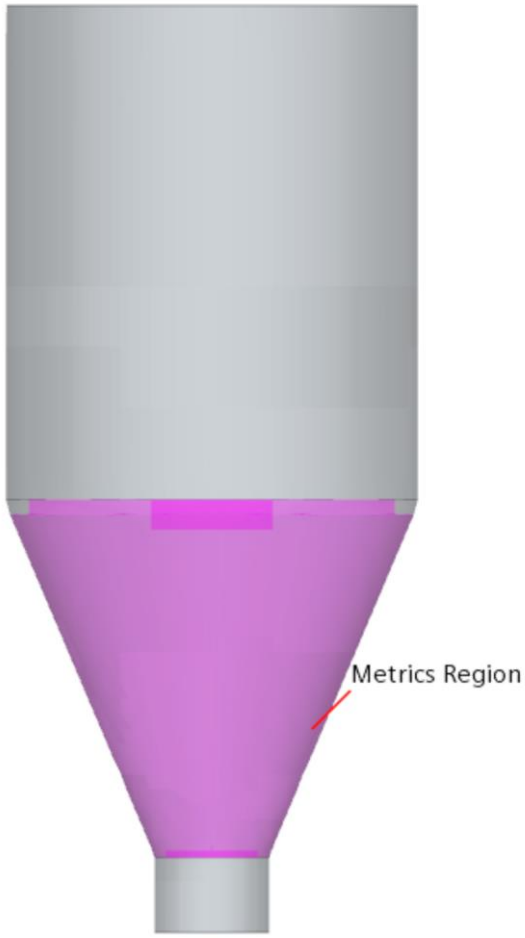

Figure 11. Hopper region where metrics are gathered highlighted

The particle size and distribution are parameterized, and the metrics are recorded again for each case. Cases are also run with the hopper domain longitudinally sliced into a symmetric third using symmetry conditions, shown in figure 12. The gas flow rate is one third the baseline case for cases using the one third hopper domain. The boundary conditions are otherwise the same across cases.

Figure 12. One third domain of conical hopper

The case with the metrics most closely replicating the baseline values, and having sufficiently reduced the computational expense of the simulation, is selected so that the conditions used in that case are used in the full DRI feed system simulation. This is to ensure that the bulk flow characteristics relevant to jamming of the flow are modeled as closely as possible while maintaining simulation run time feasibility.

5.3 Computational Domain

The hopper used is a generic axisymmetric cone shape, not based on any specific design. The dimensions of the hopper are shown in figure 13, and has a volume of 1.59m^3.

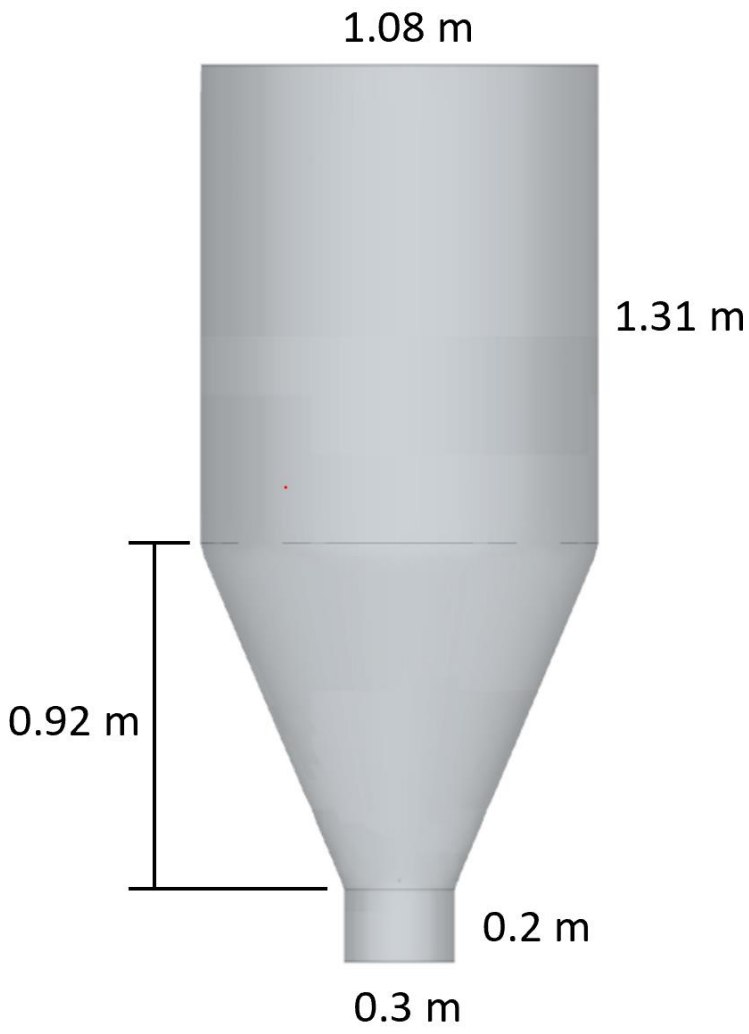

Figure 13. Small test hopper with dimensions

The hopper is sliced into a periodic symmetric third of the original domain along its longitudinal axis, shown previously in figure 12.

The mesh base cell size for each domain is the same, set at 0.08 m, shown in figure 14.

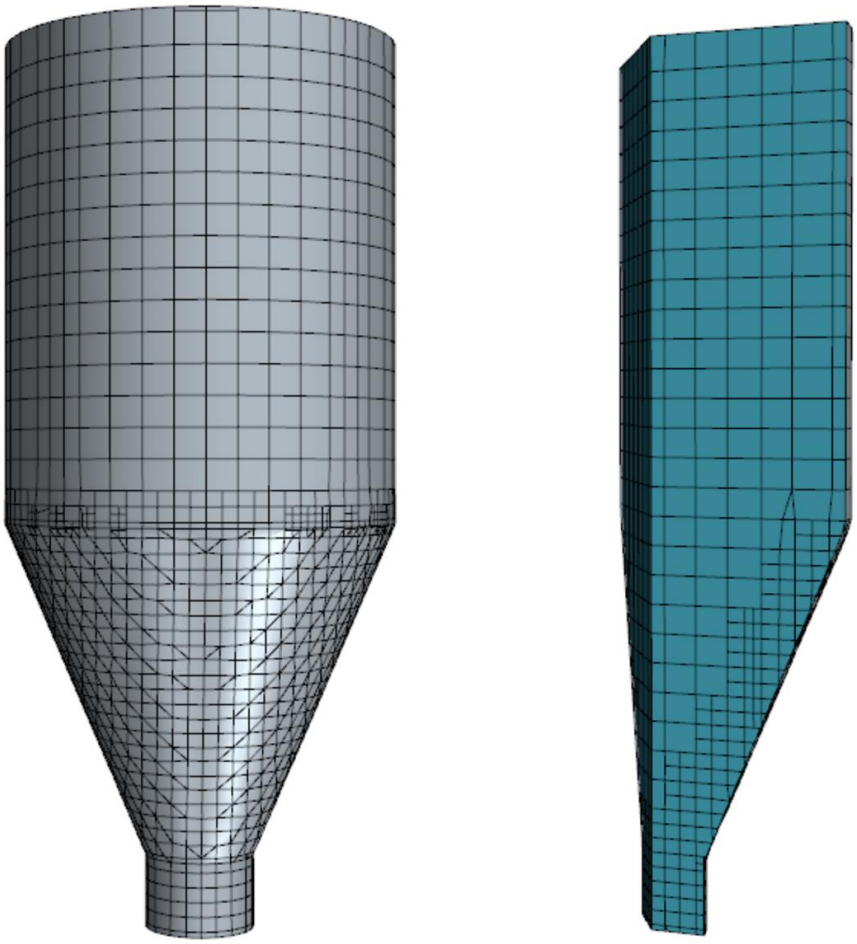

Figure 14. Mesh of full small test hopper (left) and 1/3 domain (right)

The mesh is relatively course so that no cell is fully covered by a particle, to promote simulation stability, and to limit the computational expense. The mesh contains no wall boundary inflation layers because the pellet density is high and the boundary layer created by each individual particle is not accounted for using DEM-CFD coupling. Various validated DEM-CFD results have been produced in the literature using averaged flow field values applied to the particles, and the modeling of boundary layers on walls in packed bed and fluidized bed flow has been shown to not impact results.

5.4 Physics Models

The simulation is a two-way coupled DEM-CFD simulation. Momentum is exchanged between the solid and fluid phases, but no mass exchange or energy exchange is modeled. The Hertz Mindlin force model is used to model the forces acting on the particles. The Di Felice drag force model is used to model drag exerted on the particles from the counterflow gas. The realizable k-epsilon turbulence model is used to model the turbulence of the fluid phase, and has been shown to be a suitable model for two-way DEM-CFD coupled simulations of fluidized and packed beds. The simulation is a transient simulation with a CFD timestep of 0.001s, and an internally calculated DEM timestep.

5.4.1 Pellet and Gas Properties

The pellet material properties and contact parameters are shown in tables 5 and 6, respectively.

Table 5. Pellet material properties

Iron Ore Pellet Material Properties	
Density (kg/m^3)	3948
Poison's Ratio	0.25
Young's Modulus (MPa)	40

Table 6. Pellet contact parameters

	Pellet-Pellet Contact	**Pellet-Steel Contact**
Static Friction Coefficient	0.50	0.40
Coefficient of Restitution	0.48	0.39
Coefficient of Rolling Friction	0.20	0.25

The gas properties are shown in table 7:

Table 7. Gas properties

Gas Properties	
Density (kg/m^3)	1.26
Dynamic Viscosity (Pa-s)	1.788E-5

5.5 Boundary Conditions

For all cases the bottom opening of the hopper is a wall during fill up with ore pellets, and then set as a gas inlet that allows the free fall of pellets out of the domain when discharging. The gas enters though the inlet at 1.91m/s. The walls of the hopper are set as a wall boundary condition, and in the 1/3 domain symmetry boundaries are implemented. The top opening of the hopper is a gas pressure outlet set at 1atm. The boundary conditions for both cases are shown in figure 15.

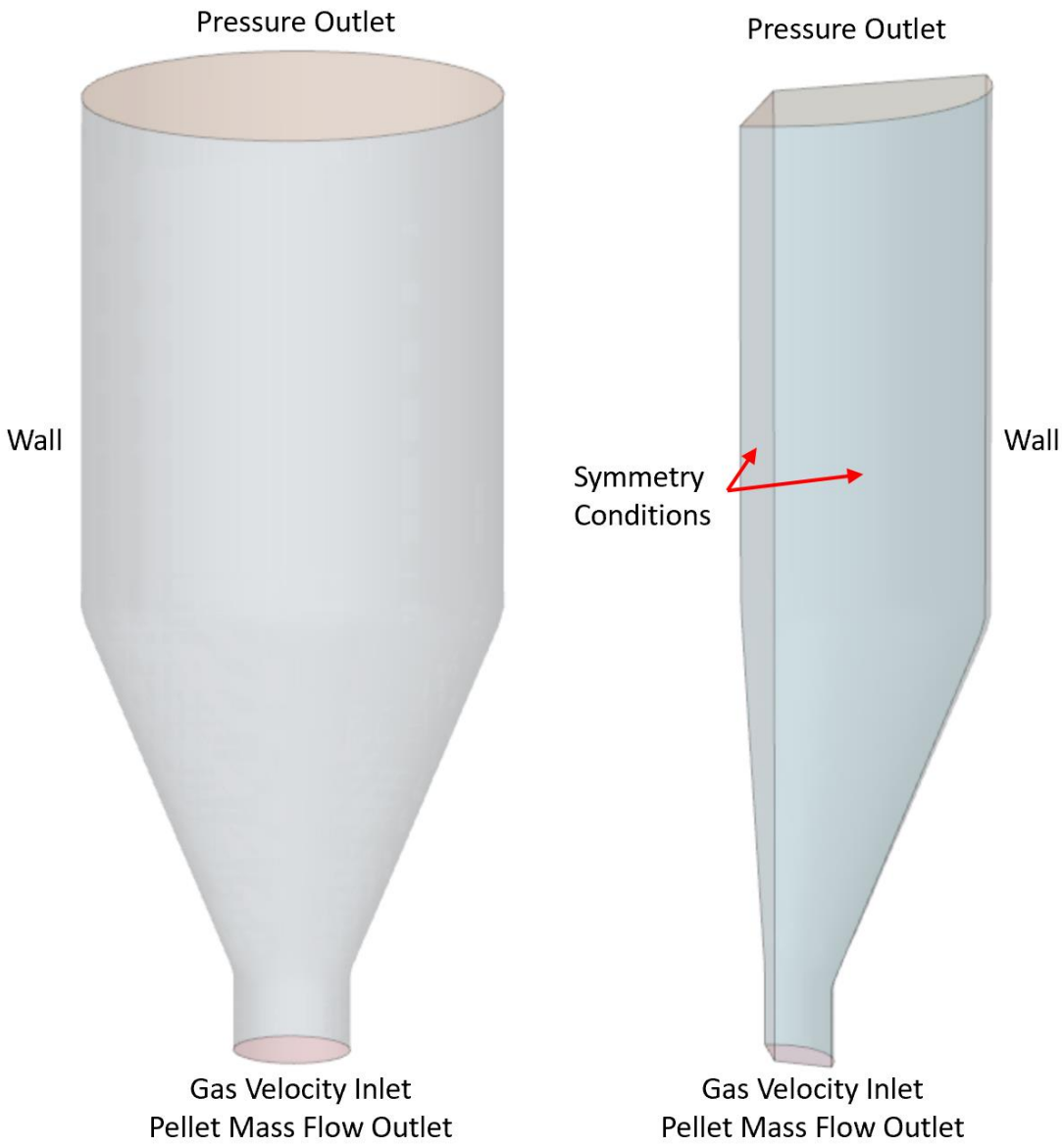

Figure 15. Boundary conditions for both domains

5.5.1 Parameterized Case Conditions

Eleven cases including the baseline are completed. The 10 cases apart from the baseline have different particle distributions and sizes, or use the one third hopper domain, or both. Six cases use a uniform particle size distribution with the particle diameter equivalent to some multiple of the base case average particle size. Nine cases use the one third hopper domain and 2 use the full hopper. The cases, which geometry they use, particle distribution, particle diameter relative to baseline, and number of particles charged are all shown in table 8.

Table 8. Case parameterizations details

	Geometry	**Particle Distribution**	**Particle Diameter Multiplier**	**Particle Number**	**Normalized Particle Number**
Baseline	Full	Distribution	1.00	1411374	1.00
Case 2	Full	Distribution	2.00	253144	0.18
Case 3	Third	Distribution	1.00	999377	0.71
Case 4	Third	Distribution	2.00	96120	0.07
Case 5	Third	Uniform	2.00 x base avg.	58137	0.04
Case 6	Third	Uniform	1.00 x base avg.	469189	0.33
Case 7	Third	Distribution	1.50	169316	0.12
Case 8	Third	Uniform	1.50 x base avg.	135755	0.10
Case 9	Third	Uniform	1.40 x base avg.	170243	0.12
Case 10	Third	Uniform	1.60 x base avg.	109647	0.08
Case 11	Third	Uniform	1.45 x base avg.	146736	0.10

5.6 Results

5.6.1 Computational Cost

The computational cost was reduced for each case when compared to the baseline case. The recorded time elapsed per iteration is presented in table 9, along with the percent change from the baseline case.

Table 9. Time elapsed per iteration and percent change from baseline for all cases

	Base	Case 2	Case 3	Case 4	Case 5	Case 6	Case 7	Case 8	Case 9	Case 10	Case 11
Time per Iteration (s)	**627.78**	48.14	336.78	13.44	2.19	38.15	35.00	7.64	9.12	5.50	8.28
Percent Change (%)	---	-92.3	-46.4	-97.9	-99.7	-93.9	-94.4	-98.8	-98.5	-99.1	-98.7

5.6.2 Void Fraction

The mean void fraction for each of the cases between 2-8 seconds of flow time is recorded. The mean void fraction for all of the cases varied from a value of 0.361 to 0.394. The void fraction for each case is plotted in figure 16 and the mean values are in table 10.

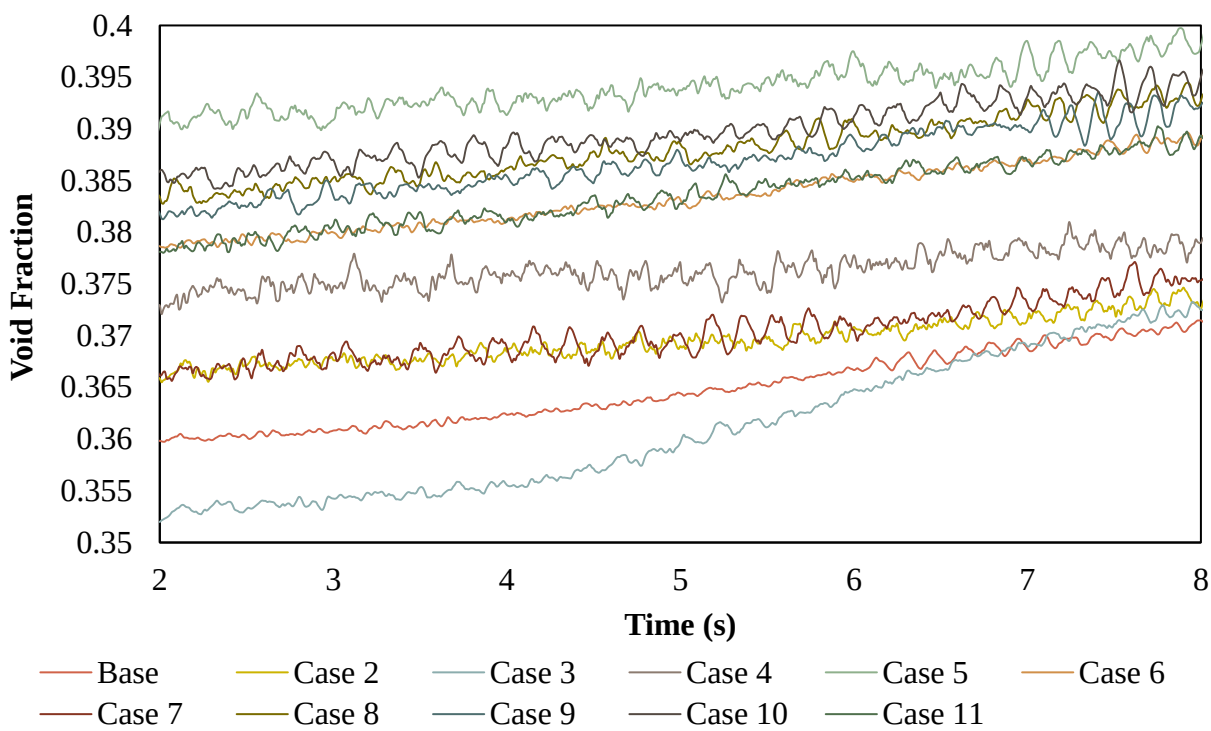

Figure 16. Void fraction vs time for all cases between 2-8s of flow

Table 10. Mean void fractions and percent change for all cases between 2-8s of flow time

	Base	Case 2	Case 3	Case 4	Case 5	Case 6	Case 7	Case 8	Case 9	Case 10	Case 11
Mean Void Fraction	0.365	0.370	0.361	0.376	0.394	0.383	0.370	0.388	0.387	0.390	0.384
Percent Change (%)	---	1.31	-1.05	3.17	8.04	5.11	1.50	6.38	6.04	6.83	5.15

5.6.3 Mean Pellet Velocity

The mean velocity of the pellets is also recorded between 2-8s of flow time. The mean velocity verses time is plotted in figures 17-21 and the mean value across time is shown in table 11. The mean velocity percent change from the baseline ranges from -12.85 to 5.35%.

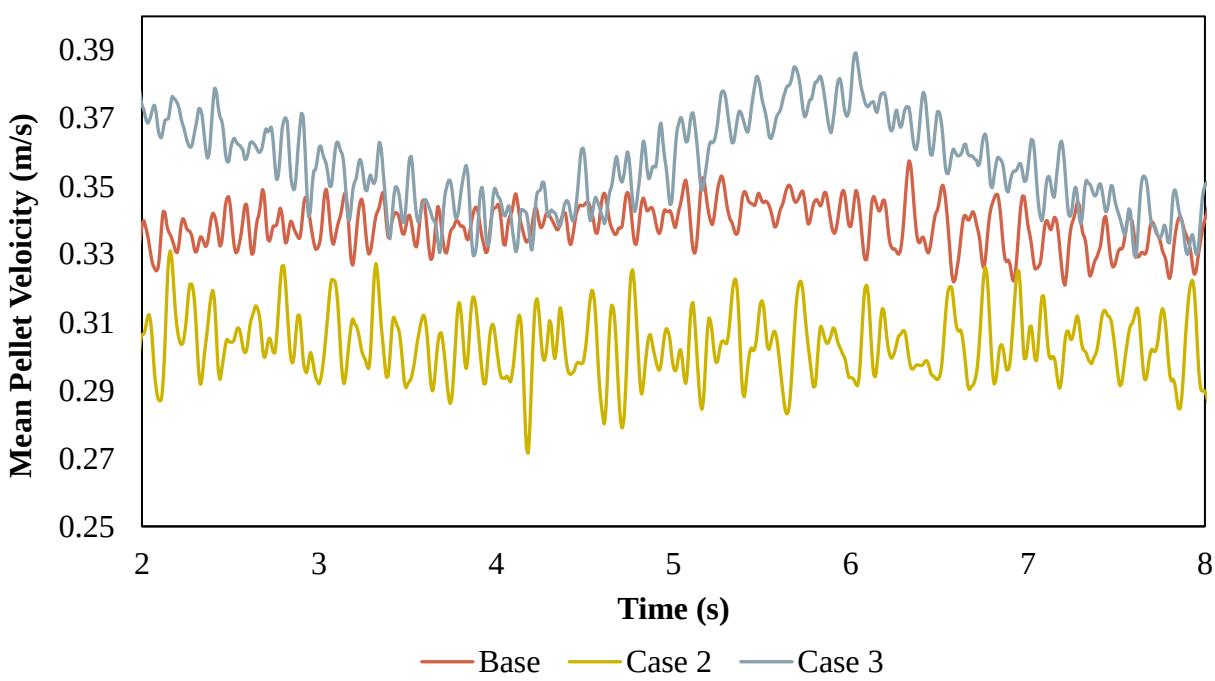

Figure 17. Mean pellet velocity vs time for cases 2 and 3 between 2-8s flow time

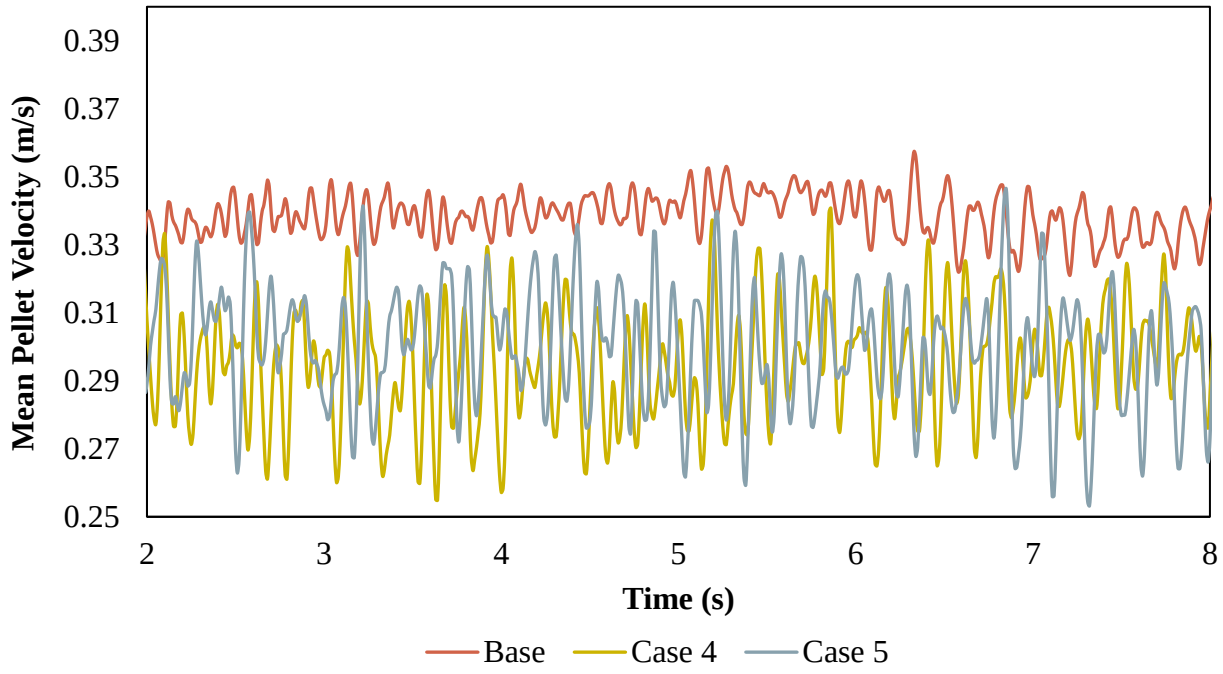

Figure 18. Mean pellet velocity vs time for cases 4 and 5 between 2-8s flow time

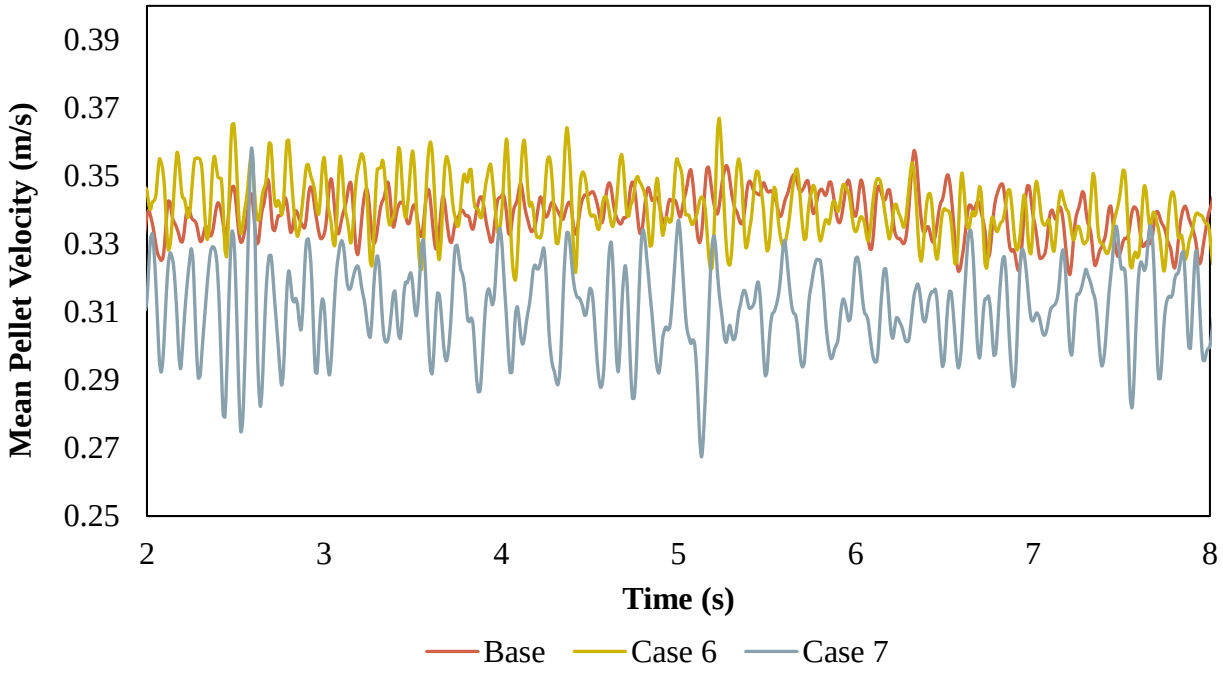

Figure 19. Mean pellet velocity vs time for cases 6 and 7 between 2-8s flow time

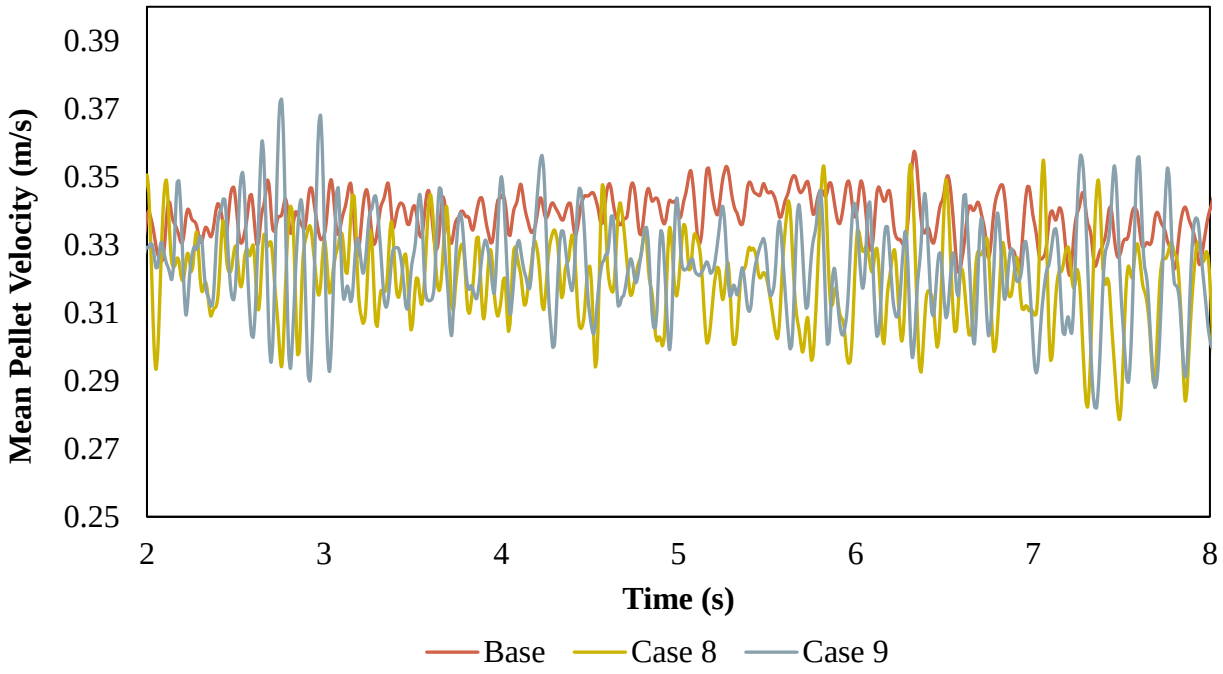

Figure 20. Mean pellet velocity vs time for cases 8 and 9 between 2-8s flow time

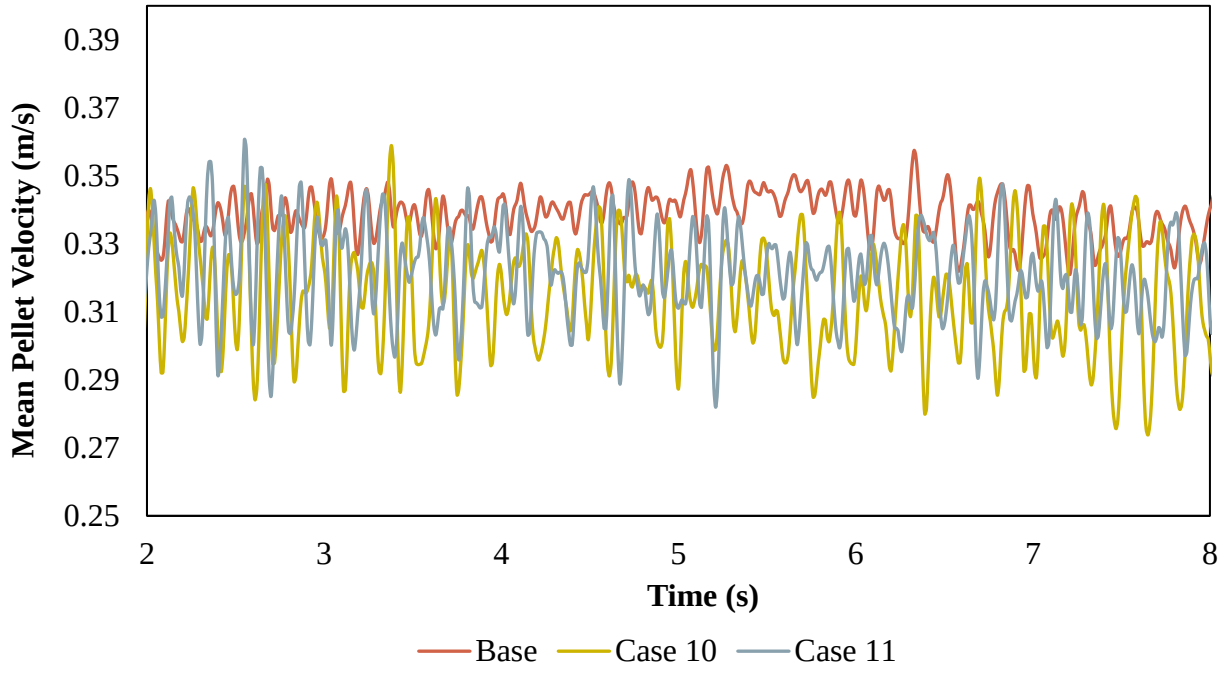

Figure 21. Mean pellet velocity vs time for cases 10 and 11 between 2-8s flow time

Table 11. Average of mean pellet velocity across 2-8s flow time window

	Base	Case 2	Case 3	Case 4	Case 5	Case 6	Case 7	Case 8	Case 9	Case 10	Case 11
Mean Velocity (m/s)	0.339	0.303	0.357	0.295	0.300	0.341	0.311	0.320	0.323	0.315	0.321
Percent Change (%)	---	-10.37	5.35	-12.85	-11.30	0.67	-8.12	-5.52	-4.48	-6.99	-5.07

5.6.4 Gas Velocity

The volume average gas velocity is also recorded in the 2-8s flow time window and the values are plotted in figures 22-26. The volume average gas velocity percent change from baseline ranges in value from -5.9 to 1.9%, shown in table 12 along with mean values for each case.

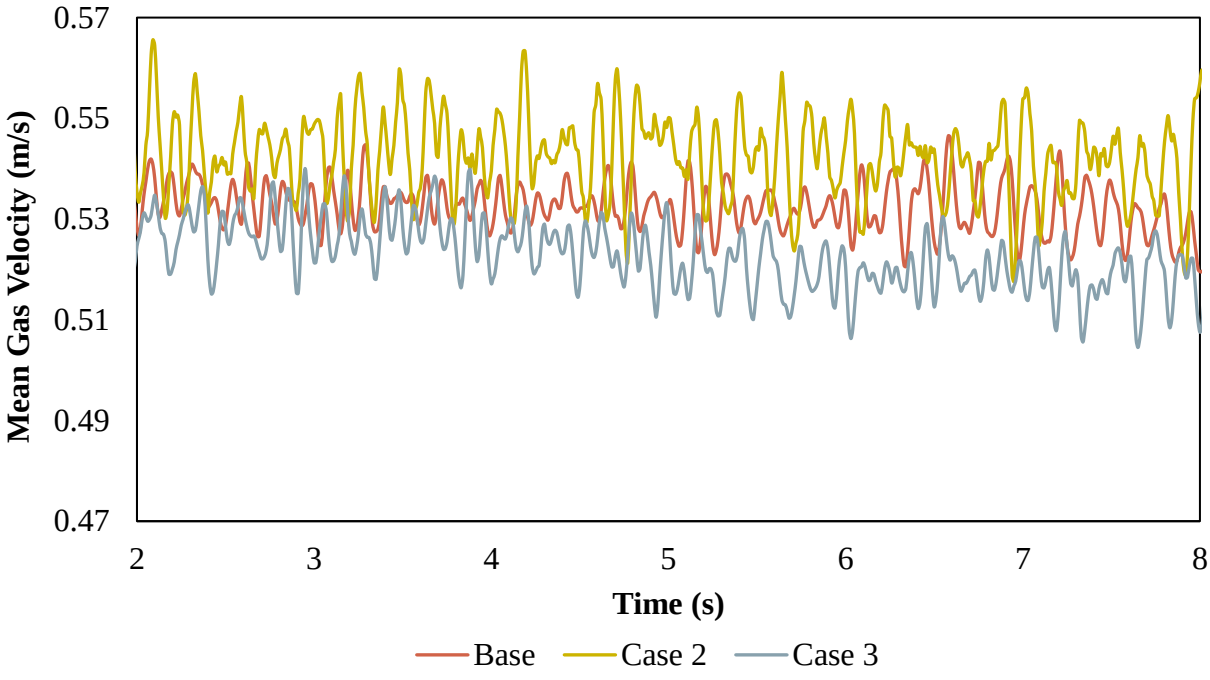

Figure 22. Average gas velocity for cases 2 and 3 between 2-8s flow time

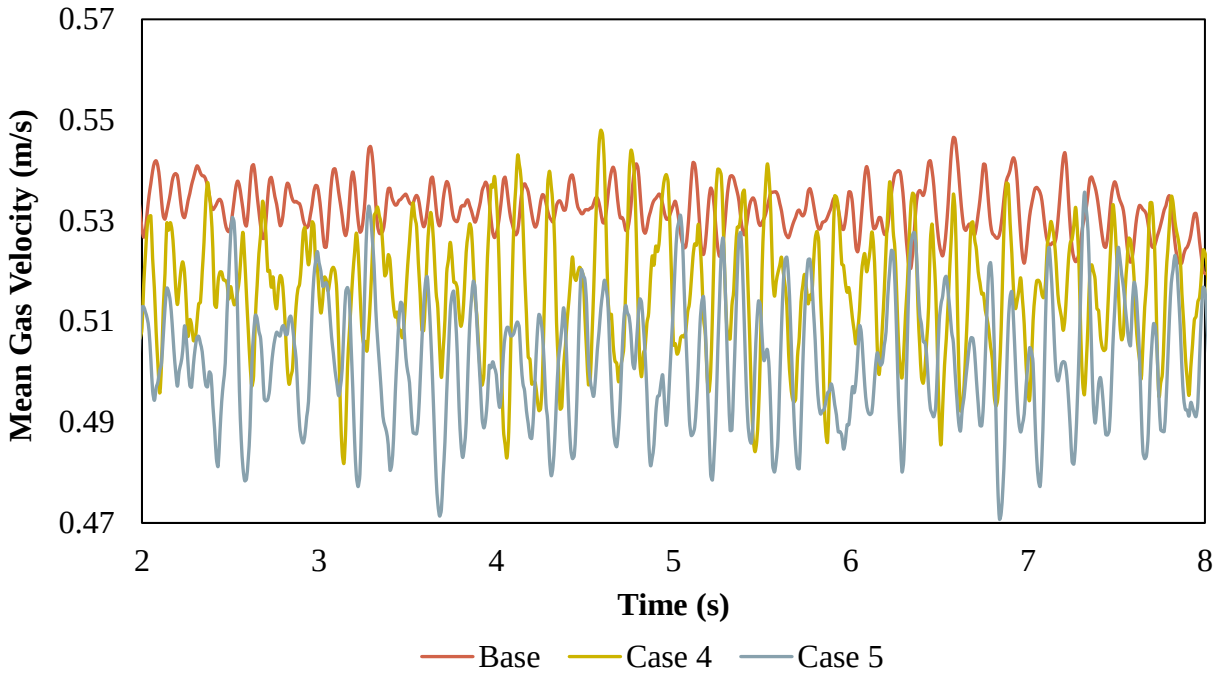

Figure 23. Average gas velocity for cases 4 and 5 between 2-8s flow time

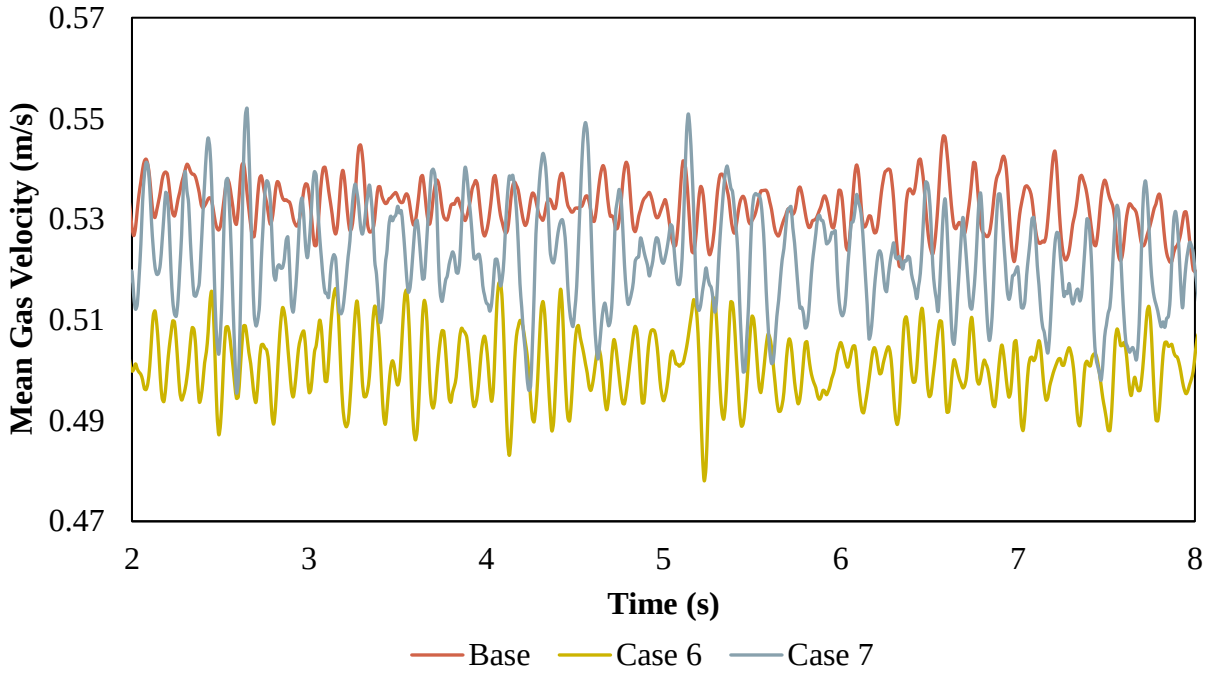

Figure 24. Average gas velocity for cases 6 and 7 between 2-8s flow time

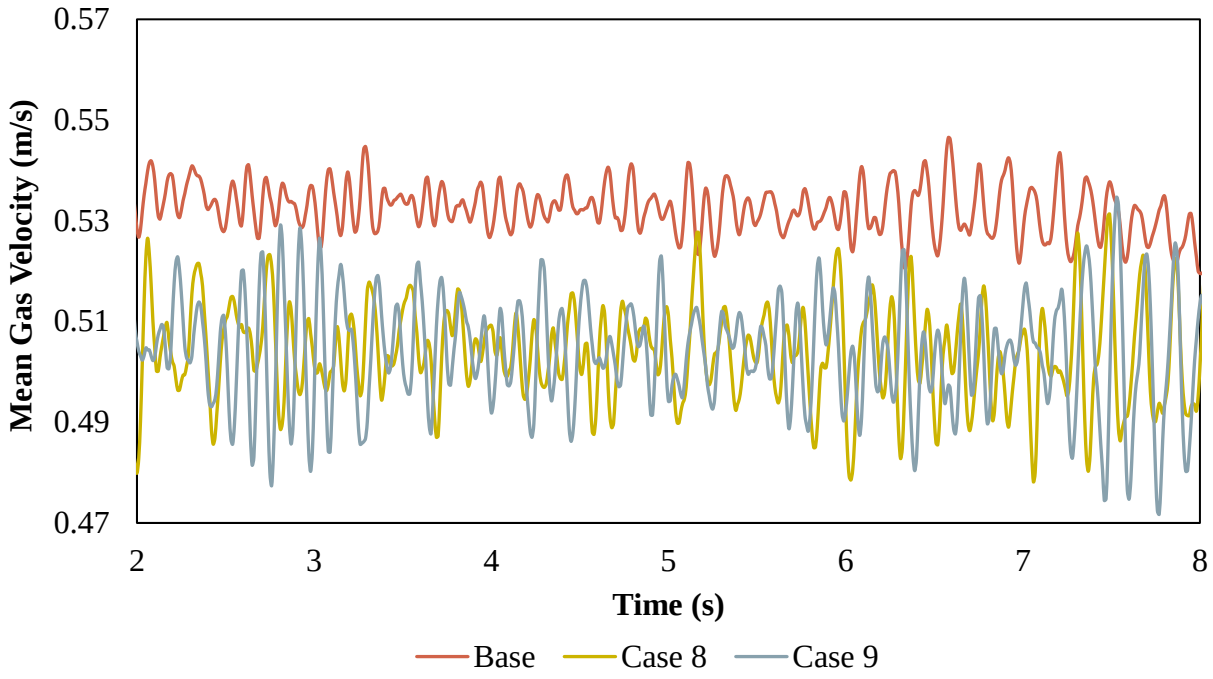

Figure 25. Average gas velocity for cases 8 and 9 between 2-8s flow time

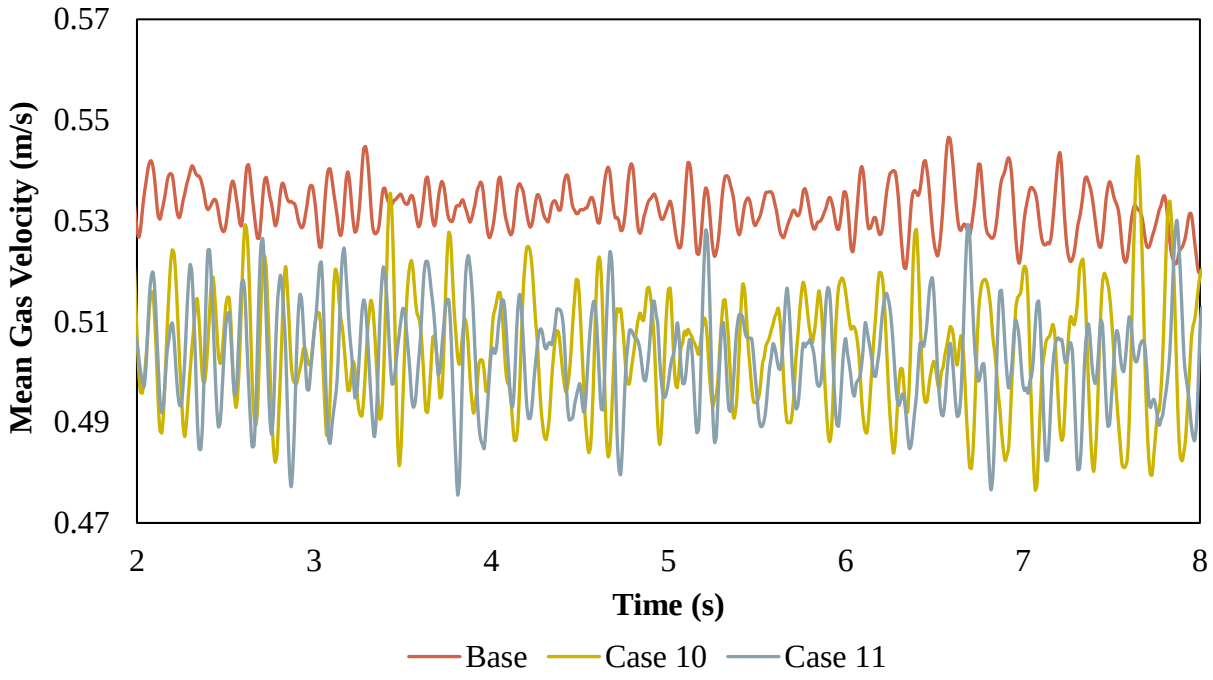

Figure 26. Average gas velocity for cases 10 and 11 between 2-8s flow time

Table 12. Mean gas velocity for all cases and percent change from baseline

	Base	Case 2	Case 3	Case 4	Case 5	Case 6	Case 7	Case 8	Case 9	Case 10	Case 11
Mean Gas Velocity (m/s)	0.532	0.542	0.523	0.516	0.502	0.501	0.522	0.504	0.504	0.504	0.503
Percent Change (%)	---	1.9	-1.8	-3.1	-5.7	-5.9	-2.0	-5.4	-5.4	-5.3	-5.6

5.6.5 Gas Pressure

The gas pressure as the pellets discharged the hopper varied significantly across time peaking in the first 2 seconds of the flow and then decreasing, shown in figures 27 and 28. The percent change in peak pressured ranged from -53.4 to 40.9% and the values of the pressure and the percent change from baseline are presented in table 13.

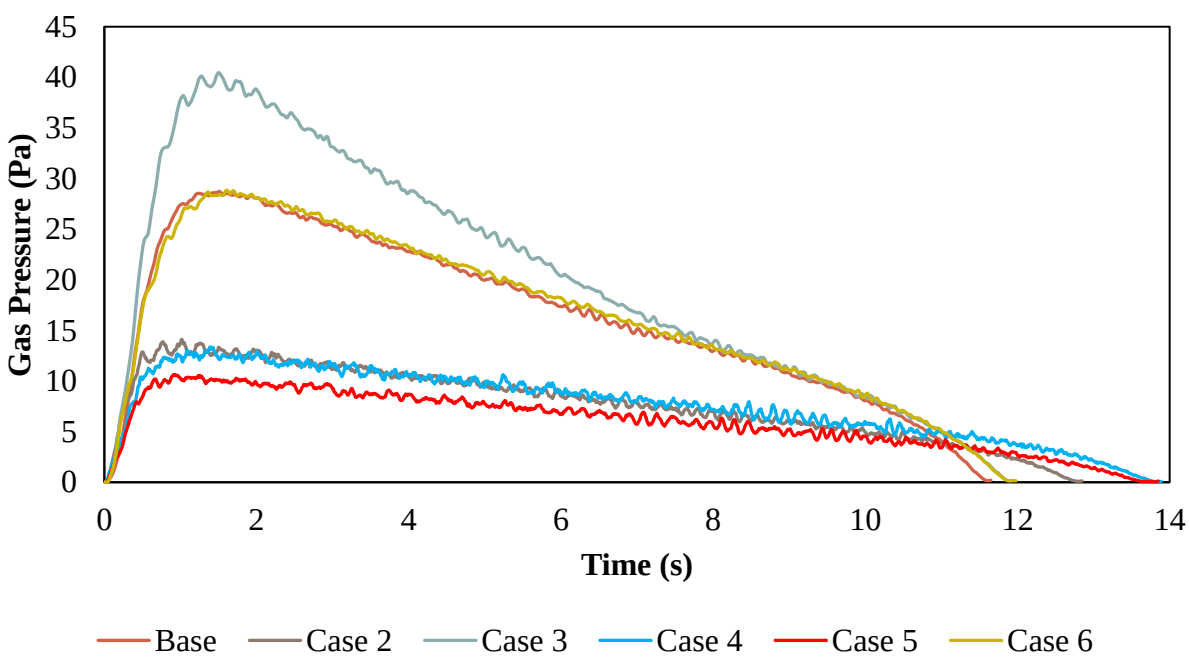

Figure 27. Gas pressure for cases 2-6 vs time

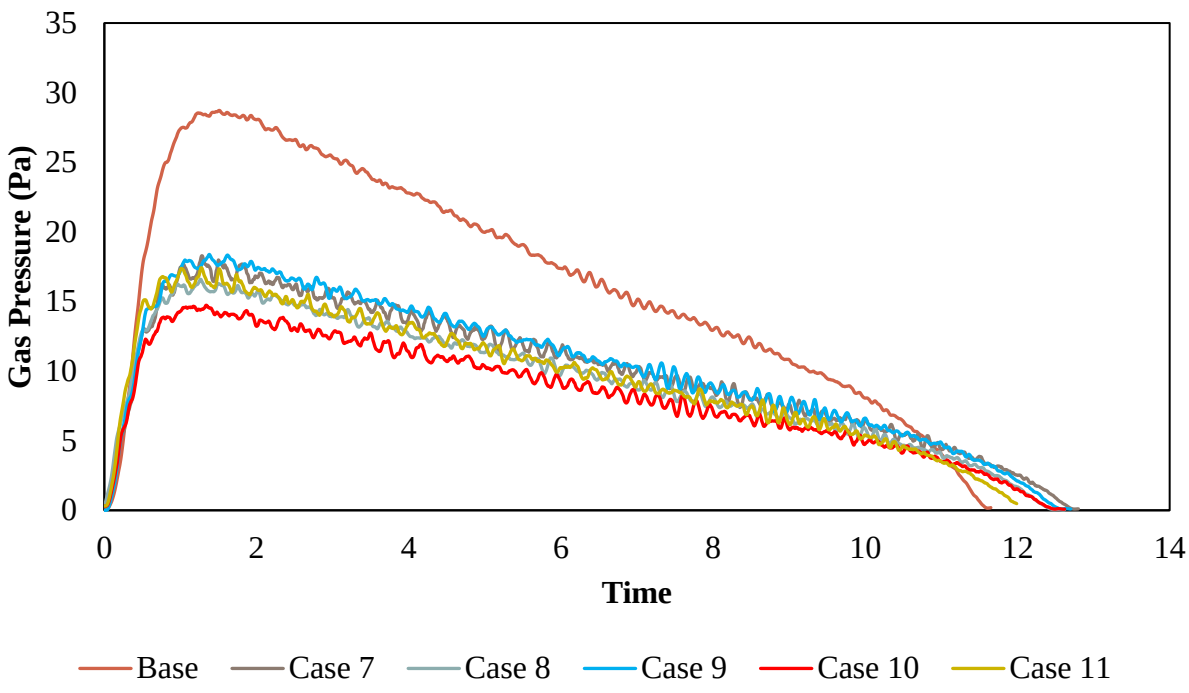

Figure 28. Gas pressure for cases 7-11 vs time

Table 13. Peak pressure values and percent change

	Base	Case 2	Case 3	Case 4	Case 5	Case 6	Case 7	Case 8	Case 9	Case 10	Case 11
Peak Pressure (Pa)	28.7	14.1	40.5	13.4	13.4	28.8	18.3	16.6	18.4	14.7	17.4
Percent Change (%)	---	-50.9	40.9	-53.4	-53.4	0.4	-36.3	-42.3	-36.0	-48.7	-39.4

5.6.6 Discussion

The computational cost of simulating potentially hundreds of millions of particles within the DRI feed system is a limiting factor when trying to model the system using DEM. However, because DEM is the best suited model to model jamming of the feed system, the parameters that

lower the computational expense are parameterized to reduce the cost, and so that the bulk flow parameters relevant to jamming are conserved.

Cases 5, and 8-11 sufficiently lowered the computational expense of the simulation, each lowering the time elapsed per iteration by approximately 99%.

The void fraction and particle velocity are the two primary bulk flow characteristics monitored so that the jamming behavior of the bulk flow is maintained. Of the cases that reduced the computational expense sufficiently, the case with the closest average void fraction is case 11 with a 5.15% increase from the baseline then case 9 with a 6.04% increase. The case with the least change in average particle velocity is case 9 with a -4.48% change from baseline, then case 11 with a -5.07% change from baseline.

The case with the closest gas velocity to the baseline case is case 10 with a -5.3% change. Cases 8 and 9 are second at -5.4%. The percent change of the gas velocity for all of the cases that lowered the expense sufficiently were all similar, with the difference between the highest and lowest percent change being 0.4%.

The peak gas pressure that was closest to baseline was case 9 with a -36.0% change from baseline. Case 11 was second with a -39.4% change from baseline.

The case that is selected as best matching the baseline case is case 11. Cases 9 and 11 were similar in how close the void and particle velocities were to the baseline case, and deviated the least out of the viable cases. However, case 11 has a lower computational expense than case 9. The average gas velocity was very close for all the cases and case 9 and 11. The conditions for the baseline and case 11 are presented in table 14.

Table 14. Baseline vs case 11 conditions

	Geometry	**Particle Distribution**	**Particle Diameter Multiplier**	**Normalized Particle Number**
Baseline	Full	Distribution	1.00	1.00
Case 11	Third	Uniform	1.45 x base avg.	0.10

The conditions implemented in case 11 are implemented into the baseline case and all subsequent cases modeling the feed system.

6. BASELINE OPERATION

6.1 Background

Pellets are charged into a material feed system above the DRI shaft furnace. The area they are charged into is a large hopper containing a flow aid insert. The pellets descend at a controlled rate into a seal leg to be fed into the shaft furnace. A gas is supplied through the seal leg below the hopper to prevent gas from the shaft from entering the hopper.

6.2 Methodology

The feed system is reportedly jamming in the hopper near the flow aid insert. DEM is used to model the pellet flow, because clogging is a bulk flow phenomenon that is dependent on forces acting on and the positions of individual particles. The model is coupled with CFD to capture the effects of the seal leg gas flow.

The hopper is modeled using a 1/3 slice of the domain with the upper portion of the hopper removed and without the seal leg, shown in figure 29. The domain is charged with pellets in the cone portion of the hopper. To replicate the weight of the charge above this point larger and denser particles are charged on top of the pellets, shown in figure 30.

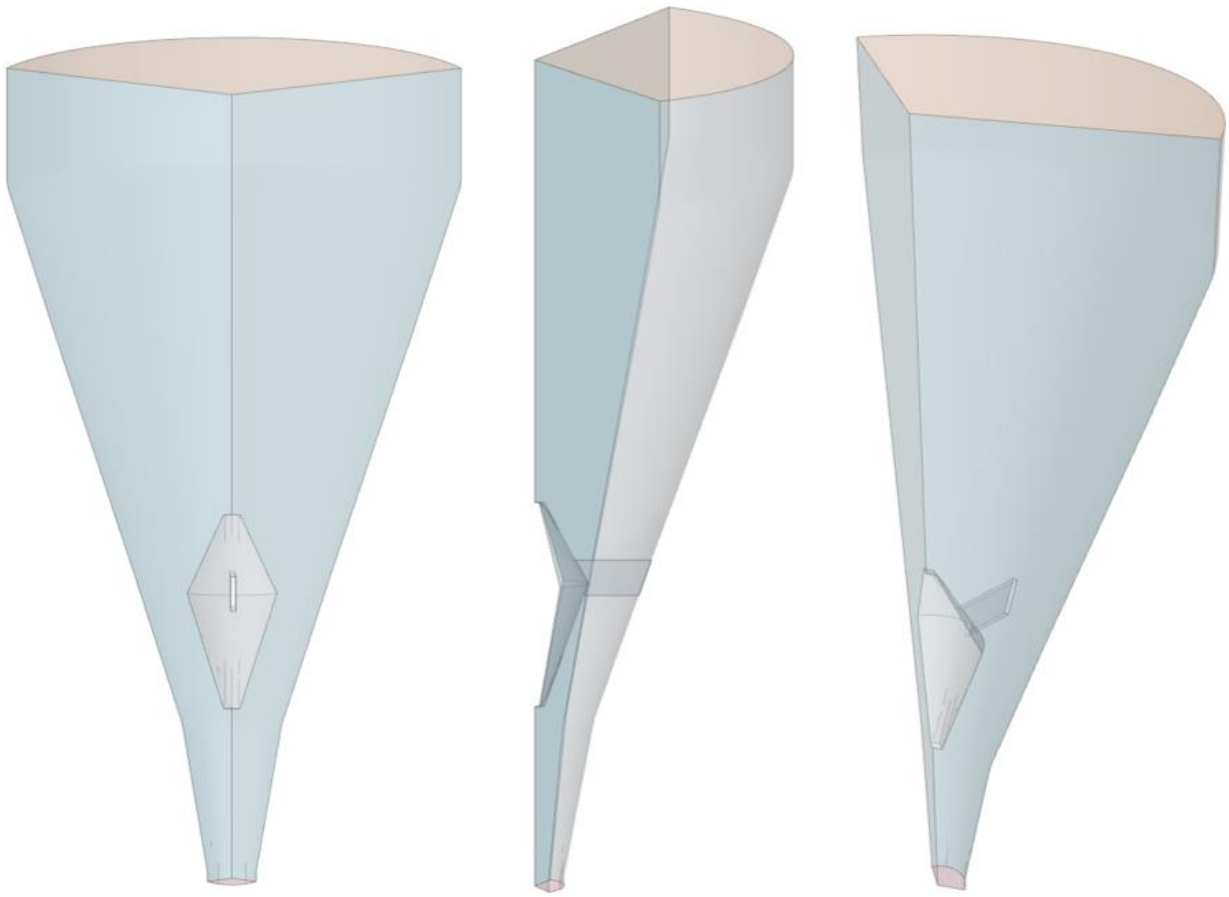

Figure 29. One third hopper geometry with upper portion shortened and no seal leg

Figure 30. Domain filled pellets in grey and large heavy pellets in red

The flow of pellets out of the domain is controlled, and gas is injected into the domain counter to the flow of pellets. The forces on the flow aid insert and the outer walls of the hopper are tracked to determine when the bulk flow reaches a quasi-steady state. The average void fraction and velocity of the particles are tracked near the upper portion and near the lower portion of the flow aid insert, shown in figure 31.

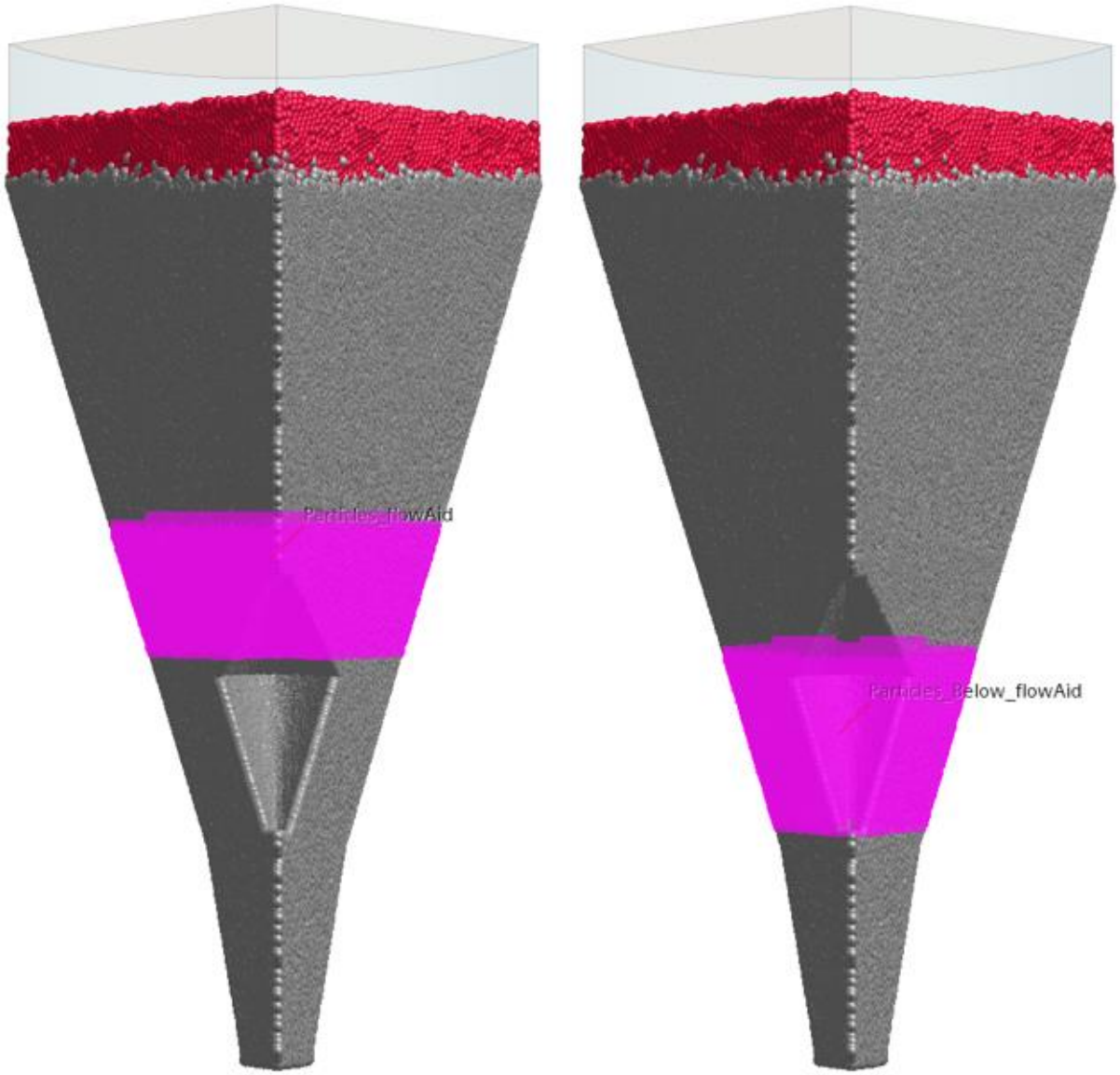

Figure 31. Region where metrics are tracked near the upper (left) and lower (right) portion of the flow aid highlighted in purple

6.3 Computational Domain

The hopper is meshed using a cell size of 0.07 m, shown in figure 32. The cell size is larger than the pellet size so that the cells are not fully covered by the pellets, promoting simulation stability, and to lower the computational expense of the simulation. Because of this the flow field between the pellets is not resolved, meaning that the boundary effects between particles are not captured, rather, average cell properties are applied to the pellets, and the void fraction applied to the cell.

There are no inflation layers near the wall surface because of the disruption of wall boundary layers in dense granular flow, where boundary layers are created on every particle.

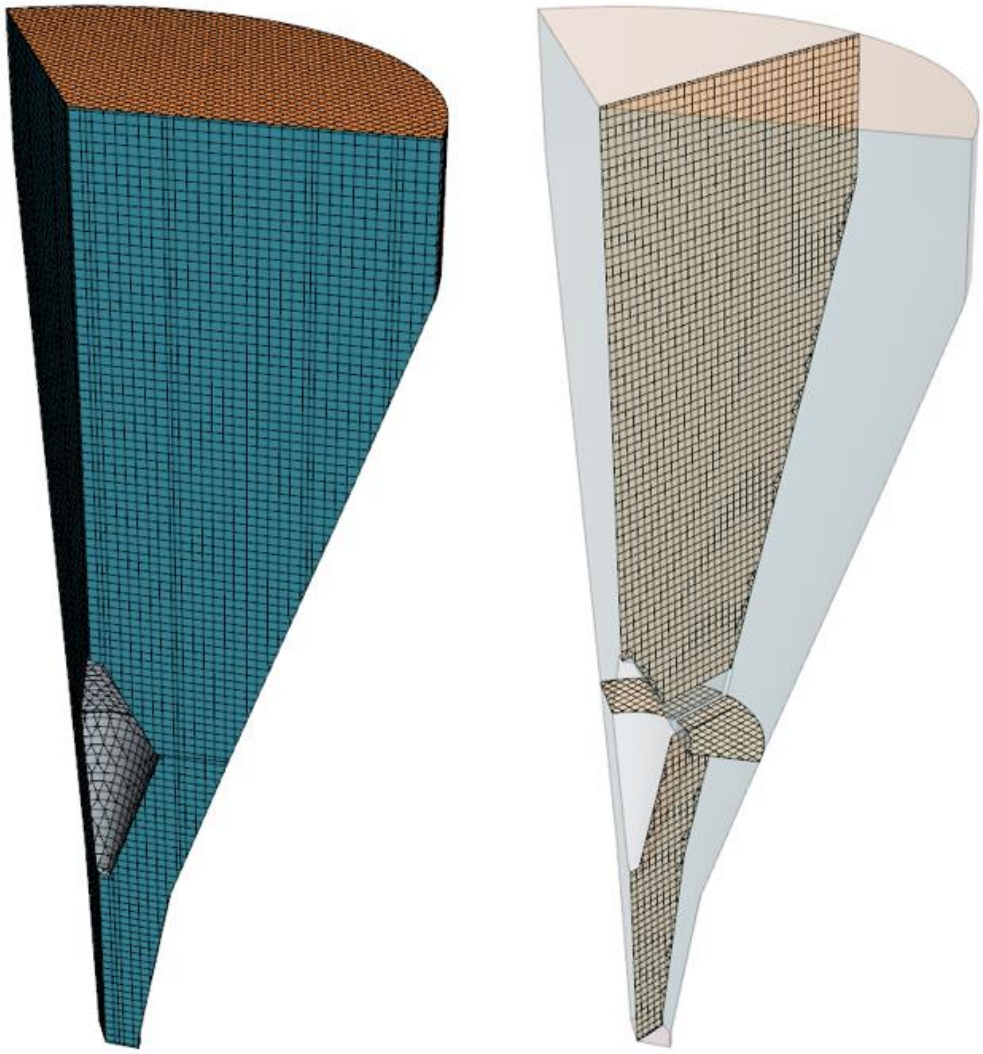

Figure 32. Mesh of domain with cross with section plane views

6.4 Physics Models

The Hertz-Mindlin model is used to model the forces acting on the pellets. The Di Felice drag force model is used to account for the drag force on the particles. The fluid and solid phases are coupled using CFD-DEM two-way coupling so that the phases exchange momentum. Mass and energy are not exchanged between the phases. The fluid phase is modeled using the coupled flow solving technique and the turbulence model used is the realizable k-epsilon turbulence model. The fluid and solid phase are modeled as a transiently.

6.4.1 Pellet and Gas Properties

The pellet material properties and contact parameters are shown in tables 15 and 16, respectively:

Table 15. Pellet material properties

Iron Ore Pellet Material Properties	
Density (kg/m^3)	3948
Poison's Ratio	0.25
Young's Modulus (MPa)	40

Table 16. Pellet contact parameters

	Pellet-Pellet Contact	**Pellet-Steel Contact**
Static Friction Coefficient	0.50	0.40
Coefficient of Restitution	0.48	0.39
Coefficient of Rolling Friction	0.20	0.25

The large pellets material properties and contact parameters are shown in tables 17 and 18:

Table 17. Large pellet properties

Large Pellet Material Properties	
Density (kg/m^3)	39480
Poison's Ratio	0.25
Young's Modulus (MPa)	40

Table 18. Large pellet contact parameters

	Large Pellet-Pellet Contact	**Large Pellet-Large Pellet Contact**	**Large Pellet-Steel Contact**
Static Friction Coefficient	0.50	0.50	0.40
Coefficient of Restitution	0.48	0.48	0.39
Coefficient of Rolling Friction	0.20	0.20	0.25

The gas properties are shown in table 19:

Table 19. Gas density and dynamic viscosity

Gas Properties	
Density (kg/m^3)	1.26
Dynamic Viscosity (Pa-s)	1.788E-5

6.5 Boundary Conditions

The hopper is divided into thirds with symmetry boundaries applied. The top opening of the hopper is a pressure outlet at 1atm, and the bottom opening is a gas velocity inlet that allows pellet to flow through at a controlled rate equivalent to that of in operation. The exact flow rate values are not disclosed, although the gas to pellet mass flow rate ratio is approximately 0.007. Pellets are continuously charged on top of the heavy particles at the same rate they leave the domain. The boundaries are labeled in figure 33, and the values listed in table 20.

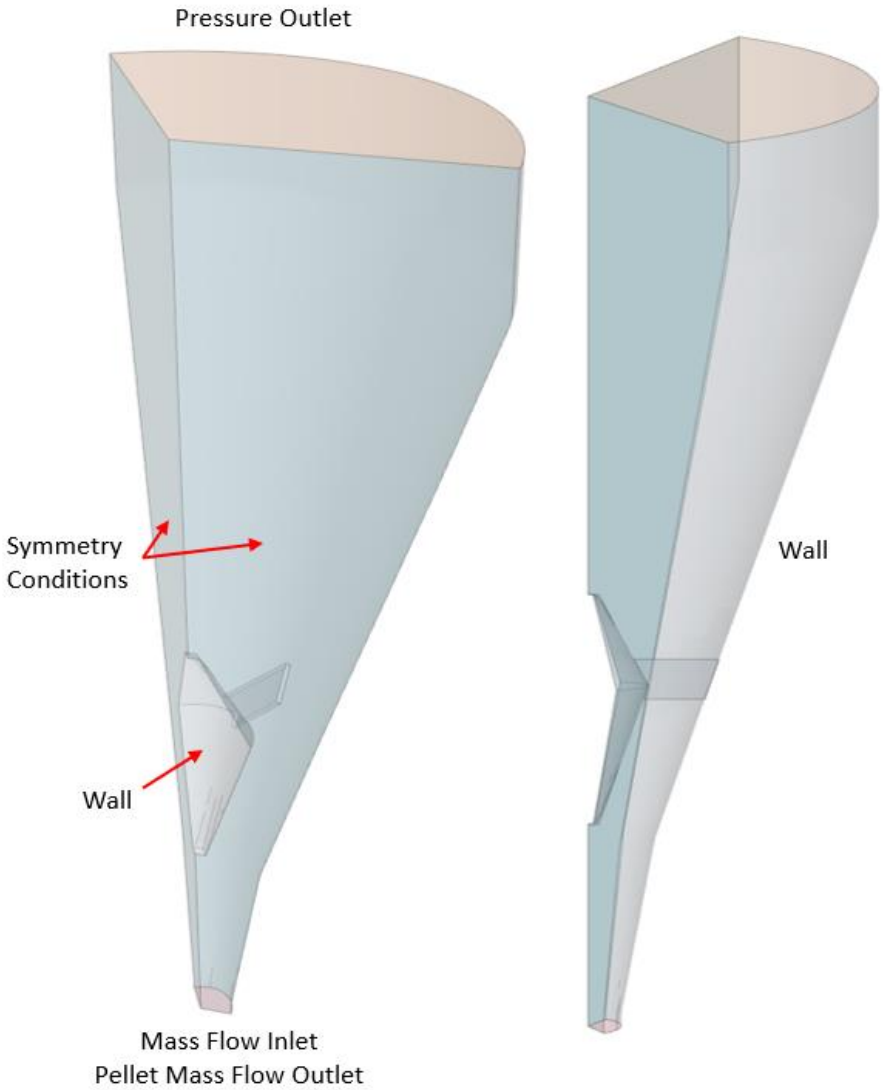

Figure 33. Hopper boundaries

Table 20. boundary condition values

Boundary Condition Values	
Gas/Ore Mass Flow Ratio	**Pressure Outlet (atm)**
0.007	1.0

6.6 Results

The average force on the flow aid and walls of the hopper become steady after approximately 3 seconds, and seem to stay steady for approximately 20 seconds, shown in figures 34 and 35, and a slight change in the forces on the walls and flow aid can be seen to occur near the 10-11 second mark on the plots. At around 10 seconds of flow time the void fraction and velocity of the pellets change dramatically, shown in figures 38, 39, 42, 43. The change in bulk flow behavior at this time point suggests that the flow is no longer steady beyond 10 seconds. The reason for the change in flow behavior of the pellets is because the large heavy pellets do not descend uniformly, and as they descend the force distribution throughout the descending bed of pellets changes.

Therefore, for analysis all average values presented for the baseline case are for values between 3-10 seconds, when the weight exerted on the pellet bed by the heavy layer is most uniform. All the plots for the baseline case contain values for the full simulation run time of 20 seconds.

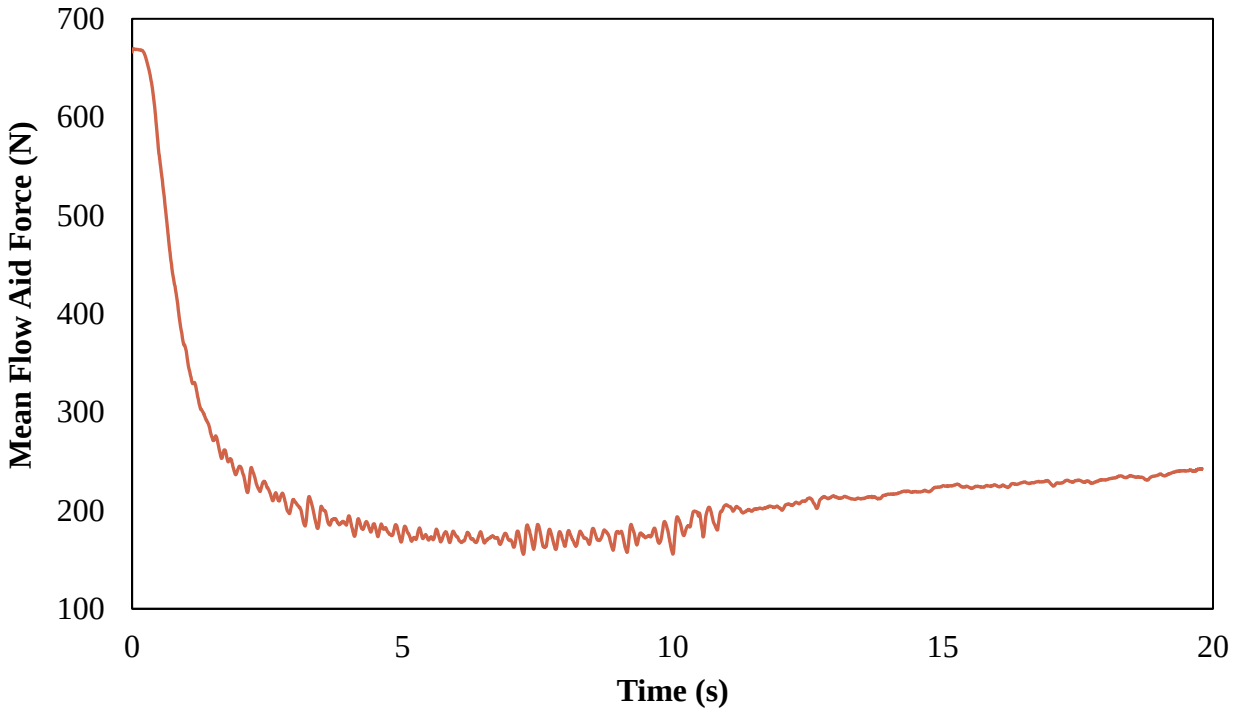

Figure 34. Plot of mean force exerted on flow aid vs time

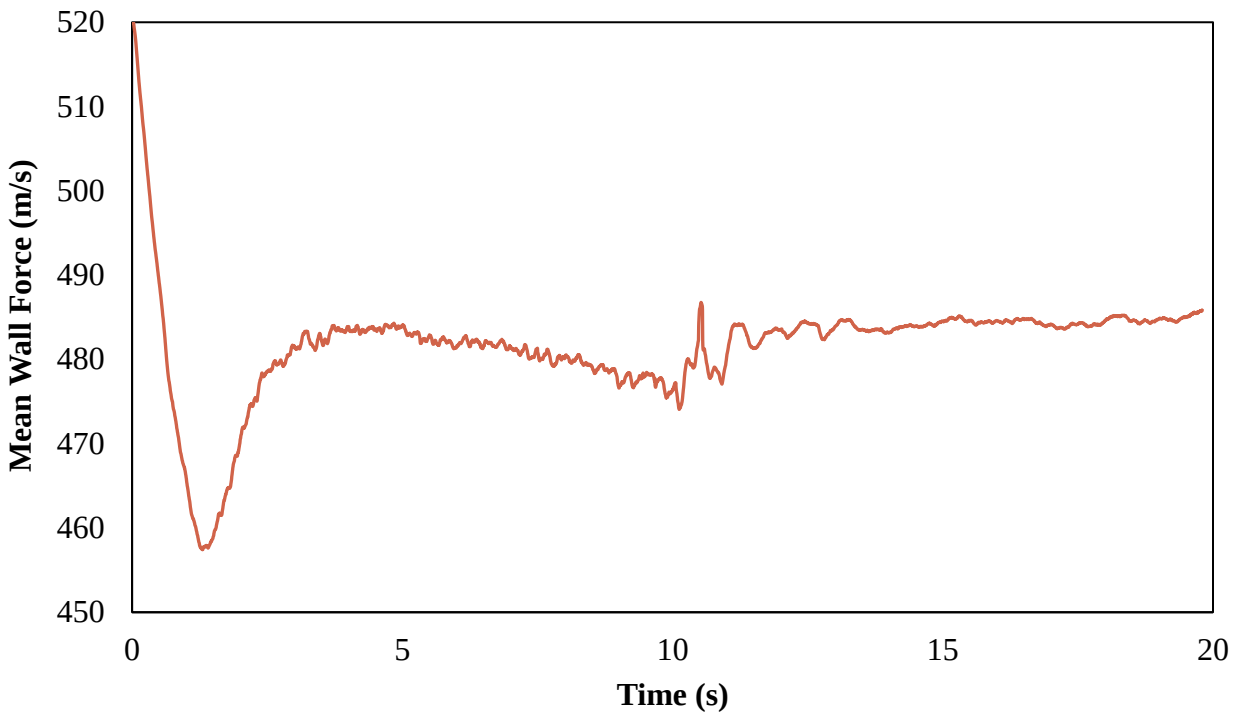

Figure 35. Plot of average wall forces

The forces on the flow aid are highest on top of the aid and very low on the bottom half shown in figure 36. The forces on the walls of the hopper are higher above the level of flow aid than below. The forces on the wall become much lower at the same level as the bottom half of the flow aid shown in figure 37.

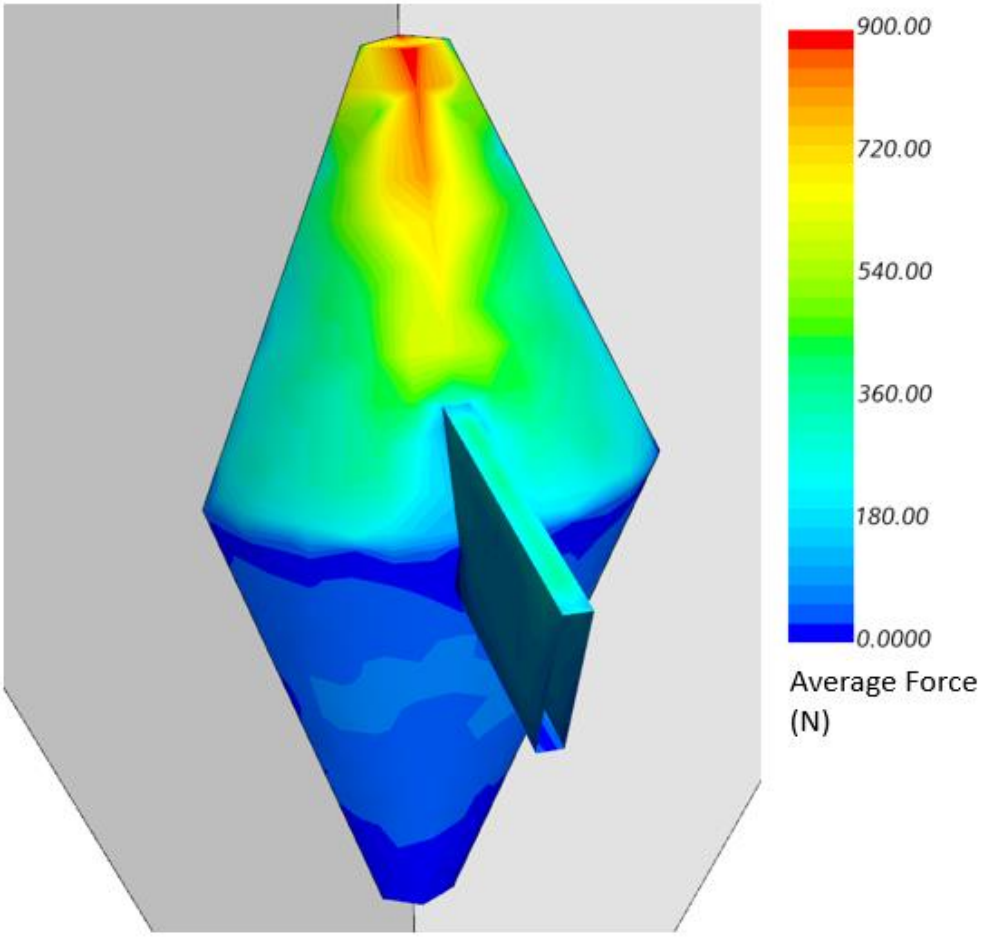

Figure 36. Forces on flow aid

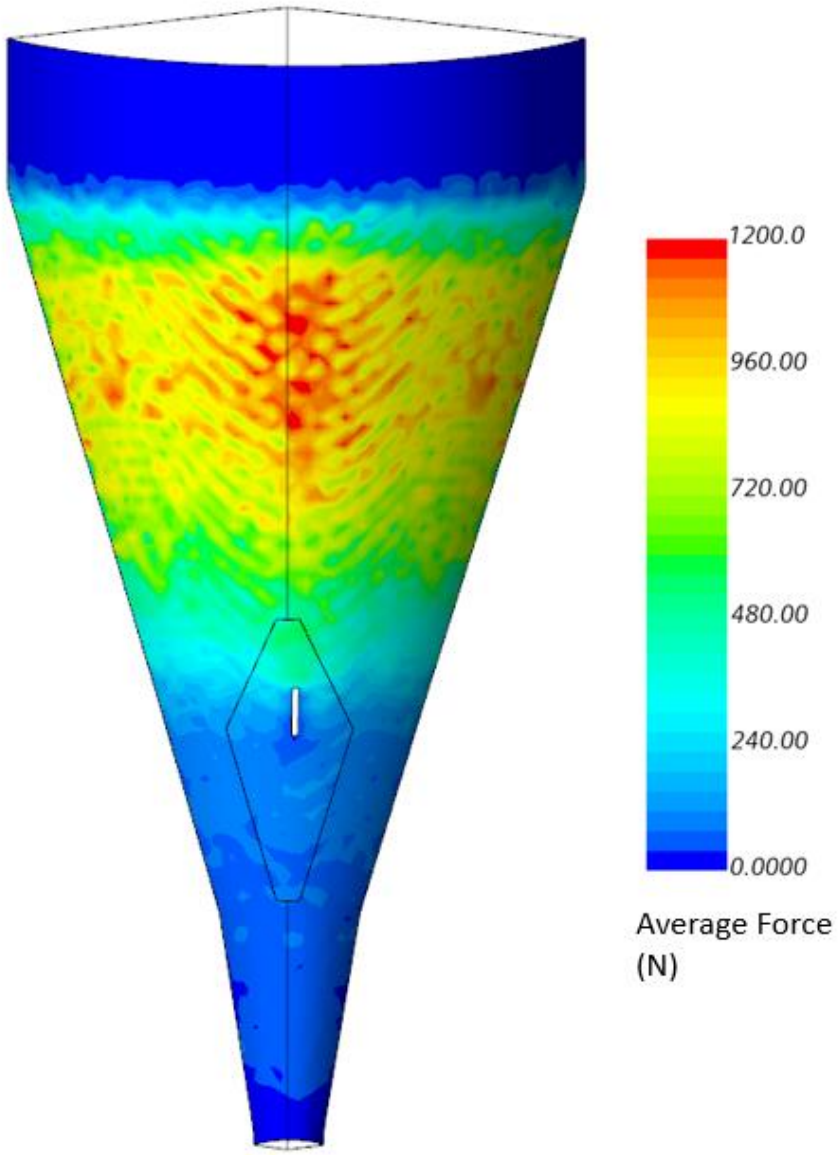

Figure 37. Forces on the walls of the hopper

The velocity of the pellets near the upper portion of the flow aid during the steady flow window have an average velocity of 0.13 m/s and with an average void fraction of 0.33 in the same area. The velocity and void fraction are plotted in figures 38 and 39, respectively. The void seems to vary dramatically at first glance of figure 39, but the variation is small within the steady window, varying between approximately 0.315 and 0.335.

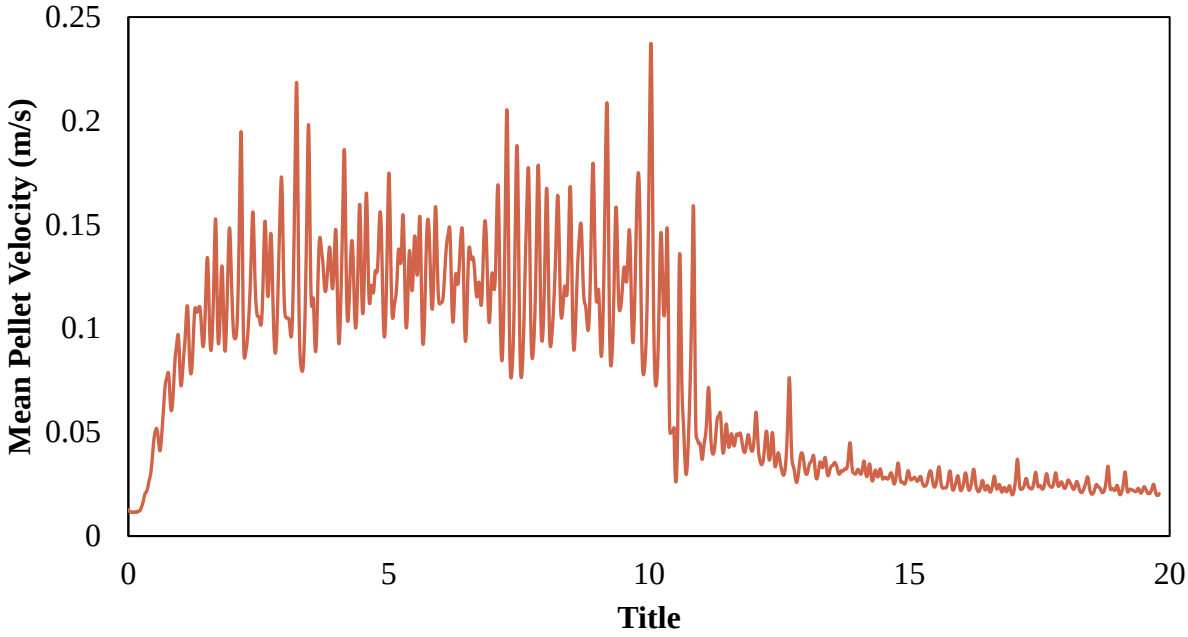

Figure 38. Pellet velocity above flow aid vs time

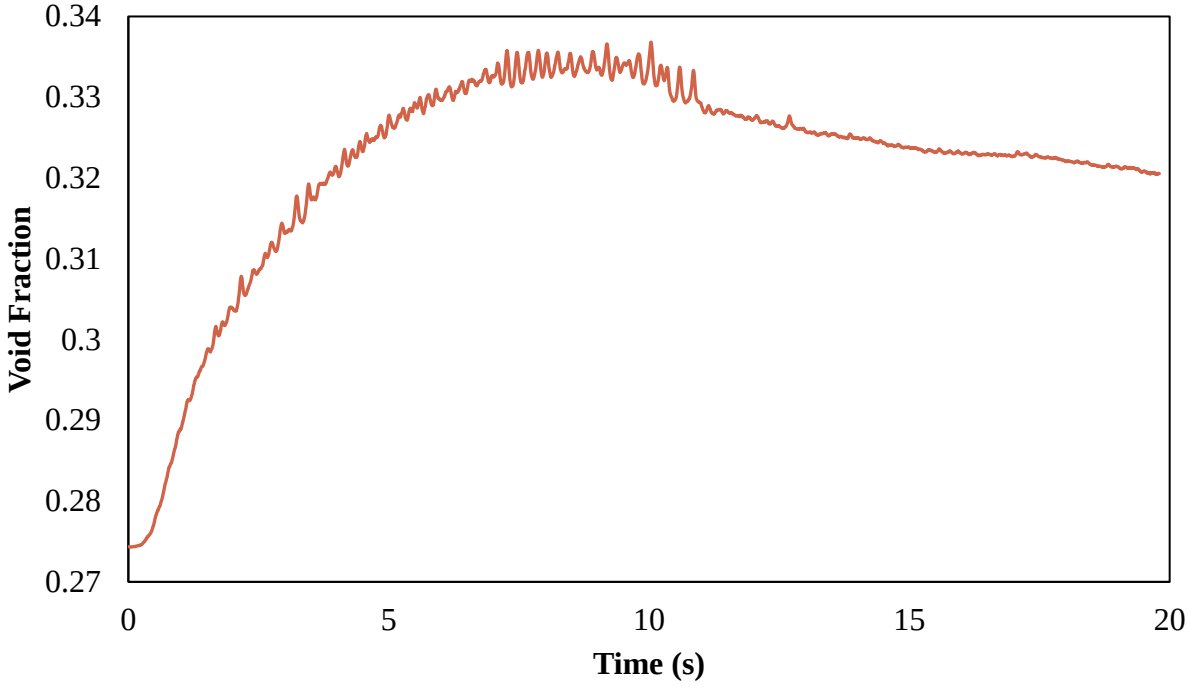

Figure 39. Void above flow aid vs time

The void fraction varies through the hopper and is higher above the flow aid and becomes lower below the flow aid shown in figure 40. The velocity of the pellets increases as they descend through the narrowing hopper, shown in figure 41.

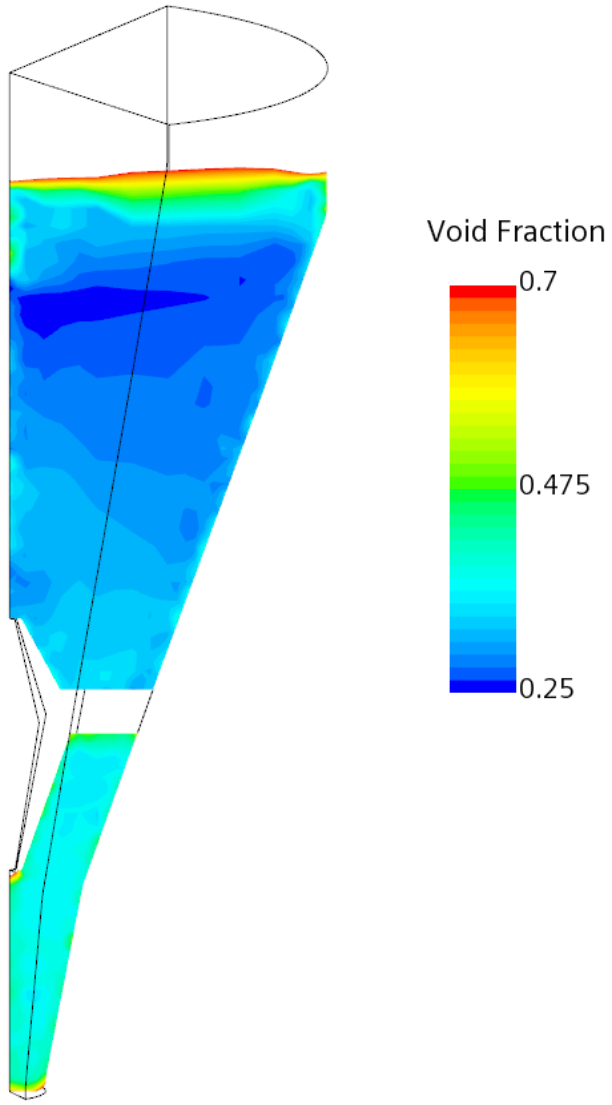

Figure 40. Void in flow aid cross section plane (clipped values)

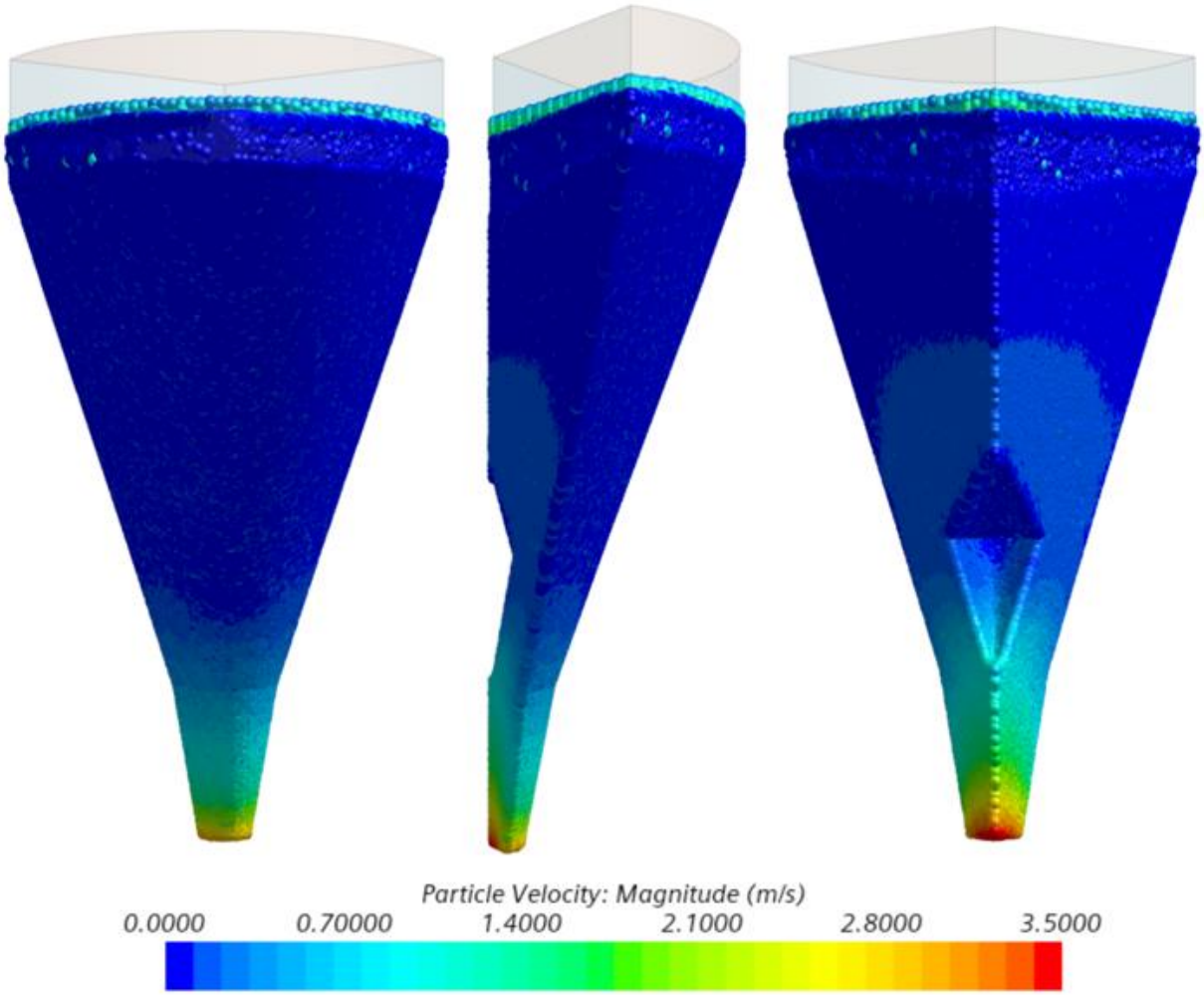

Figure 41. Velocity of the pellets increasing as the pellets descend with a noticeable pattern change around the flow aid

The void is higher near the lower portion of the flow aid with an average value of 0.37, and the velocity of the pellets is higher with an average value of 0.36 m/s. The average void and velocity bellow the flow aid are plotted in figures 42 and 43, respectively. The average values of the void and pellet velocity above and below the flow aid are shown in table 21.

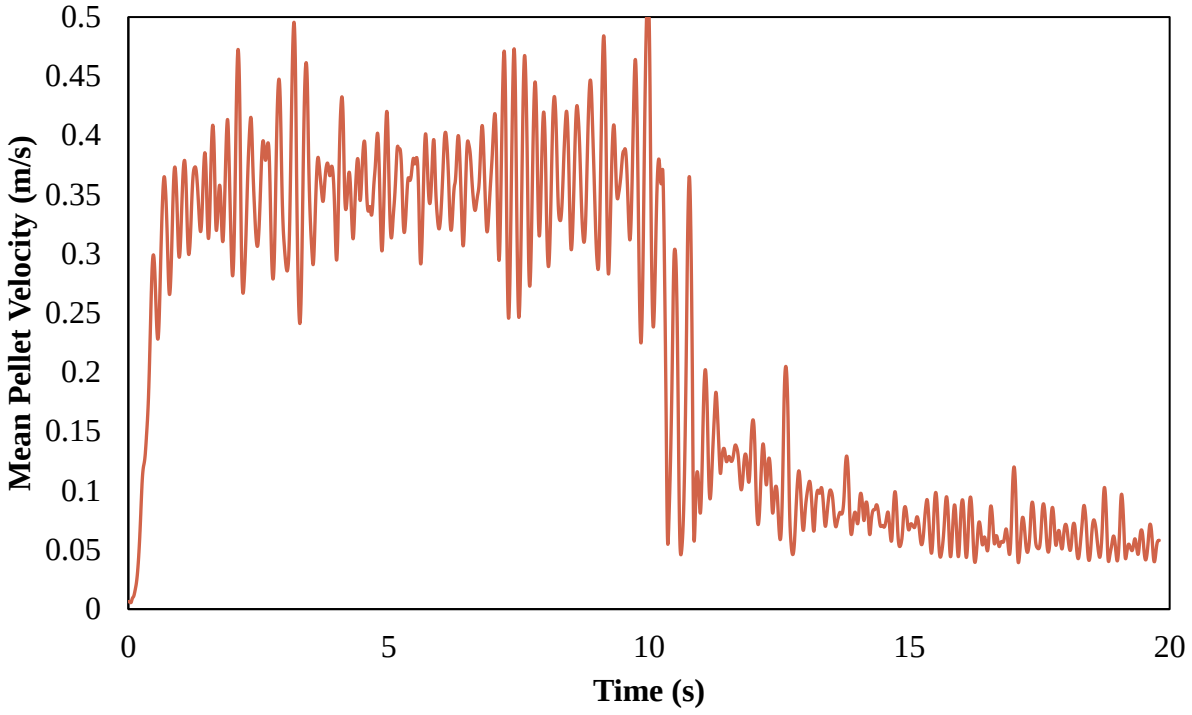

Figure 42. Pellet velocity below flow aid vs time

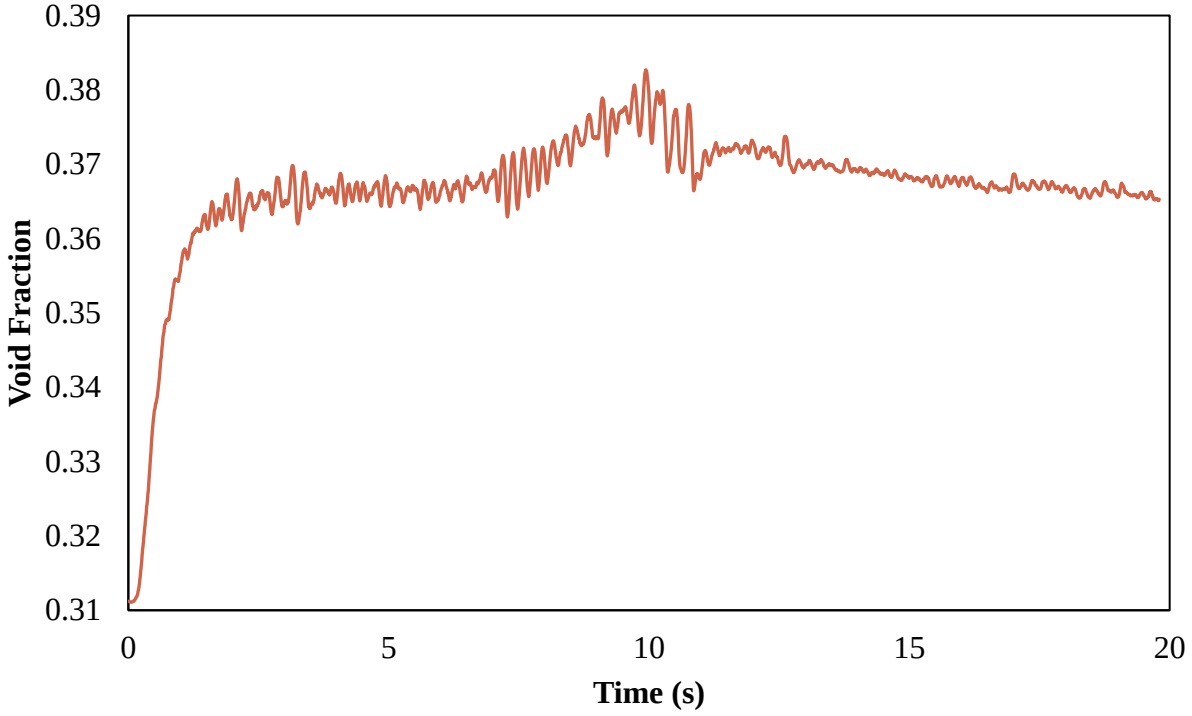

Figure 43. Void below flow aid vs time

The average gas velocity and pressure for the region near the upper aid are 0.23 m/s and 10.98 Pa respectively, and are plotted in figures 44 and 45.

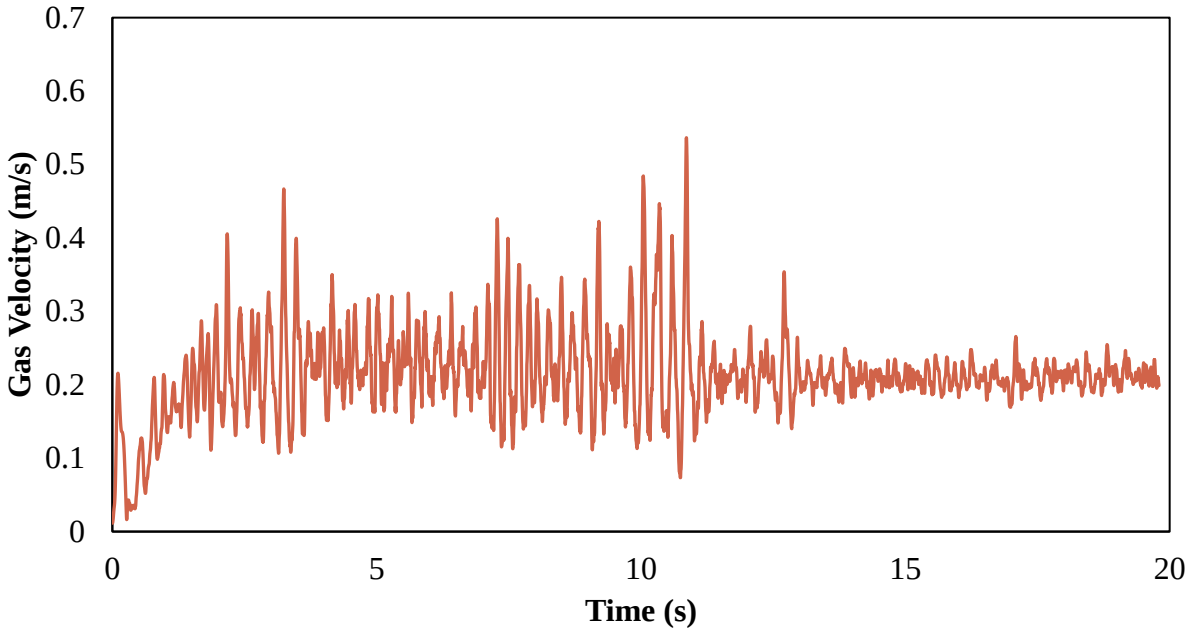

Figure 44. Gas velocity near upper portion of flow aid insert vs time

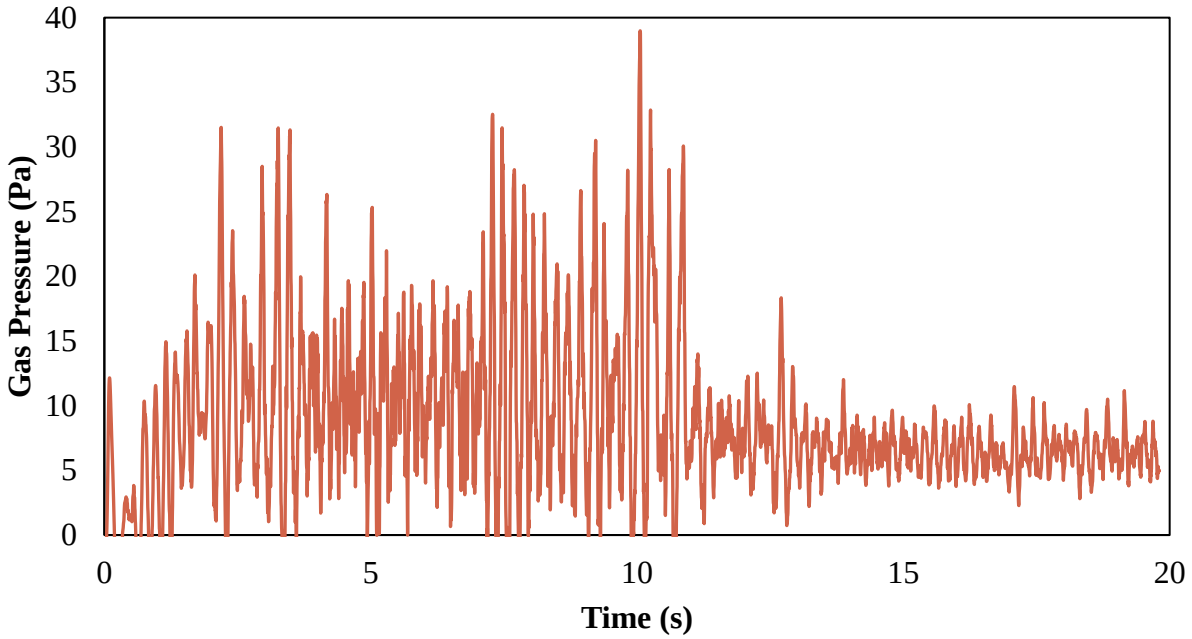

Figure 45. Gas pressure near upper portion of flow aid insert vs time

The average drag force to weight force ratio throughout the bed of pellets is sampled at the end of the simulation and found to be approximately 9.55E-5. The average values for the pellet velocity, and void fraction near the top and bottom of the flow aid insert, along with the average gas velocity and pressure are shown in table 21.

Table 21. Pellet velocity and void fraction for in upper and lower flow aid region and average gas velocity and pressure

	Pellet Velocity (m/s)	**Void Fraction**	**Gas Velocity (m/s)**	**Gas Pressure (Pa)**
Upper Flow Aid Region	0.13	0.33	0.23	10.98
Lower Flow Aid Region	0.36	0.37	---	---

6.7 Discussion

Modeling the baseline operation of the DRI feed system provides insight for what the conditions within the feed system are when operating properly, and allows for comparison of the conditions within the system under different operating conditions.

The results show that for the baseline case the bulk flow is quasi-steady for 7 seconds after the 4 seconds it takes to become steady. Jamming is a probabilistic phenomenon, meaning that a steady flow has a certain probability of suddenly jamming at any given time. Running the simulation at the timescales necessary to determine the probability of jamming is not feasible. For example, the system may run with similar operating conditions for months then suddenly jam, while simulation only captures 7 seconds of operation. The study will use this short steady window of time to capture the formation of a jam and what conditions lead to the formation.

The mean velocity of the pellets increases as the pellets descend through the hopper as is expected. The flow rate of pellets is constant through the shrinking longitudinal cross-sectional area as they descend through the hopper which explains the increase in velocity.

The flow aid insert disrupts the flow of pellets and causes the void fraction to increase below it. The forces on the lower portion of the flow aid and on the walls, on the same level, drop significantly decreasing the probability of jamming in this region. The forces are high on the top

of the flow aid and are higher on the walls of the hopper at the upper half level of the flow aid and above, increasing the probability of jamming in this area.

The location of the higher forces on the walls and flow aid insert show where jamming is most likely to occur and coincide with where the flow is reported to be jamming. The void being lower and the velocity lower above the flow aid also indicate that this area is more likely to clog than below the flow aid. Overall, where the simulation shows the highest probability of jamming is the location where the feed system is reported to be jamming.

7. OPERATION WITH HIGH FRICTION

7.1 Background

It has been suspected that the moisture content in the feed system is impacting the friction between the pellets and causing the pellets to jam. Moisture has been shown to be important in the jamming of particulate flows via cohesive forces between the particles. When particles are wet and near each other a liquid bridge exists between the particles. The surface tension of, and a low-pressure zone within the liquid bridge creates a net attractive force between the particles. When the attractive force between the particles is significant relative to the weight and size of the particles, the bulk flow behavior changes significantly [51]. To quantify this phenomenon a relation called the Bond number (Bo) is defined as the ratio of the maximum total force exerted by the liquid bridge to the weight of the particle, where if Bo >> 1 the moisture has a strong effect on the bulk flow. The Bo number is defined as: strong if:

$$Bo \equiv \frac{F_{l,max}}{|\boldsymbol{F}_w|} = \frac{3\gamma_s}{2\rho_p g R^2} \tag{38}$$

With the term $F_{l,max}$ representing the max total force exerted by the liquid, $|\boldsymbol{F}_w|$ the magnitude of the force of gravity, γ_s the surface tension of the fluid, ρ_p the particle density, g the acceleration due to gravity, and R the radius of the particle.

Research conducted by Lanzerstorfer and Hinterberger has shown that increased moisture content in iron ore fines significantly reduces the flowability of the fines, reaching a peak reduction in flowability at approximately 3-5% moisture content and remaining constant at further concentrations [10]. The iron ore fines in their research had a mass median diameter of 20.1 µm, and thus have a Bo value much greater than 1.

Iron ore pellets are approximately 0.01m in diameter, many orders of magnitude larger than fines. An estimate of Bo for wet iron ore pellets is:

$$Bo \approx 0.113$$

For: $\gamma_s = 0.073$ N/m, $\rho_p = 3948$ kg/m^3, $g = 9.81$ m/s^2, $R = 0.005$ m

The Bo value is below 1, and given that Bo must be significantly larger than 1 to have an effect on the bulk flow. It can be concluded that moisture in the pellet bed does not introduce cohesive forces strong enough to impact the bulk flow of the pellets, and thus is negligible.

How moisture impacts the friction between iron ore pellets is not well documented. However, how friction changes between many rock types when wet is well documented. Consistently the friction between rocks is decreased when wet, as the water acts as a lubricant between the rocks [9]. Therefore, in the absence of direct measurements it is reasonable to assume that wet pellets would behave similarly.

Moist pellets and fines are often charged into the hopper. The moist pellets likely see a decrease in the friction between them, decreasing the probability of clogging, whereas the moist fines experience a reduction in their flowability, possibly increasing the chance of clogging. The net effect on the bulk flow of moist pellets and fines is not well documented.

7.2 Methodology

The methodology for modeling the flow within the feed system is essentially the same as the baseline. However, the flow of pellets accounting for moisture and fines is modeled by increasing rolling and static friction between the pellets. This is under the assumption that the net bulk flow effect of the charged wet pellets and fines is a higher resistance to shear forces within the material [52].

The computational domain and physics models selected are the same as the baseline. The pellet static and rolling friction coefficients are both raised to 0.90 assuming a large change in the resistance to shear forces. If jamming occurs while assuming a large increase in the resistance to shear forces than the exact friction levels where jamming begins to occur can be further explored by parameterizing the friction levels. The contact parameters accounting for the presence of moisture and fines is presented in table 22.

Table 22. High friction pellet coefficients to account for the presence of moisture and fines

	Pellet-Pellet Contact	Pellet-Steel Contact
Static Friction Coefficient	0.90	0.40
Coefficient of Restitution	0.48	0.39
Coefficient of Rolling Friction	0.90	0.25

7.3 Results

The forces on the flow aid for the high friction case became steady after around 10 seconds of flow time, and the average values presented for the results are calculated using the values across time after this 10 second point. The value of the forces is lower than what is seen in the baseline case. The average value of the force on the flow aid insert is 102.2 N, compared to 177.1 N for the baseline case. For the walls the average value of the force is 462.2 N, compared to 481.1 N for the baseline case. The high friction vs baseline case results for the forces on the flow aid insert and the walls across time are plotted in figures 46 and 47.

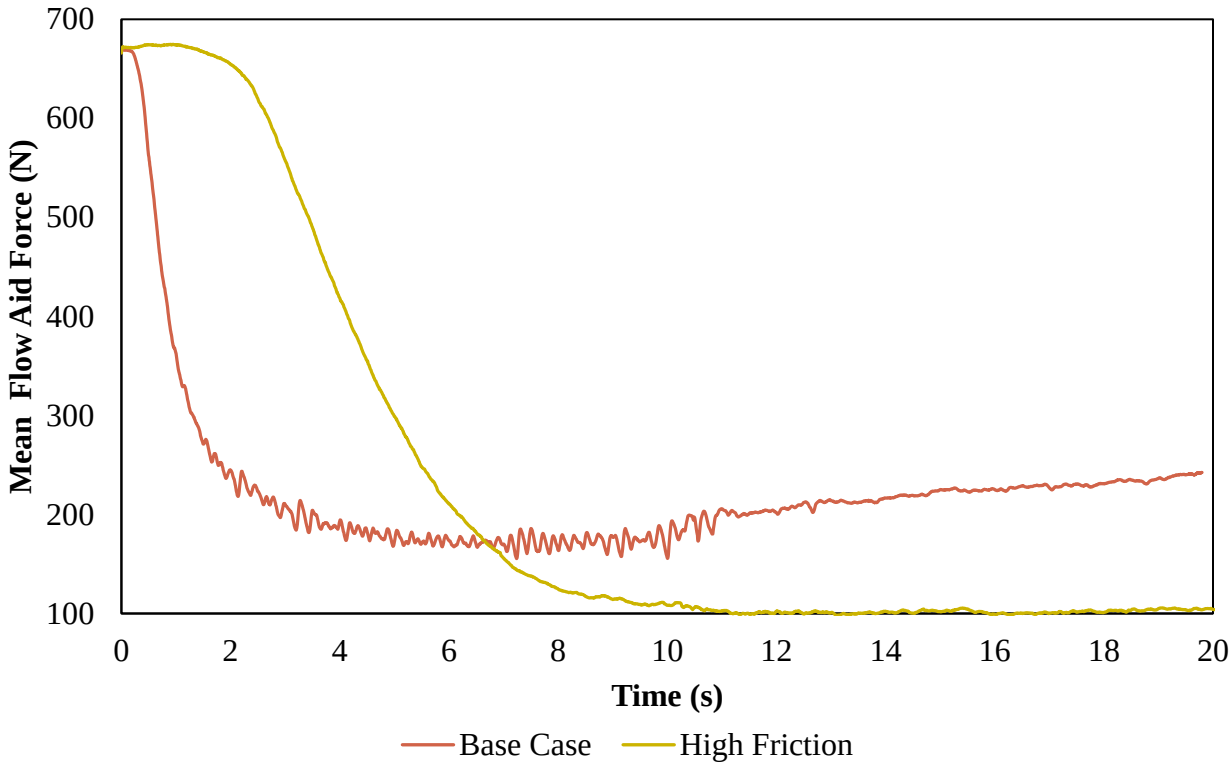

Figure 46. Plot of force on flow aid vs the baseline

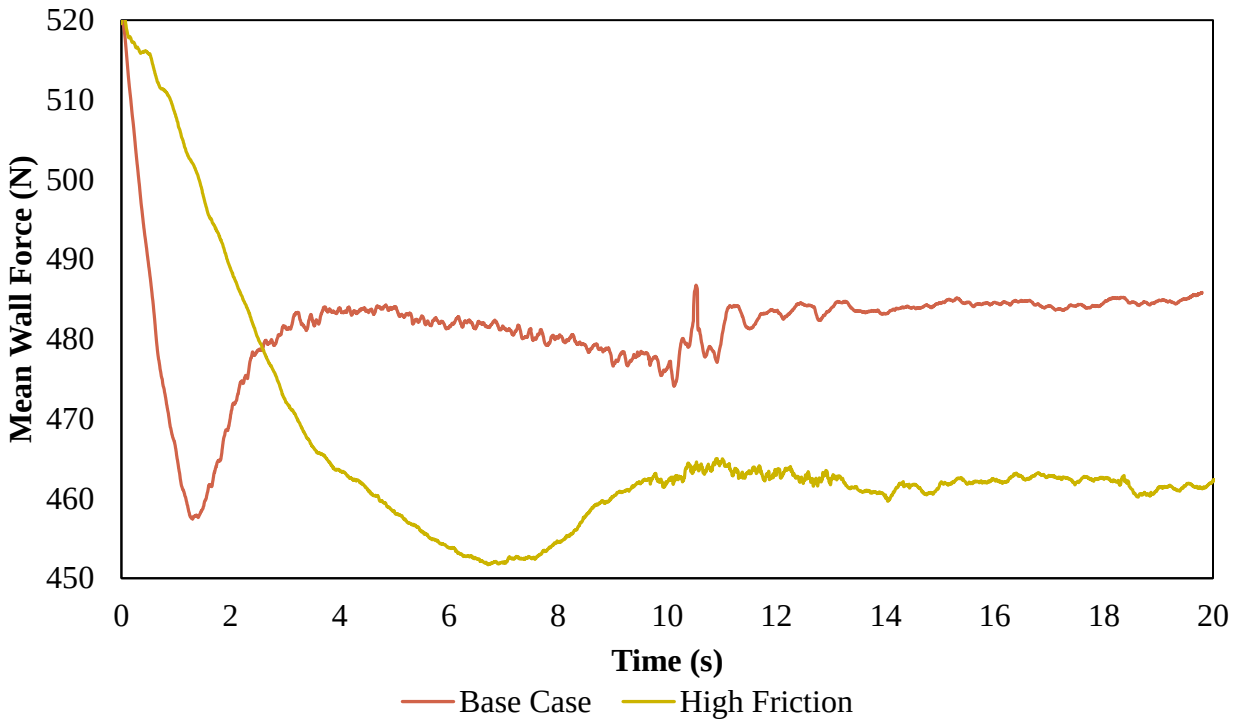

Figure 47. Plot of force on walls

The force distribution on the surface of the flow aid insert displays a similar pattern to the baseline case, shown in figure 48, with the forces being higher on the top of the flow aid insert and being very low on the bottom. However, the values of the force overall are lower than what is observed in the baseline case.

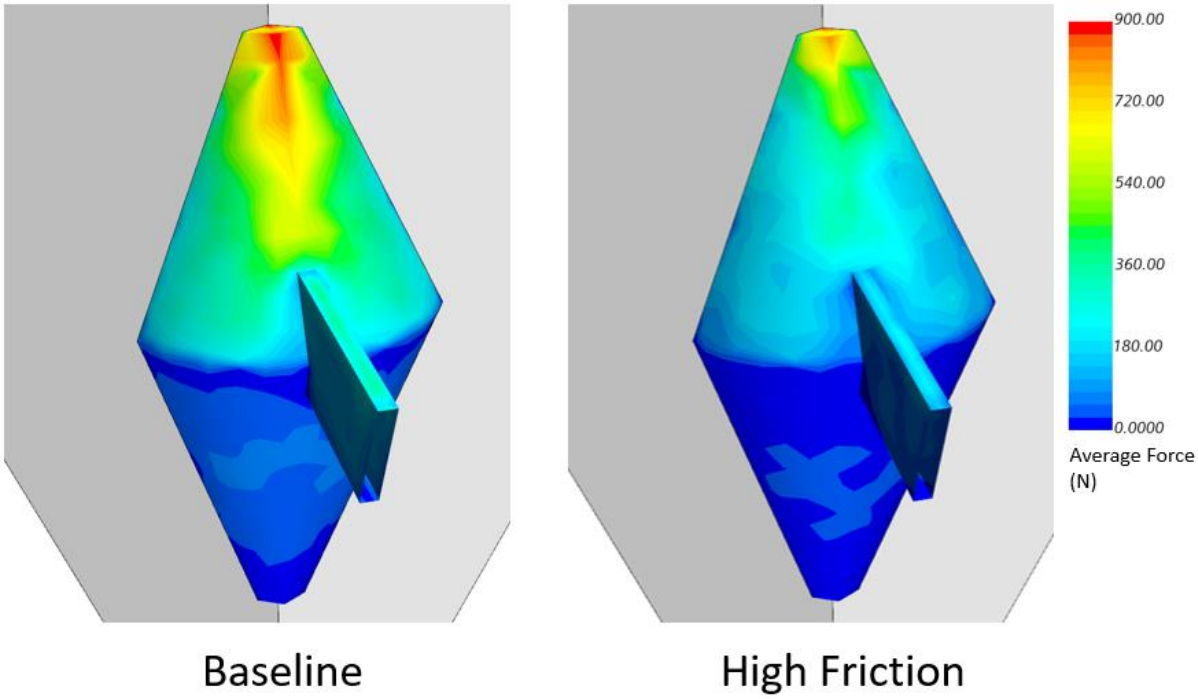

Figure 48. Forces on surface of flow aid of the baseline and the high friction case

The distribution of the forces on the walls of the hopper are also similar to the baseline with similar peak values, shown in figure 49. Both cases show higher forces on the walls above and near the level of the top half of the flow aid insert and a drop in the forces exerted on the wall near the bottom of and bellow the flow aid insert.

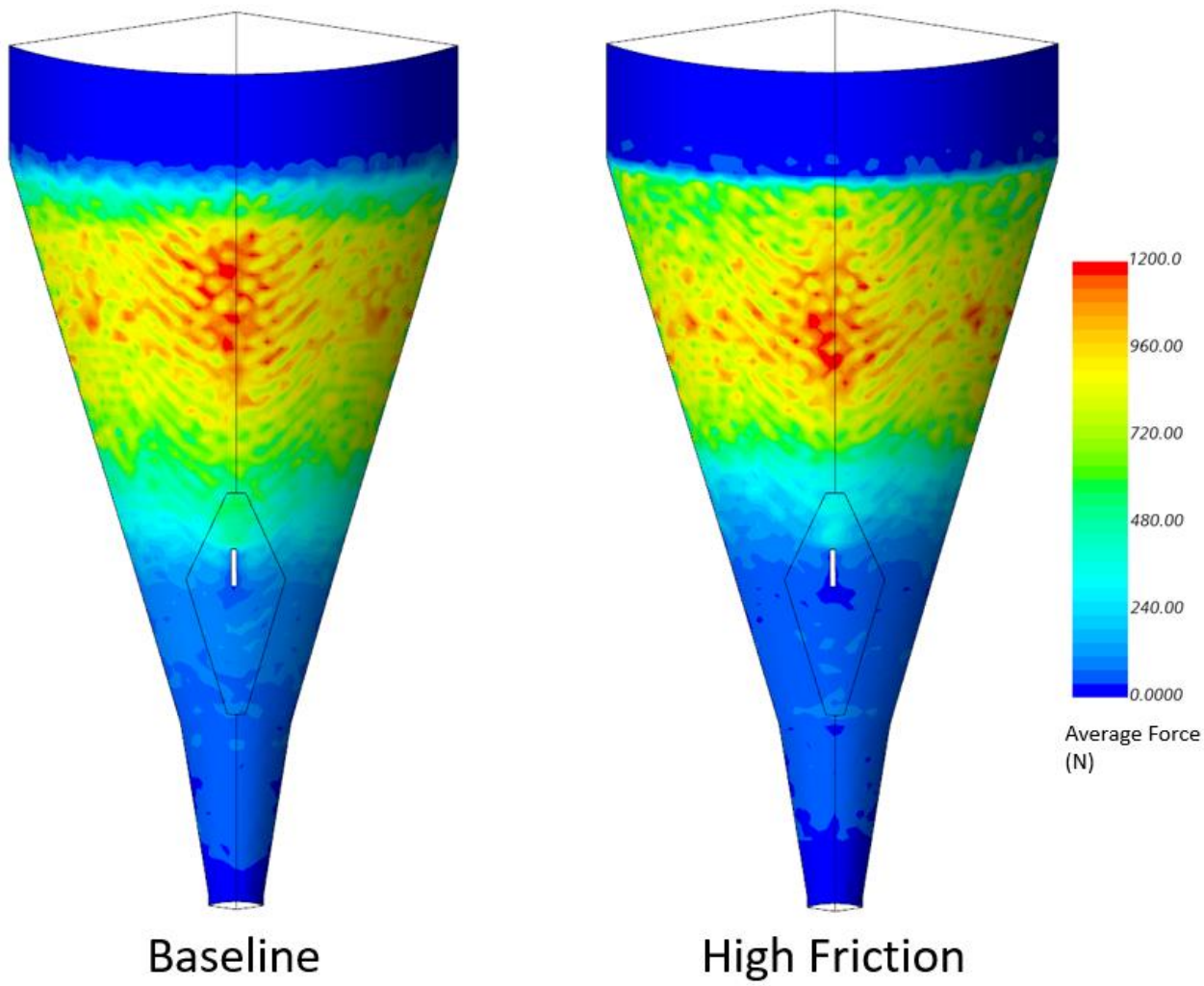

Figure 49. Forces on walls of the high friction case compared to baseline

The mean velocity of the pellets in the region near the upper flow aid did not vary as much as was seen in the baseline case, shown in figure 50. The average velocity of the high friction pellets in the upper flow aid region is 0.068 m/s, compared to 0.12 m/s for the baseline case.

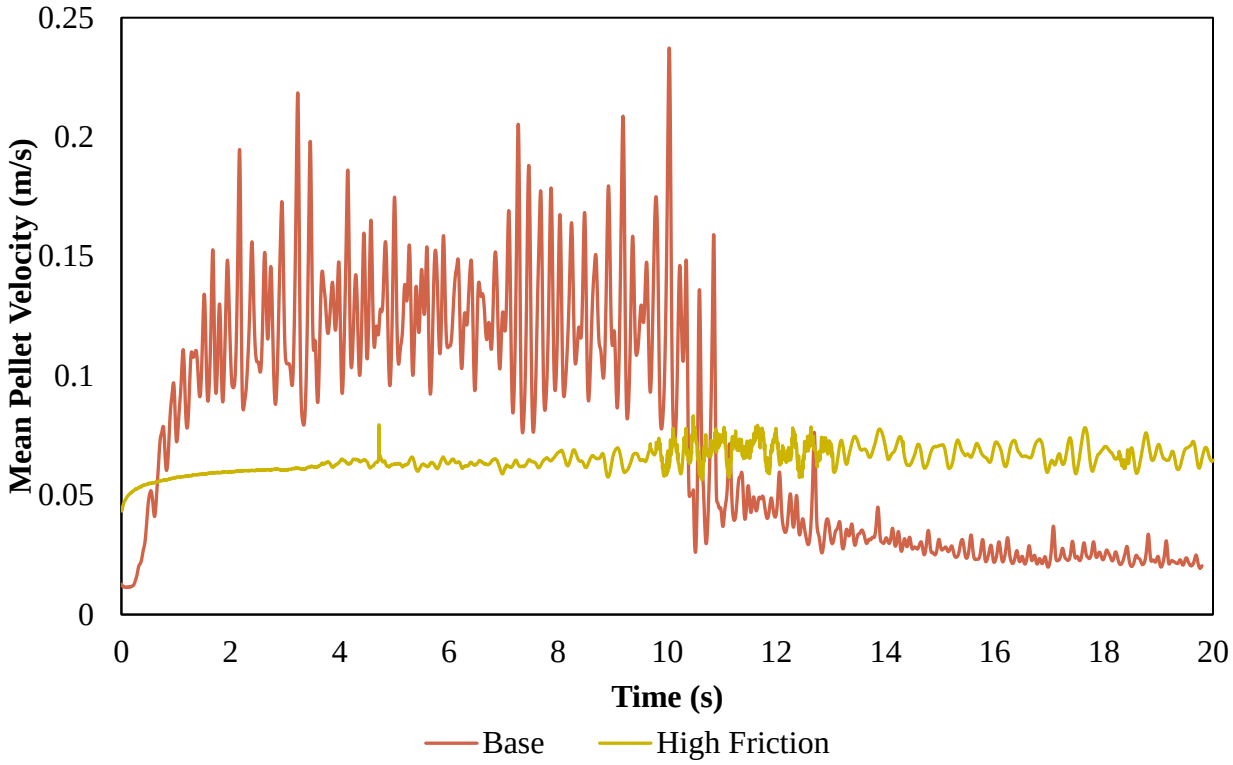

Figure 50. Mean pellet velocity near upper flow aid vs time

The void fraction in the upper flow aid region of the high friction case is higher than the baseline case, shown in figure 51. The average void fraction is 0.40, compared to 0.33 for the baseline case.

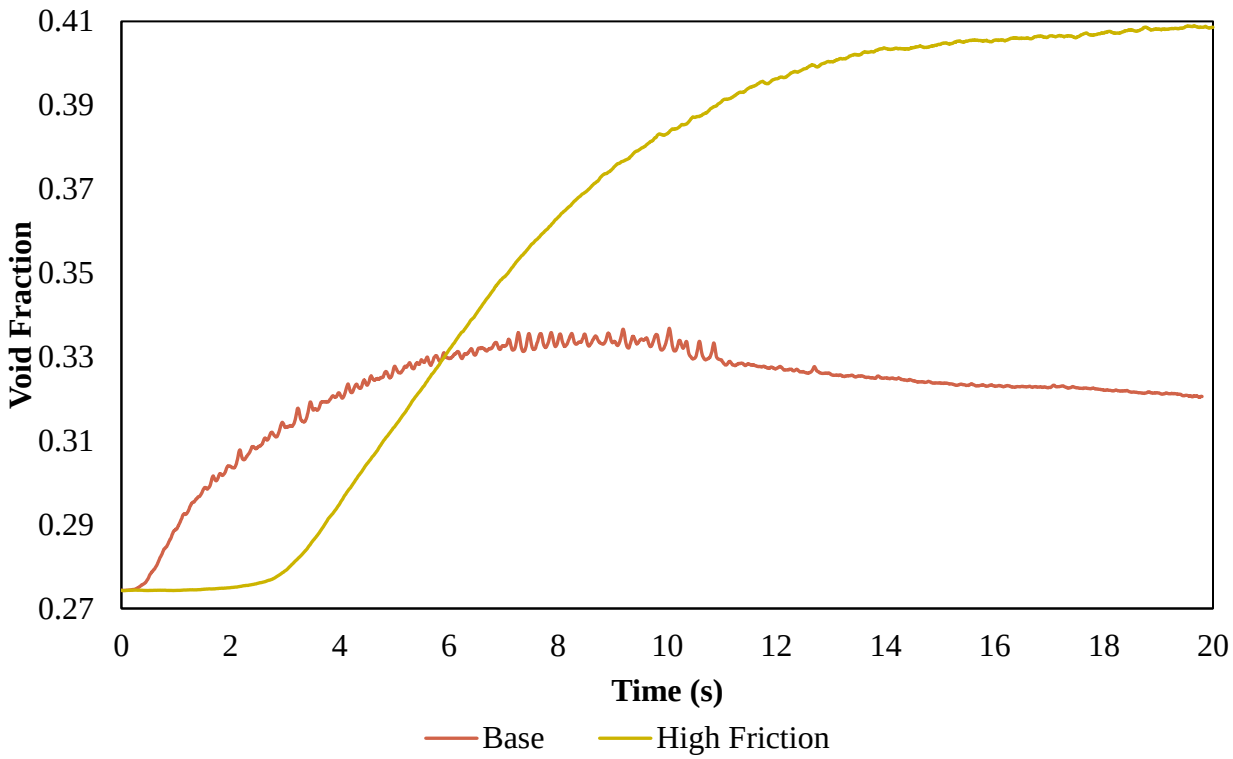

Figure 51. Void fraction in upper flow aid region

A contour of the void fraction through the hopper at the 9 second time point reveals that for the high friction case, the void fraction increases at a higher rate as the particles descend through the hopper than what is observed in the baseline case, shown in figure 52.

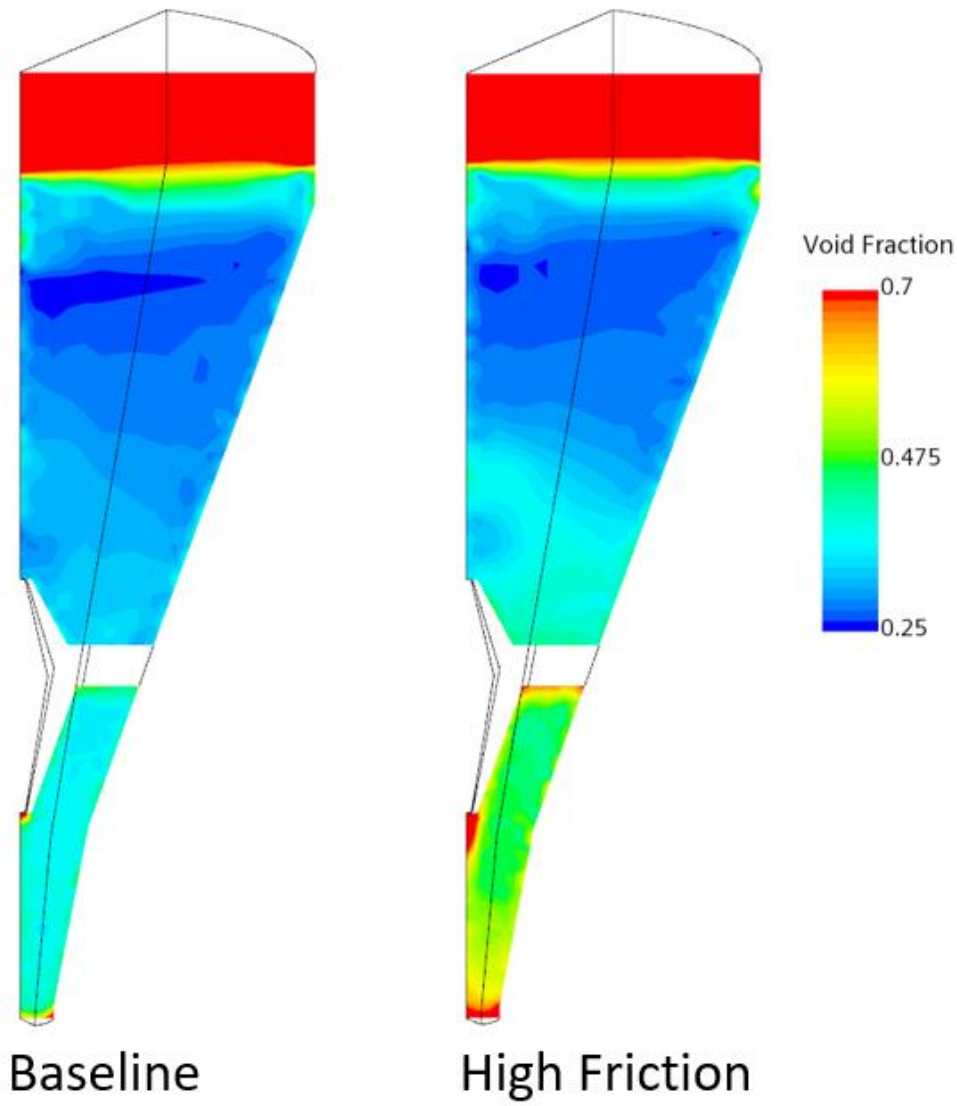

Figure 52. Void fraction cross section

Figures 53-55 show the velocity distribution of the pellets in the high friction case and the baseline case at the 9 second time point. The velocity profile in both cases changes from moment to moment, especially above the flow aid insert, and the profile at this exact moment is not representative of the profile across time in that region. However, it can be seen that the pellet velocity does decrease beneath the flow aid insert for the high friction case when compared to baseline, which does happen to be representative of the change across time in this region.

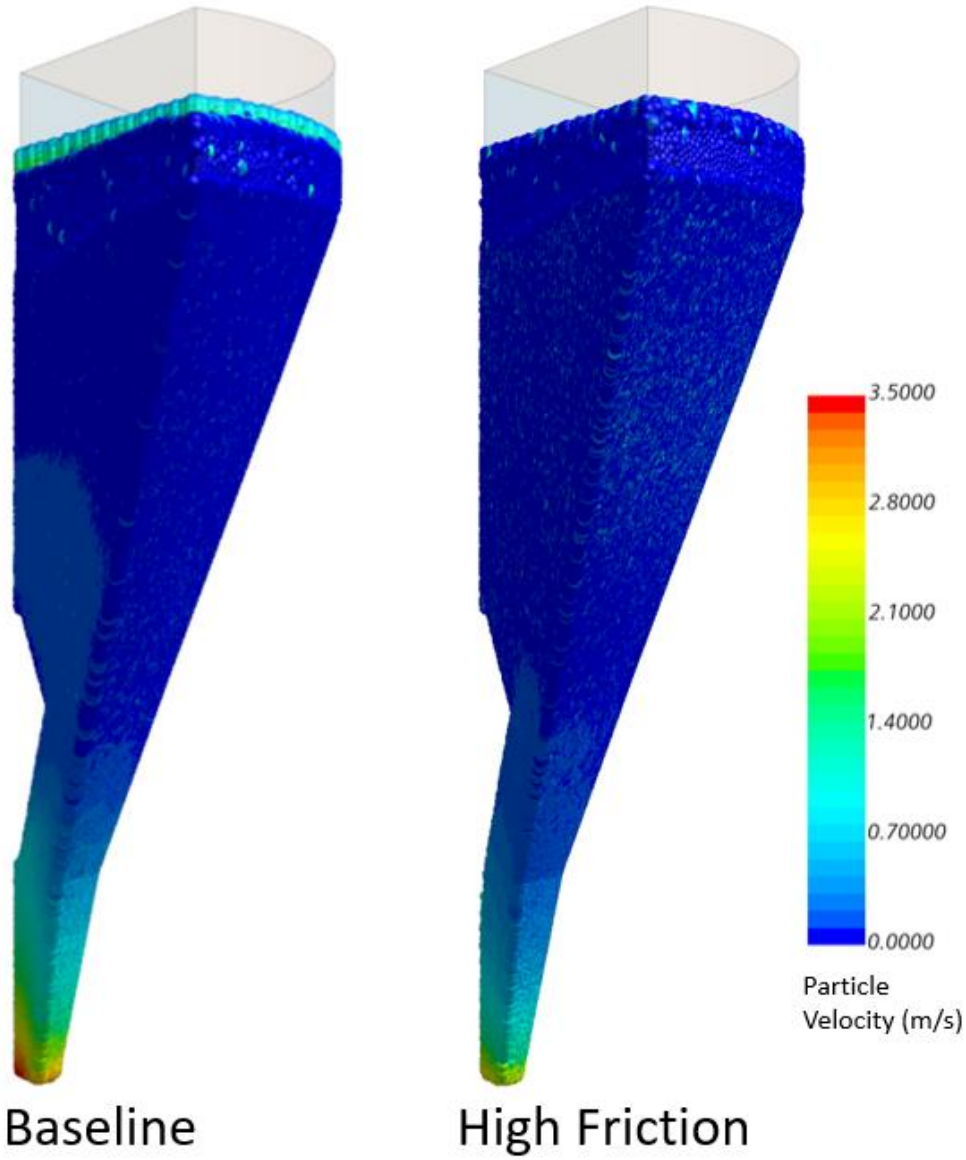

Figure 53. Pellet velocity magnitude side view

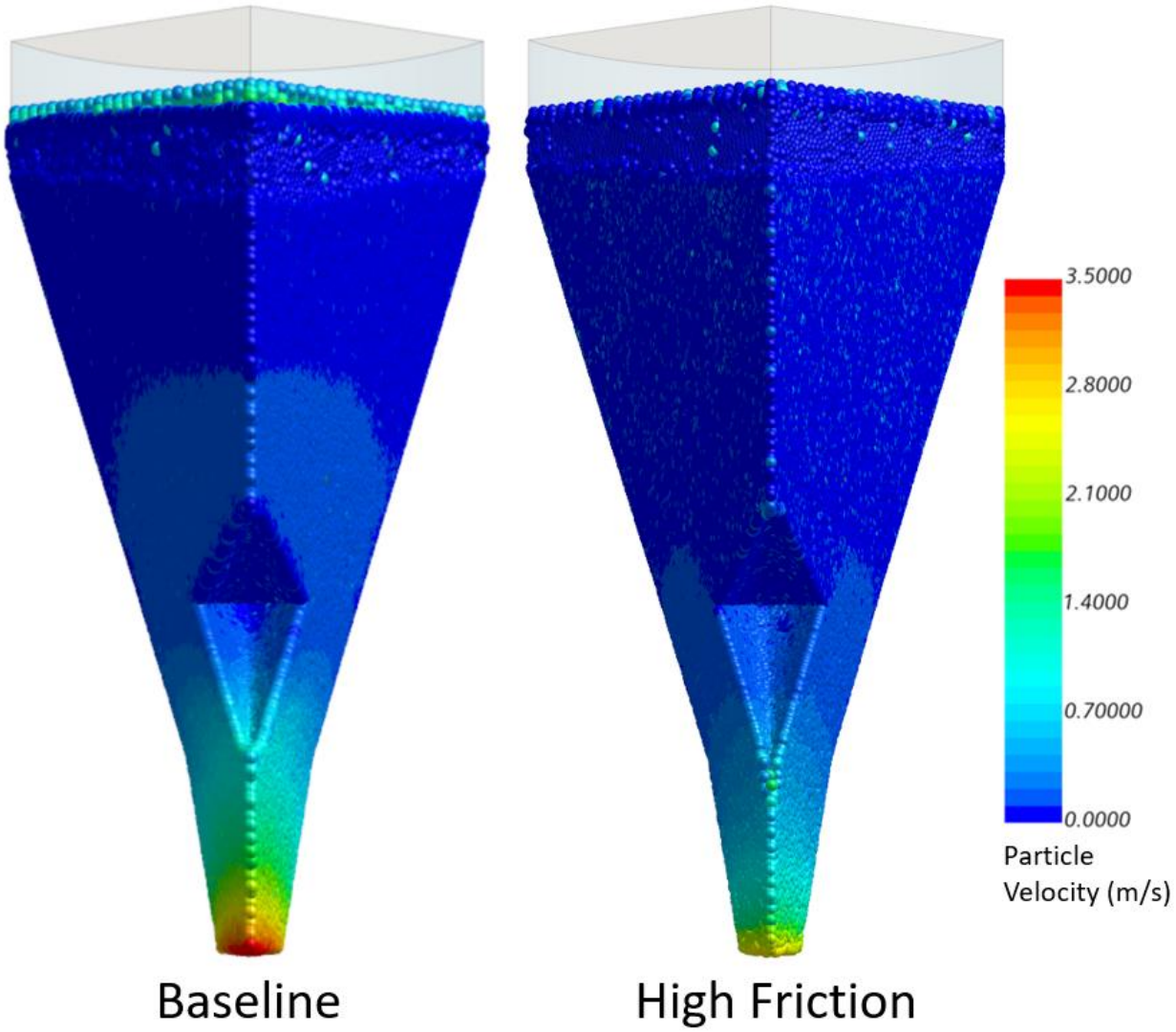

Figure 54. Pellet velocity magnitude inside view

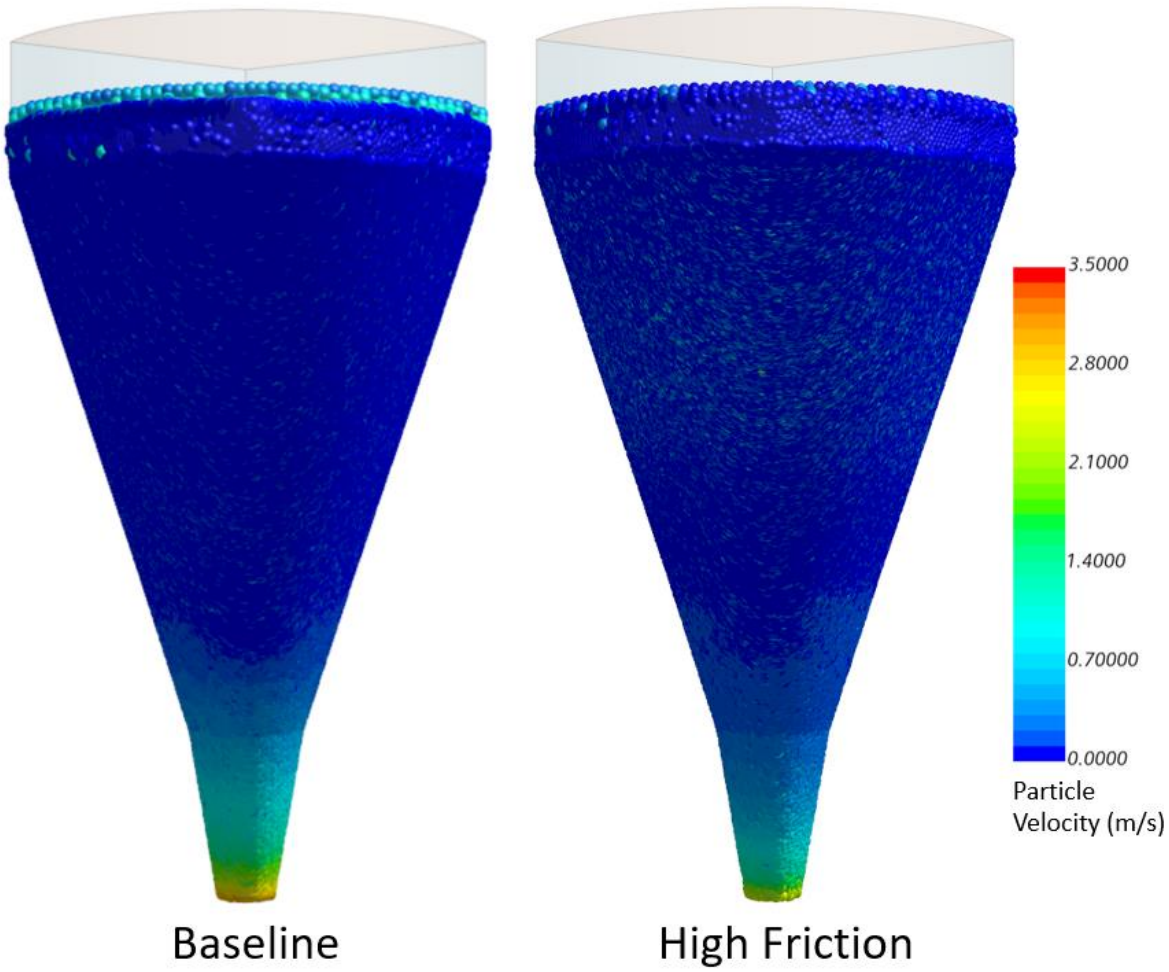

Figure 55. Pellet velocity magnitude front view

The pellet velocity in the lower flow aid region of the hopper is more consistent than what is seen in the baseline case, shown in figure 56. Like the baseline case the velocity is higher than what is seen in the upper portion of the hopper. The average pellet velocity in this region is 0.18 m/s, compared to 0.36 m/s in the baseline.

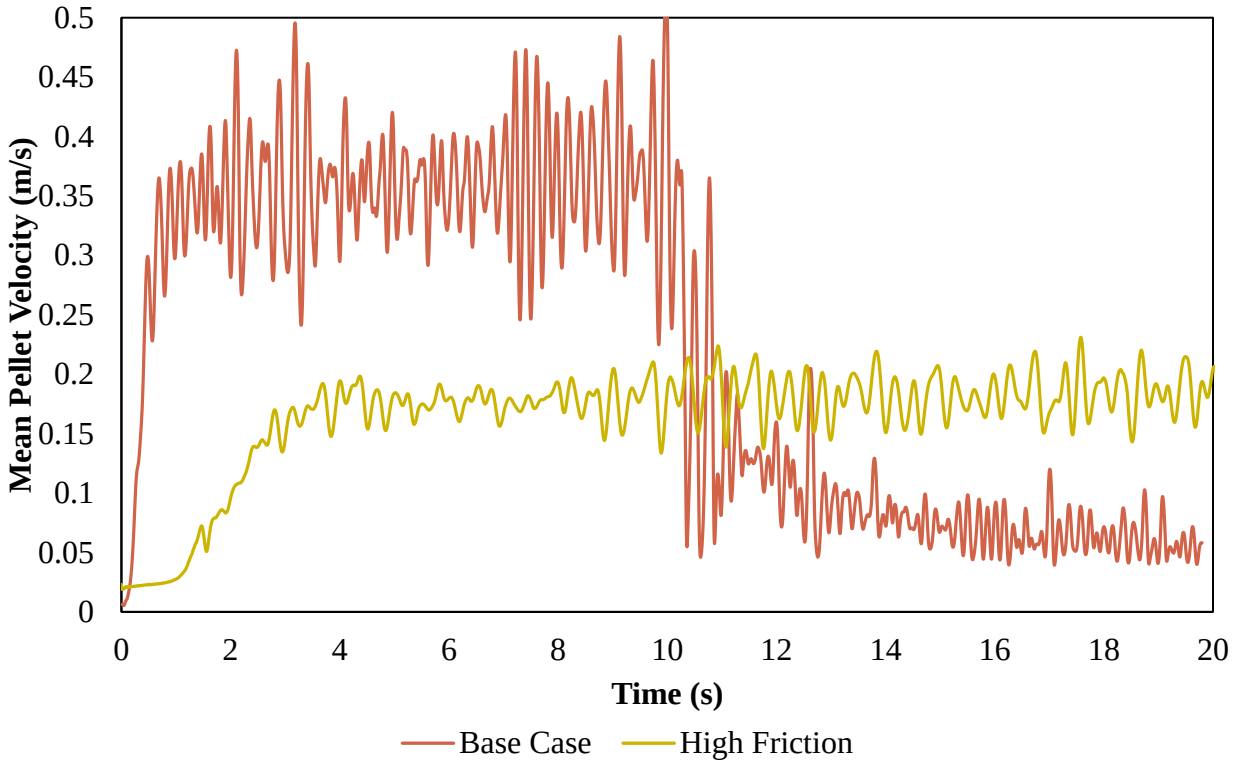

Figure 56. Pellet velocity below flow aid vs time

The void in the lower flow aid region of the hopper is also higher for the high friction case, shown in figure 57. The average value of the void fraction is 0.45, compared to 0.37 for the baseline case.

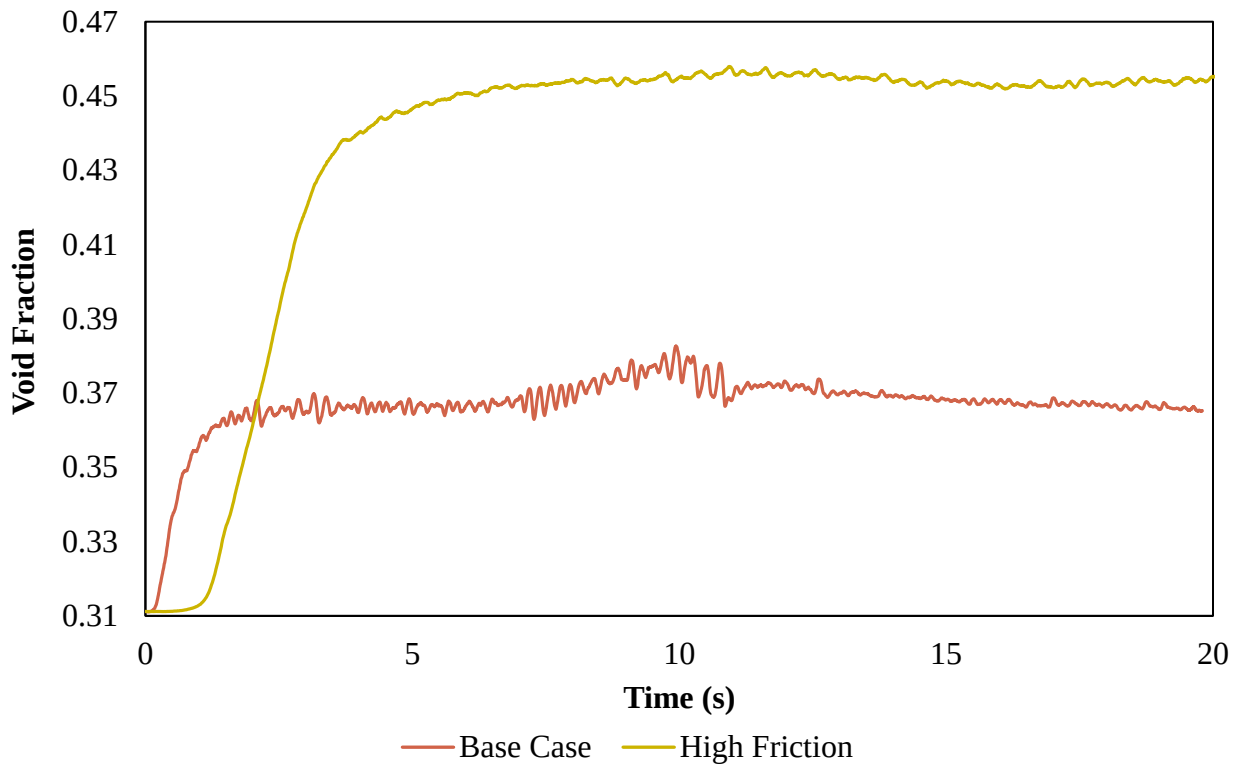

Figure 57. Void fraction below flow aid vs time

The average gas velocity in the region near the upper portion of the flow aid insert for the high friction case was very similar to that of the baseline case shown in figure 58. The average gas velocity is 0.20 m/s, compared to 0.23 m/s for the baseline case.

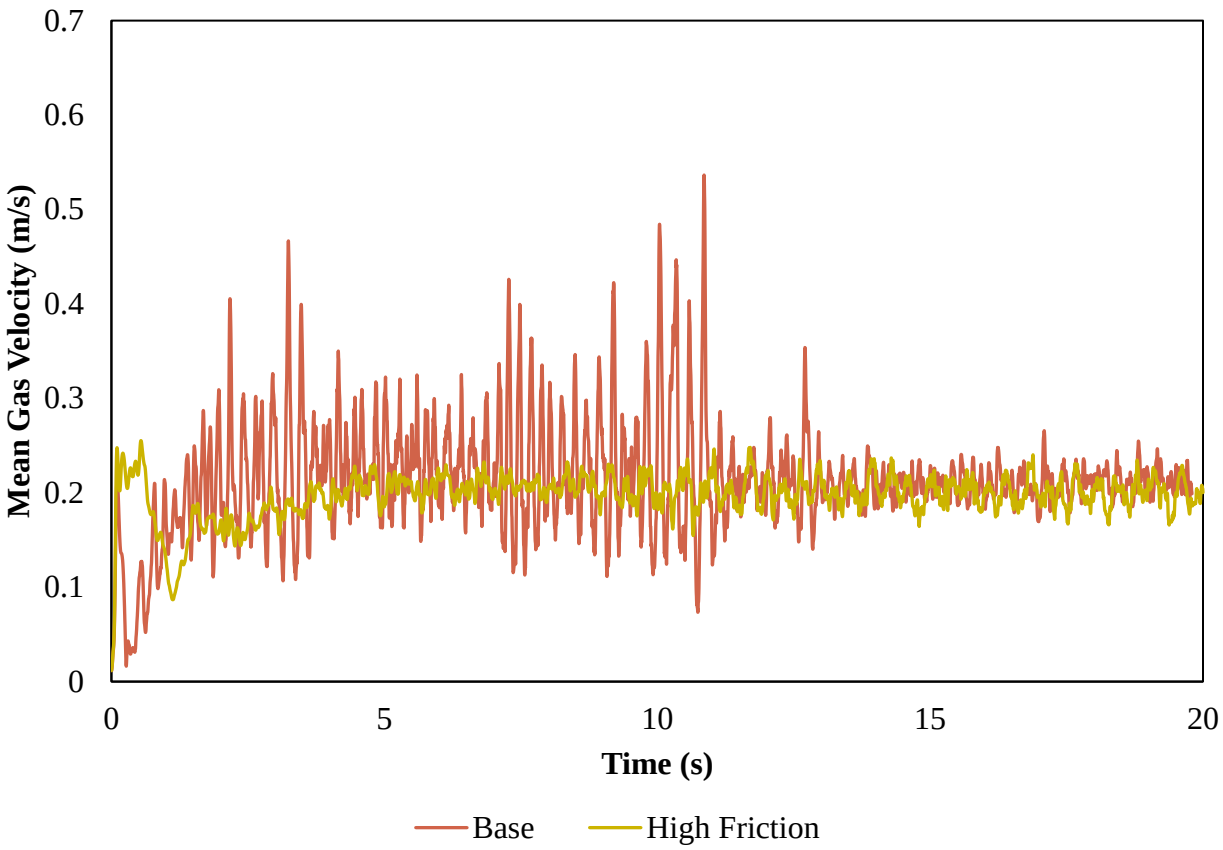

Figure 58. Mean gas velocity near upper flow aid region vs time

The average gas pressure near the upper flow aid region of the for the high friction case is similar to that of the baseline case, but the values across time do not fluctuate as much, shown in figure 59. The average value of the gas pressure is 6.13 Pa, compared to the baseline value of 10.98 Pa.

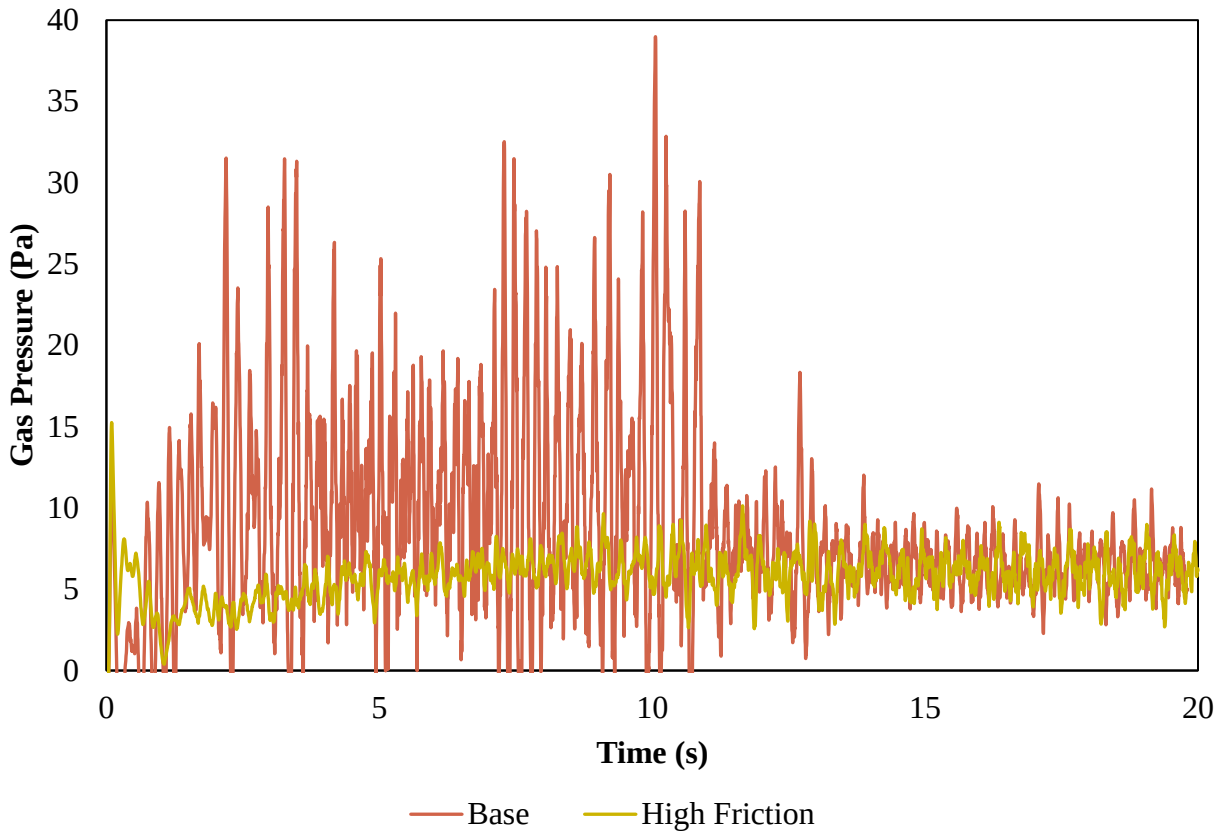

Figure 59. Gas pressure near upper flow aid region vs time

The average values for the pellet velocity, and void fraction near the top and bottom of the flow aid insert, along with the average gas velocity and pressure for the high friction case are shown in table 23. And the percent change of these values from the baseline case are shown in table 24.

Table 23. The pellet velocity, void fraction, gas velocity and pressure for the high friction case

	Pellet Velocity (m/s)	**Void Fraction**	**Gas Velocity (m/s)**	**Gas Pressure (Pa)**
Upper Flow Aid Region	0.07	0.40	0.20	6.13
Lower Flow Aid Region	0.18	0.45	---	---

Table 24. Percent change from baseline for pellet velocity, void fraction, gas velocity and pressure

	Pellet Velocity % Change	**Void Fraction % Change**	**Gas Velocity % Change**	**Gas Pressure % Change**
Upper Flow Aid Region	-46.2	22.2	-12.2	-44.1
Lower Flow Aid Region	-49.5	23.1	---	---

7.4 Discussion

No jamming effect was captured for the high friction case. This case assumes that the bulk flow effect of moisture on pellets containing fines is an increased resistance to shear forces. The increased resistance is represented by increasing the friction between the pellets. A decrease in the friction is not explored as decreased interparticle friction has been repeatedly shown to reduce the probability of jamming.

The velocity of the pellets as they descend through the hopper decreases. The decrease in velocity may imply that the hopper is operating at a higher probability of clogging, but the phenomenon was not captured with the rolling and static friction coefficients set at a high value of 0.9. The void fraction throughout the pellets is increased in the region where jamming is expected, which may imply that the hopper is operating at a lower probability of jamming. The forces on the top of the flow aid are lowered while the forces on the walls are very similar when compared to baseline operation. Increased pressure on the walls within a hopper has been correlated with an increased probability of jamming. The forces being lowered on the flow aid and the same on the walls suggests that the chance of bridging of the material is similar or lower than the baseline case.

The jamming of the flow has been reported to be happening in the winter months, and not during other times of the year. Pellet moisture would vary year-round as the pellets are stored outside where they are exposed to precipitation all year.

Given the simulation results and the fact that the clogging happens under winter conditions, a strong case for moisture being the sole cause of the clogging cannot be made. Exploring phenomenon that would be present during winter months and not others should be considered.

It should also be noted that there is also a need to validate the basic assumption made about the impact of moisture on the bulk flow with experimental work. The geometrically dependent effects of the fines within the flow are not directly captured as it is not computationally feasible. Still, these effects should be seen year around and the clogging is only reported during winter operation.

8. THERMAL MODEL DEVELOPMENT AND TESTING

8.1 Background

The initial assumption was that moisture is causing the jamming in the system, but given the results of the previous section, and the fact that moisture is a year-round phenomenon, that is unlikely the sole cause.

The pellets are stored outside and exposed to weather conditions year-round. The system is reported to be jamming in the winter, when pellets are exposed to wet and freezing conditions. Iron ore pellets, that have been frozen together from exposure to wet and freezing conditions in an ore pellet field, are shown in figure 60.

Figure 60. Example of pellets frozen together from being exposed to winter conditions in an ore field

Pellets that are frozen and wet are directly charged into the hopper. A hot counterflow gas passes through the pellet bed as they descend. It is assumed that a steady thermal profile exists in

the bed of pellets as they descend. If cold wet pellets are continuously charged with frozen pellets the thermal profile in the hopper may change such that there is not enough heating, and the freezing of pellets may begin to take place in the hopper and jam the flow.

The next step is to develop a model that accounts for freezing and melting of ice that adheres the pellets together. The model needs to be capable of at least 5 things listed:

1. Adhering and releasing pellets together at given temperatures
2. Exchanging heat between the gas and solid using proper heat transfer coefficients
3. Representing the thermal properties of wet and icy iron ore pellets
4. Account for the phase change from ice to water without introducing a third phase
5. Representing the steady thermal profile within the hopper domain

The next sections seek to build and test the capability of such a model in a computationally efficient manner. To do this small test cases are built to test the functionality of the model to then be implemented in the full domain.

8.2 Thermal Test Case 1

8.2.1 Methodology and Case Set Up

A model is created linking an additional cohesive force between pellets to the temperature of the pellets. The model will apply a cohesive force to the pellets when the temperature of the pellets is below the freezing point of water to replicate the effect of pellets being frozen together. A test case was created by modifying the drop test case to show that pellet cohesion could successfully be connected to the temperature of the particles and disrupt the flow. The pellets were set to the default material properties and contact parameters for the default rubber material in StarCCM+, and the pellet diameter is uniform set at 0.01m.

The energy model is turned on, and the drop test is charged with pellets at 223 K and 500 K, shown in figure 61. No heat transfer was allowed for this case, and the rest of the physics models selected along with the boundary conditions are the same as the drop tests (see section 4.3). The pellets below 273.15 K trigger an additional cohesive force whereas the pellets above 273.15K experience no cohesive force.

The drop test is repeated in the same manner as the drop test (see section 4.2).

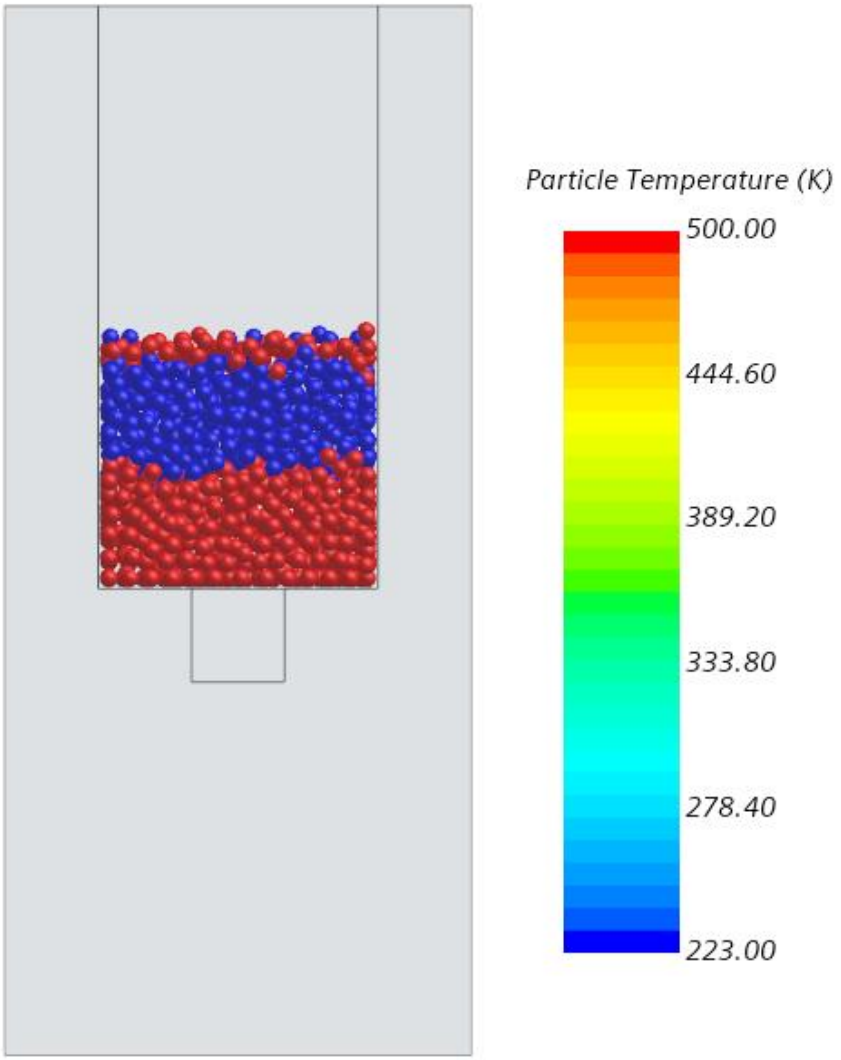

Figure 61. Drop test filled with a single material at two different temperatures

8.2.2 Results

The door is opened and the pellets above freezing temperature fall freely through the door, whereas the pellets below freezing temperature formed a blockage and obstructed the flow, as shown in figure 62.

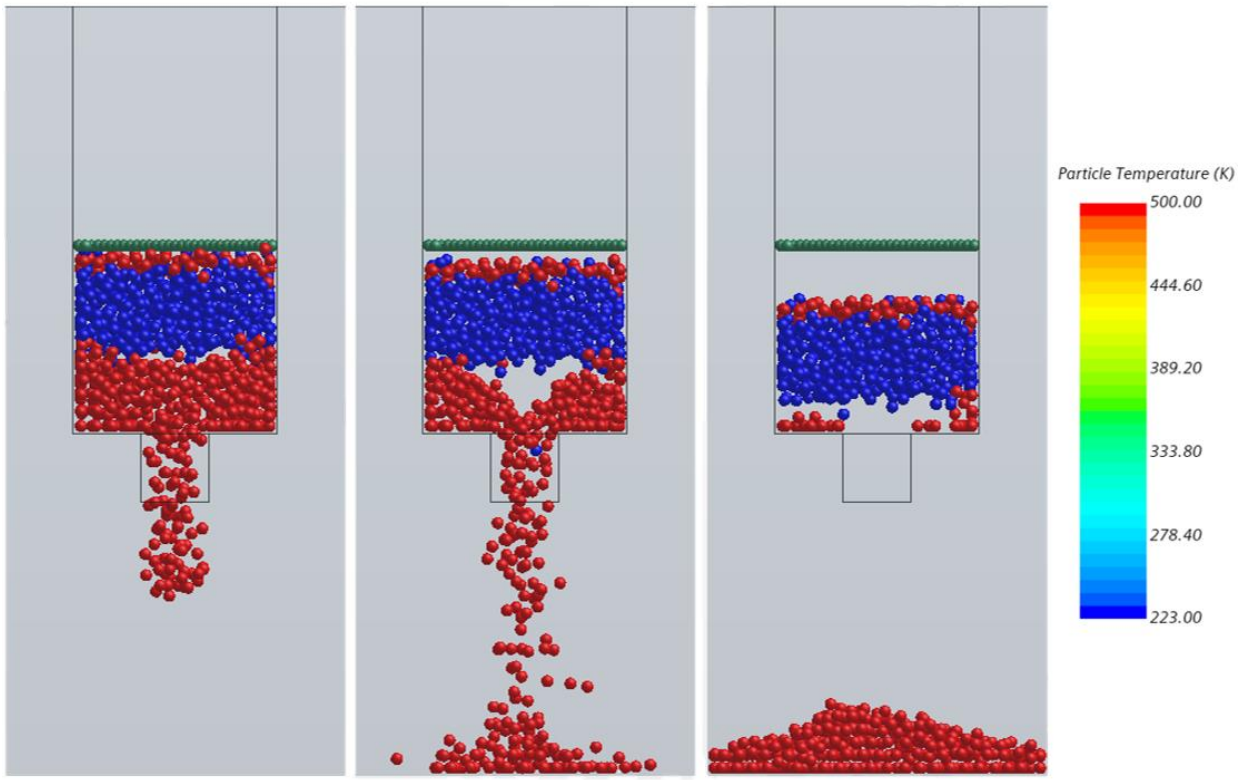

Figure 62. Pellets below ice melting temperature forming a blockage in the drop test

The results show that the cohesive force can be linked to the temperature of the particles, and demonstrate the concept of linking the cohesive force to temperature to model frozen pellets jamming the flow.

8.3 Thermal Test Case 2

8.3.1 Methodology and Case Set Up

To test the heat transfer between the fluid and solid phases, the drop test was again modified so that the bottom wall of the domain is a gas inlet that does not allow pellets to pass through, and the drop test is charged with pellets that are just below freezing temperature. The mesh and boundary conditions are shown in figure 63. A plane is defined longitudinally bisecting the hopper to display gas phase contours of temperature shown in figure 64.

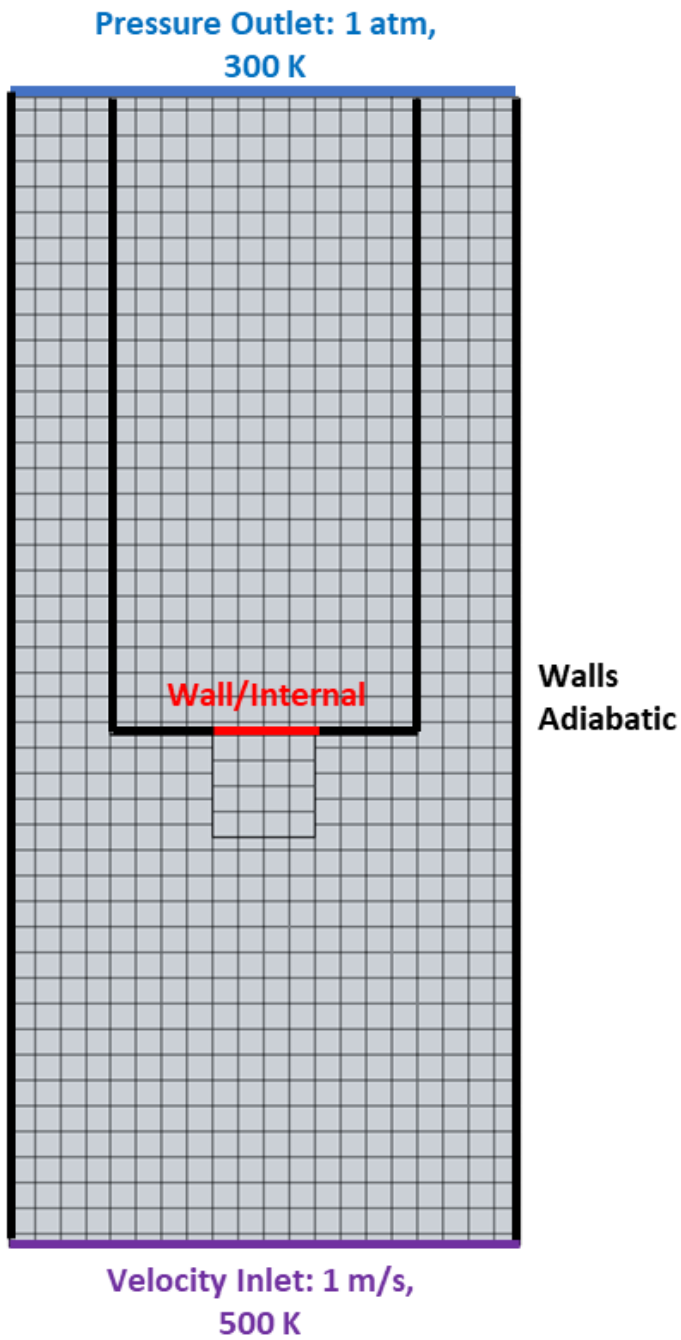

Figure 63. Modified drop test domain for testing heat transfer to frozen pellet blockage

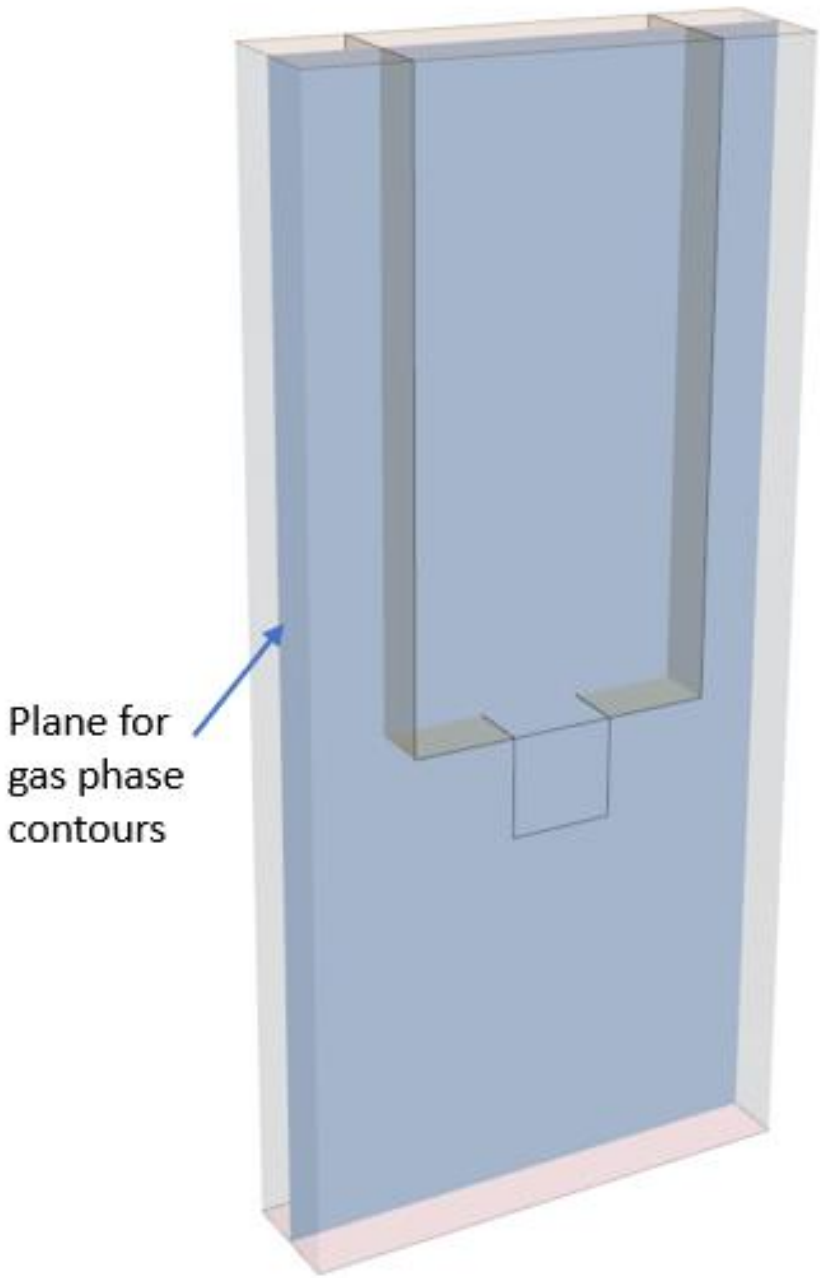

Figure 64. Plane to show the gas contours

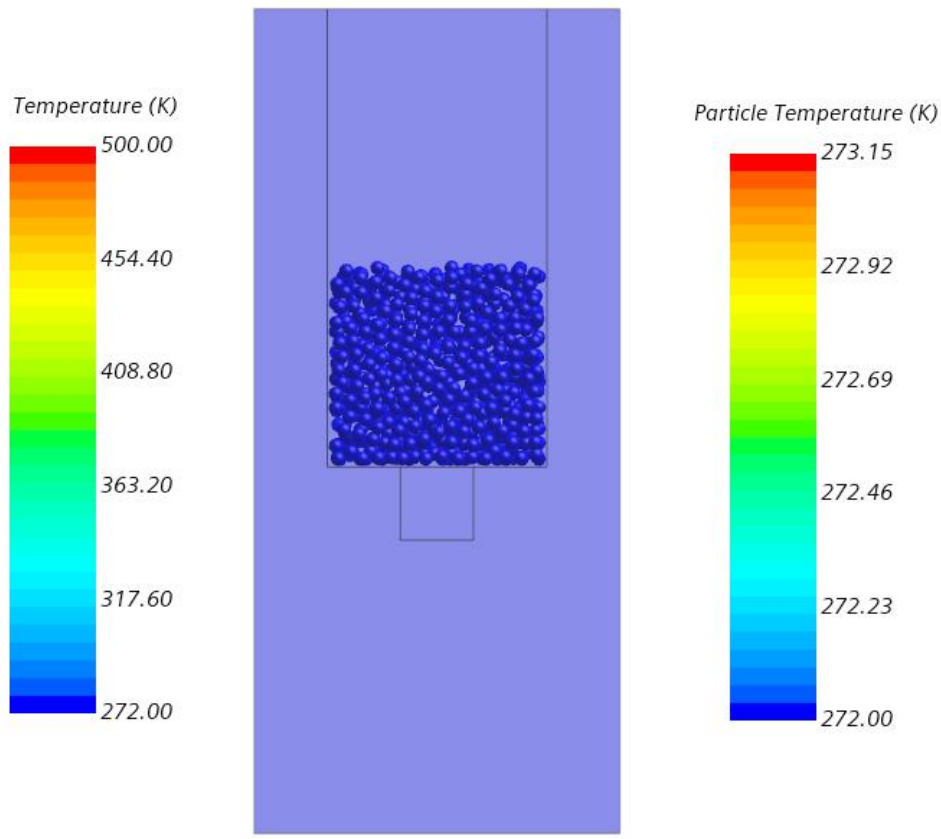

Figure 65. Drop test charged with pellets at 272.0 K and continuous phase initialized at 272.0 K

The pellets were charged into the drop test at 272 K and the gas phase was initialized at the same temperature, shown in figure 65. The pellets are charged with a cohesive force between them and when the pellets reach 273.15 K the cohesive force value becomes 0. The walls of the domain and the walls holding the pellets are set as adiabatic. The bottom wall is changed to a gas inlet boundary moving air at 1 m/s at 500 K, and does not allow pellets to pass through. The top outlet is a pressure outlet set to 1atm at 300 K.

The material properties were again left as default properties. The pellet diameter is uniform at 0.01m. The same physics models are used, but conduction and convection are considered. The default settings for the heat transfer coefficient are used.

8.3.2 Results

The door is opened and the particles are frozen together and do not fall. Air at 500 K enters through the gas inlet at 1 m/s and heats the pellets. When the pellet temperature is above 273.15 K the cohesive force becomes zero allowing the pellets to drop, shown in figure 66.

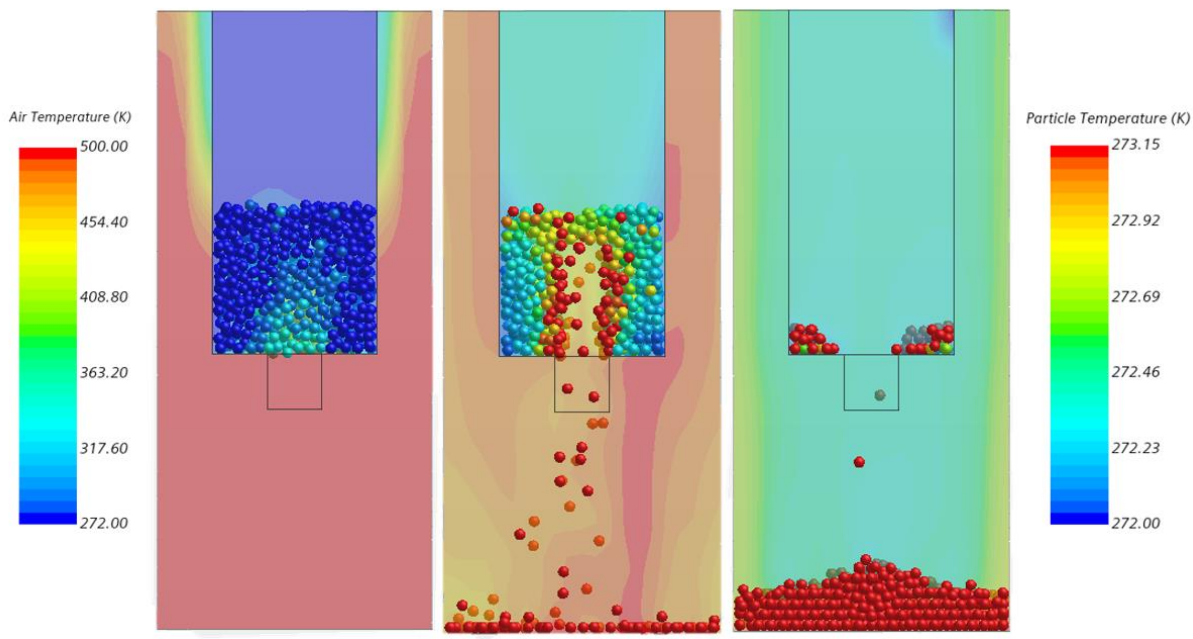

Figure 66. Heat transfer between solid and gas phases

The pellets heat to a temperature above 273.15 K, triggering the bond strength to become 0, and begin to flow. The change in gas temperature due to heat exchange with the pellets is observed. The pellets along the centerline of the domain above the drop hole heat first and fall through while the pellets near the walls heat after and fall through, showing that the pellets are individually heating and being released.

8.4 Thermal Test Case 3

8.4.1 Methodology and Case Set Up

The same test is repeated using the same physics models, but with the thermal properties and contact parameters of iron ore pellets applied to the pellets. The pellet specific heat is assigned

as a mass weighted average between the pellet and of the moisture content in the pellet, and accounts for the phase of the water, defined as:

$$c_{p,wet} = (1-\alpha)c_{p,pellet} + \alpha c_{p,water} \tag{39}$$

$$c_{p,icy} = (1-\alpha)c_{p,pellet} + \alpha c_{p,ice} \tag{40}$$

With the mass fraction of moisture denoted α and material specific heat values shown in table 25.

Table 25. Specific heat of pellets, water, and ice

Specific Heat Values (J/kg*K)		
Pellet ($c_{p,pellet}$)	**Water ($c_{p,water}$)**	**Ice ($c_{p,ice}$)**
560	4182	2093

Given that the max moisture content in a pellet is 0.055 the mass fraction of the pellet, the maximum specific heat value of the pellet is 759.21 J/kg*K when holding water and 644.3 J/kg*K when holding ice, shown in figure 67.

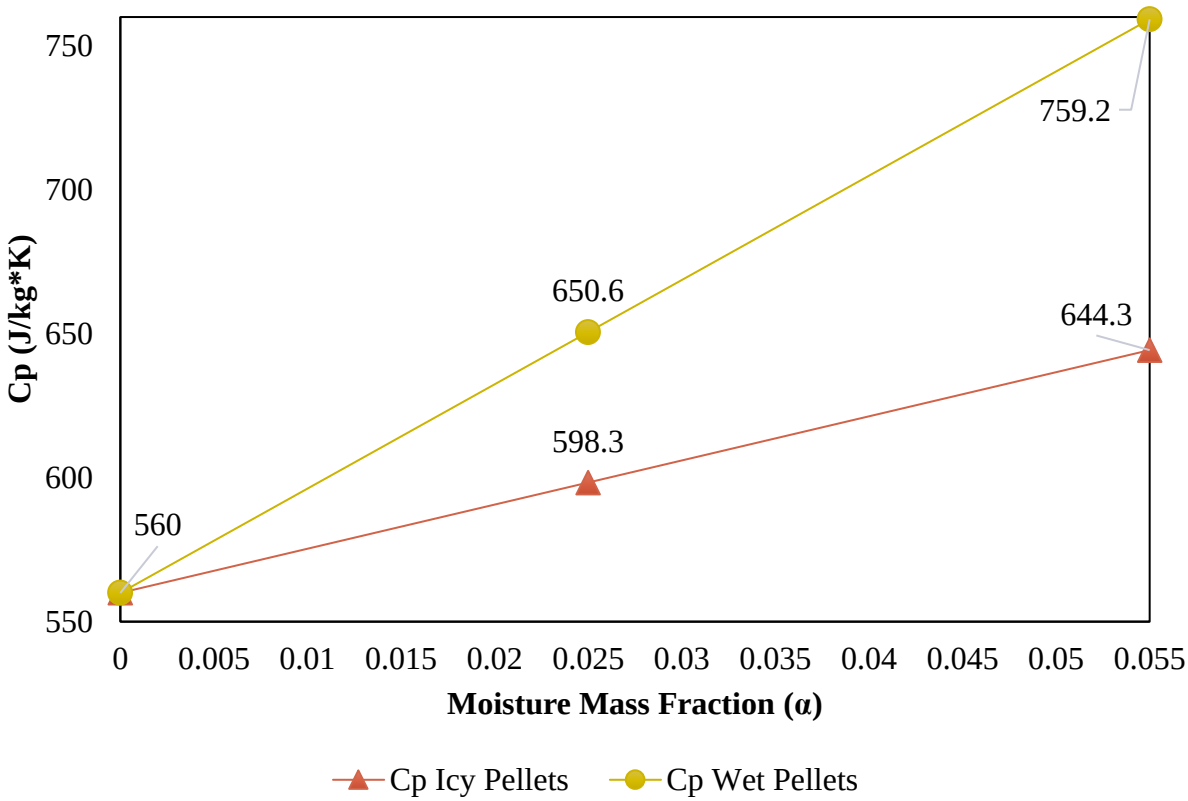

Figure 67. Specific heat values of wet and frozen the iron ore pellets vs moisture mass fraction

The pellet Cp value increases up to 35.6% when wet and 15.1% when frozen, agreeing with literature results that estimate an up to 40% increase in the Cp for wet pellets [T7].

The additional energy due to the latent heat of fusion, which describes the amount of energy required for a phase change from solid to liquid, is accounted for in the Cp value of the pellets as the temperature of the pellets change. This is to prevent added complications and computational expense of modeling a phase change taking place within the pellets.

The Cp is increased near the melting point between 272.15 and 273.15 K so that the energy required to raise the temperature from 272.15 K to beyond 273.15 K includes the additional energy required to produce a phase change from ice to water at 273.15 K. The relation derived to calculate the mass weighted Cp value in this range is:

$$c_{p,modified} = (1-\alpha)c_{p,pellet} + \alpha\left(\frac{h_{lf}}{\Delta T} + c_{p,icy}\right) \tag{41}$$

Where $c_{p,modified}$ is the specific heat modified to include the energy required to produce a phase change in the temperature interval of ΔT. The latent heat of fusion is denoted h_{lf}.

The value of $c_{p,modified}$ verses the pellet moisture mass fraction to be applied between the temperatures of 272.15 and 273.15 K ($\Delta T = 1$K) is plotted in figure 68.

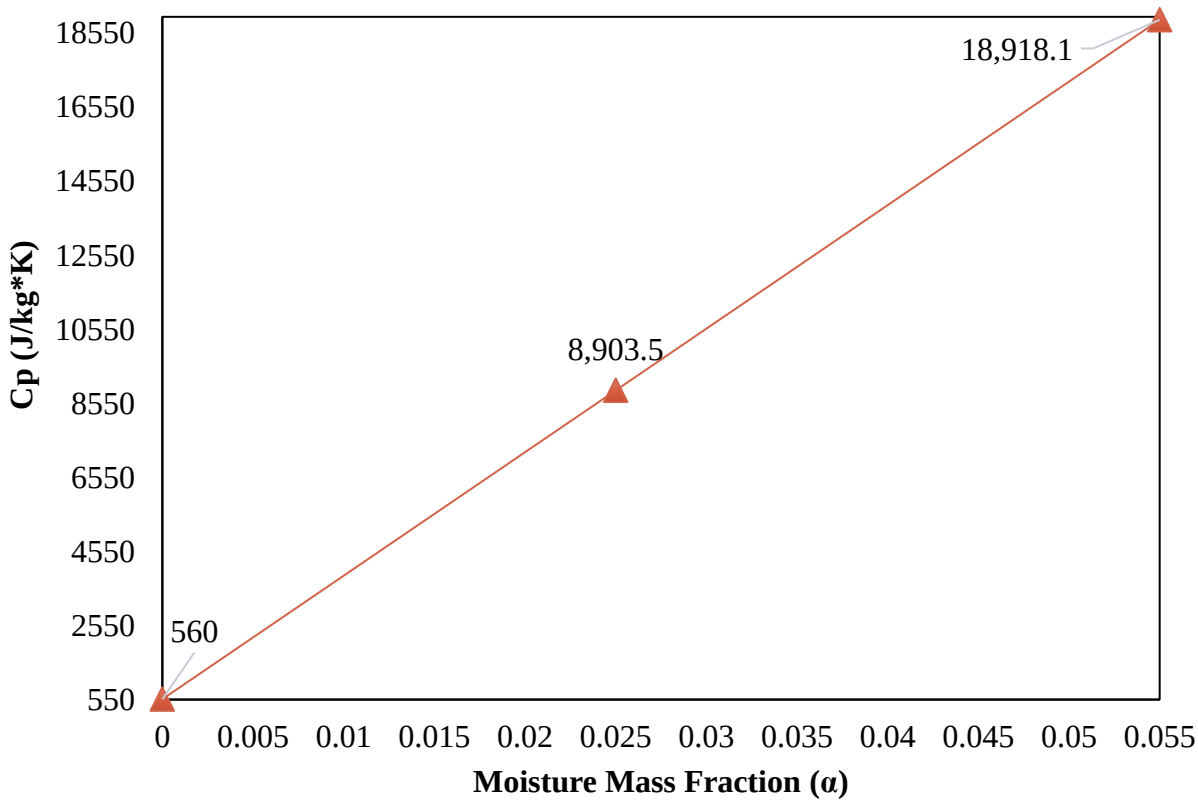

Figure 68. The specific heat values between 272.15 and 273.15 K to account for phase change vs the moisture mass fraction

The pellets were assigned a mass fraction of 0.025 water. The resultant Cp as it changes with temperature, and accounting for the phase change is plotted in figure 69.

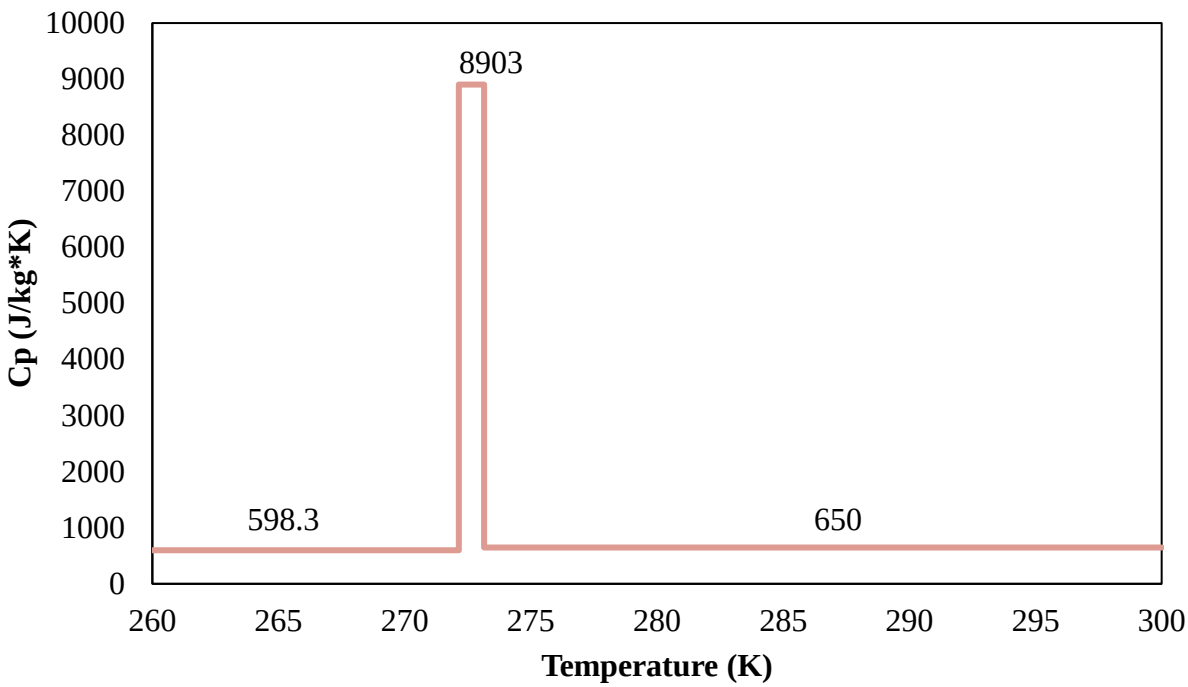

Figure 69. Specific heat mass weighted average pellets containing 0.025 mass fraction water and accounting for the phase change

The thermal conductivity of the pellets is not greatly impacted by the moisture level of the pellet [8] and has a chosen value of 1.2 W/m*K assuming a porosity of 25% [53].

The Nusselt number relation appropriate for the convective heat transfer to the pellets is a validated relation used for packed and fluidized beds and is given by:

$$Nu_p = 2.0 + 1.2{Re_p}^{1/2}Pr^{1/3} \tag{10}$$

With the particle Reynolds number defined as:

$$Re_p = \frac{\rho v D_p}{\mu} \tag{42}$$

Where ρ, v, and μ are the surrounding fluid density, velocity, and kinematic viscosity, and D_p is the particle diameter.

The previous test case was re-run with the thermal properties applied to the pellets, using a moisture mass fraction of 0.025, and the proper Nusselt number relation implemented for the convective heat transfer. For this case the pellets were allowed to pass through the bottom gas inlet.

8.4.2 Results

The results show a similar heating pattern as the previous test case and show heat transfer between the pellets and between the pellets and the gas phase. The gas and pellet temperatures are shown in figure 70, and the gas velocity along with the heat transfer coefficient of the pellets are shown in figure 71.

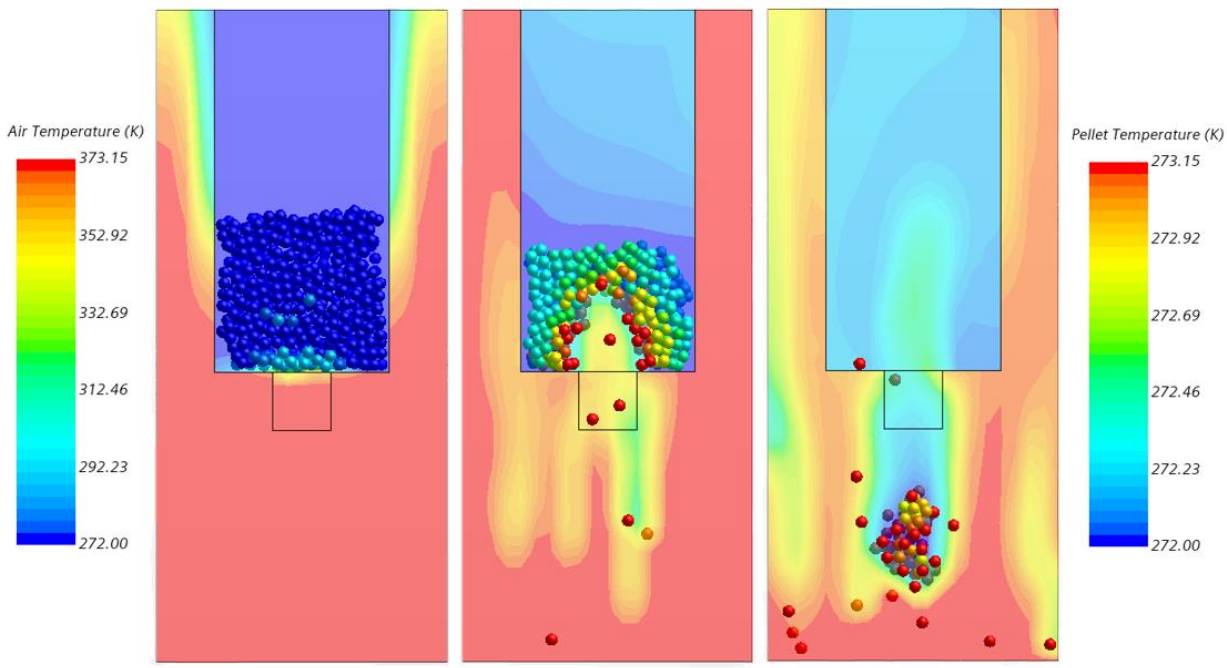

Figure 70. Gas and pellet temperatures during heating and dropping

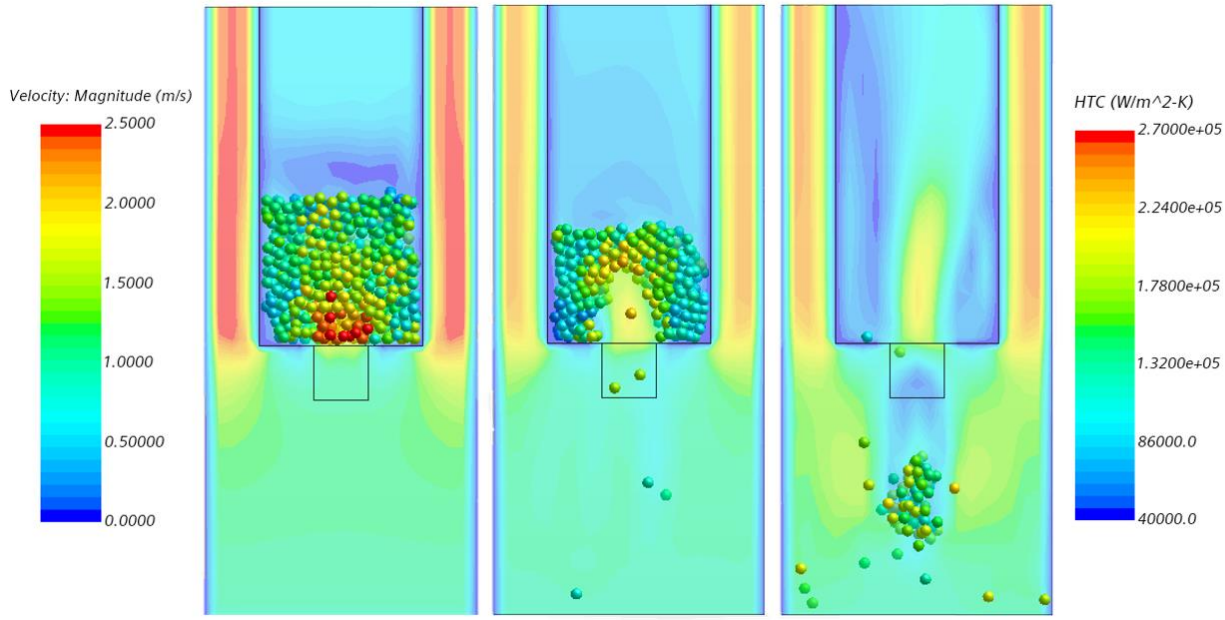

Figure 71. Gas velocity and heat transfer coefficient of the pellets during heating and dropping

The results of this test suggest that the model created is capable of representing the heating of pellets that are frozen together and obstructing the flow, allowing the pellets to freely flow.

8.5 Thermal Profile Development Cases

8.5.1 Methodology and Set Up for Cases

It is assumed that when cold pellets are charged into the hopper and descend with the hot counterflowing gas passing through them a steady temperature profile develops in the bed of pellets. The hot gas heats the pellets and cools as it flows through the bed and out of the hopper, while the pellets are heated and carry energy out of the hopper. It is not known how long it takes to develop the steady temperature profile, and because the base case only has 7 seconds of steady flow time, it is not feasible to run the baseline with heat transfer models applied until a steady profile develops. The possibility of heating the pellets before the flow of pellets begins, to a temperature profile similar to that of steady operation, is explored.

To determine how the temperature profile of the pellets develops in the hopper, two cases were created using the 1/3 hopper domain from the computational cost study, shown in figure 74.

One case was charged with pellets at 265.15 K and the other at 272.15 K, with both having a hot counterflow gas with a temperature equivalent to that used in operation. In both cases the walls are adiabatic and the hopper opening is defined as a pressure outlet at 1 atm, with the outlet temperature being equivalent to the charged temperature of the pellets.

The pellets flow out of the domain at a controlled rate and the domain is continuously charged with more pellets at the same rate. The mass flow rate of the test cases is scaled according to the mass ratio of this charged case to the baseline, which is 8.35E-03, and the mass flow ratio of the pellets out of the hopper and gas into the hopper is kept the same as the baseline case. The time the cases are run for is the full residence time of the pellets.

Another case with pellets at temperature of 265.15 K was run without allowing the pellets to leave the domain and no continuous feed of pellets. The counterflow gas is still present and at the same operational temperature.

The cases are referred to as thermal profile cases 1, 2 and 3. The boundary conditions are presented in table 26, and the domain presented in figure 72.

Table 26. Boundary conditions for thermal profile cases 1-3

	Outlet Pressure (atm)	**Outlet Temperature (K)**	**Charged Pellet Temperature (K)**	**Wall Heat Flux (W/m^2)**	**Gas/Pellet Mass Flow Ratio**
TP-Case 1	1	265.15	265.15	0	0.007
TP-Case 2	1	272.15	272.15	0	0.007
TP-Case 3	1	265.15	265.15	0	No Pellet Flow

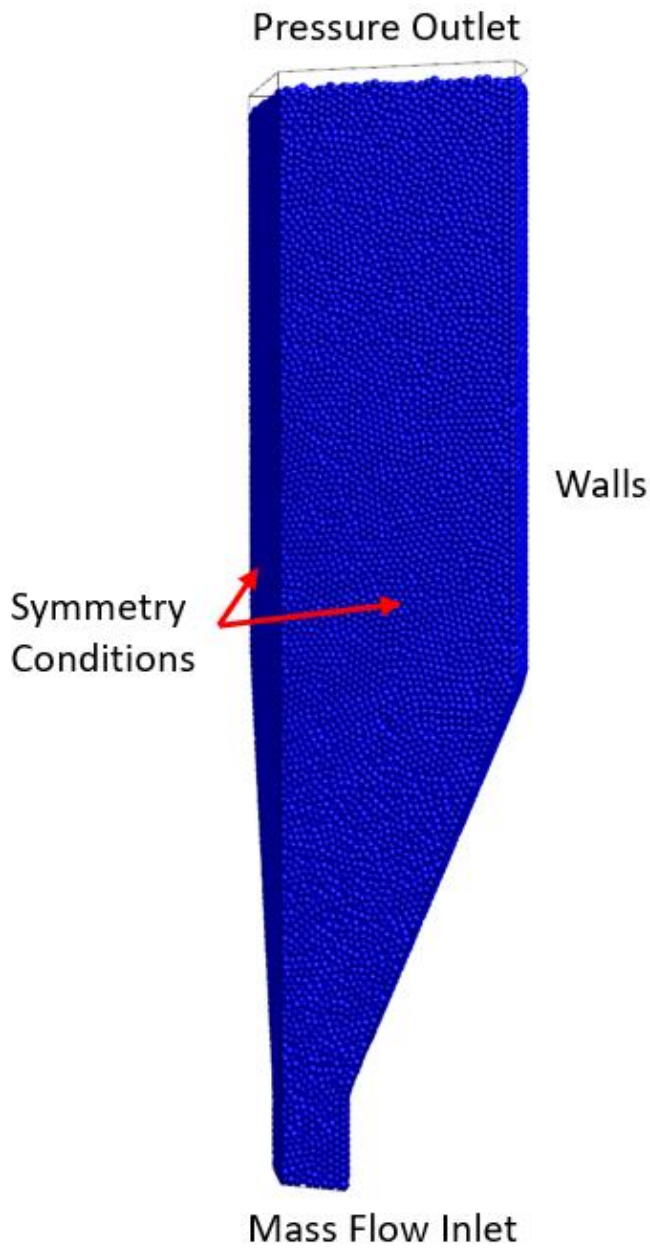

Figure 72. Filled hopper and boundaries labeled

Each of these simulations are coupled DEM-CFD simulations. Conduction heat transfer between the pellets and convective heat transfer between the pellets and the gas phase is modeled. No cohesion between the pellets is modeled. No radiative heat transfer is modeled as radiative heat transfer in packed beds is negligible in this temperature range, with convective heat transfer being the dominant mode [T10].

The pellets are modeled as having no moisture content and use a constant Cp value of 560 J/kg*K. The iron ore pellet material properties and contact parameters used in the baseline case are applied to the pellets. The pellet thermal properties and moisture content are shown in table 27.

Table 27. Specific heat, moisture content, and thermal conductivity of the pellets

Pellet Moisture and Thermal Properties		
Specific Heat (J/kg*K)	**Moisture Content**	**Thermal Conductivity (W/m*K)**
560.0	0.0	1.2

The average temperature of the pellets descending in the cone section of the hopper is tracked against time to compare how the temperature profiles develop. The section where the pellet temperature is monitored is shown in figure 73.

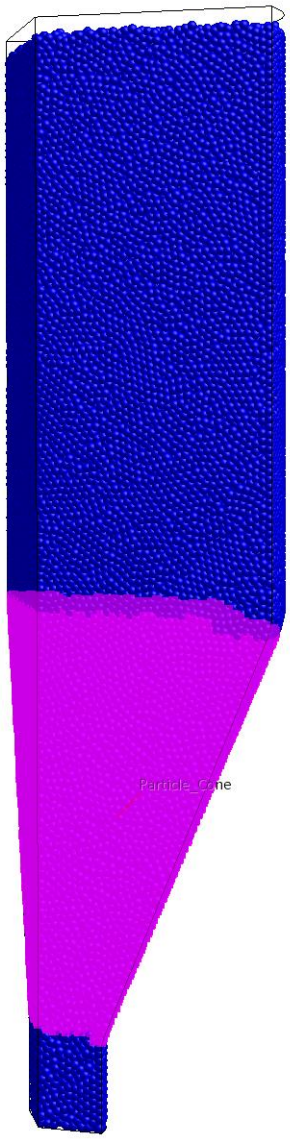

Figure 73. Highlighted region where pellet temperature is tracked

8.5.2 Results

For both thermal profile cases 1 and 2 there was no change in the average temperature across the entire particle residence time. The gas entering the hopper quickly approaches the temperature of the pellets and the pellets receiving the energy quickly leave the domain. This finding suggests that the amount of energy supplied to the pellets through the gas is not capable of heating the pellets in winter conditions. Gas and pellet temperature profiles of thermal cases 1 and 2 are shown in figures 74 and 75, respectively.

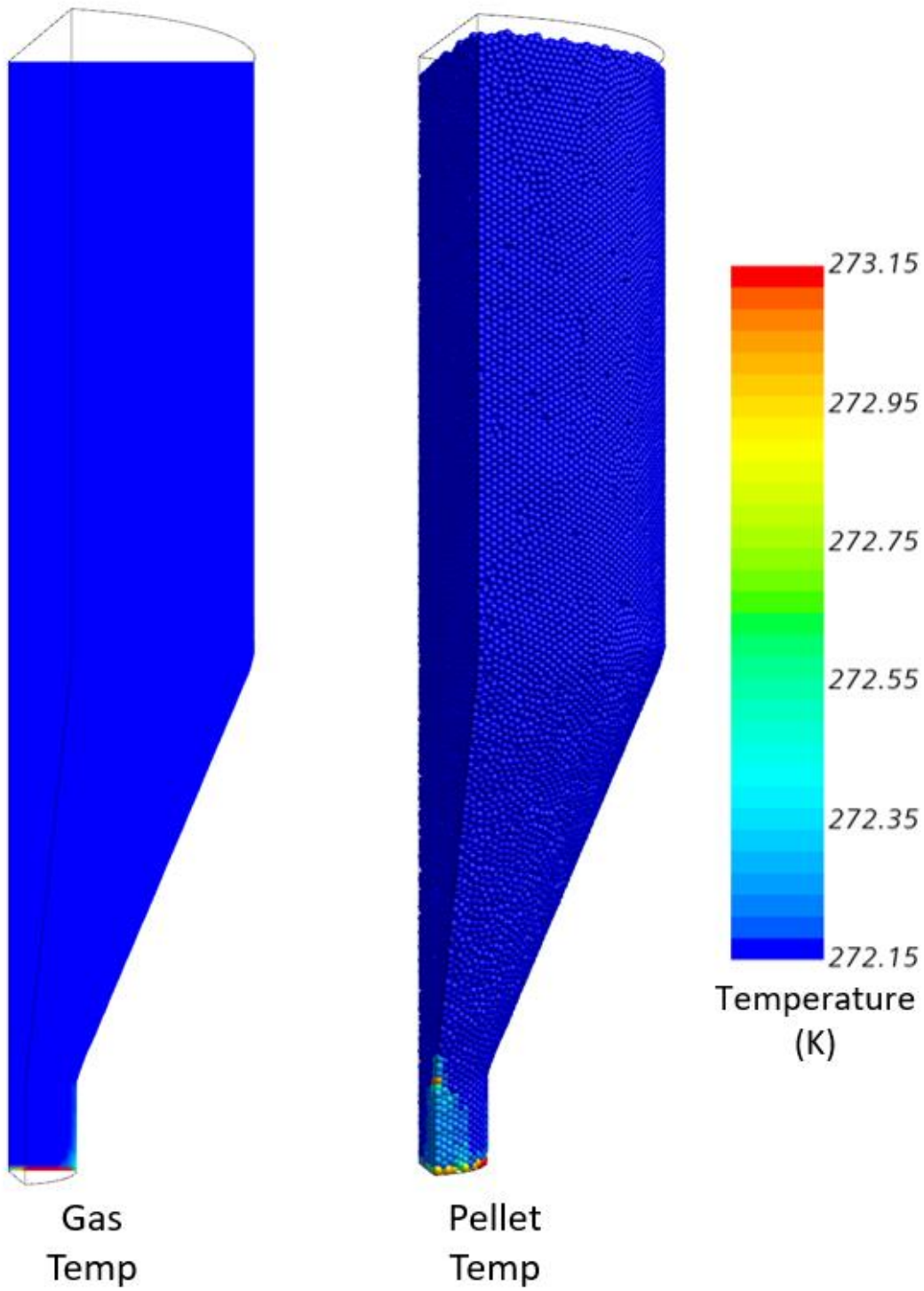

Figure 74. Thermal profile case 1 pellet temperature, no temperature profile develops through hopper

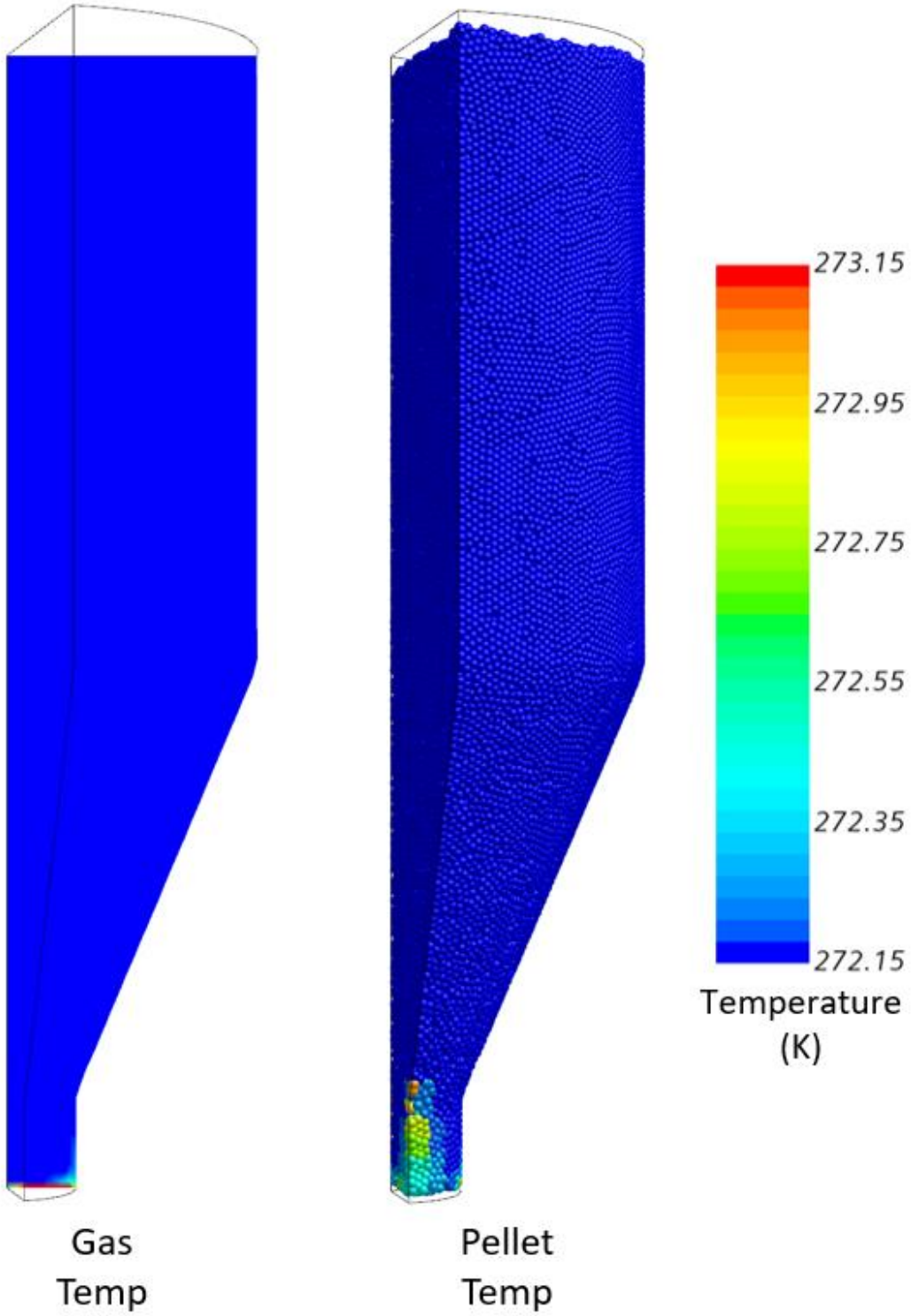

Figure 75. Thermal profile case 2 gas and pellet temperature, no temperature profile develops through the hopper

Thermal profile case 3, with the pellets resting in the domain, resulted in an average temperature of 301 K in the measured region. The temperature profile of the pellets is shown in figure 76.

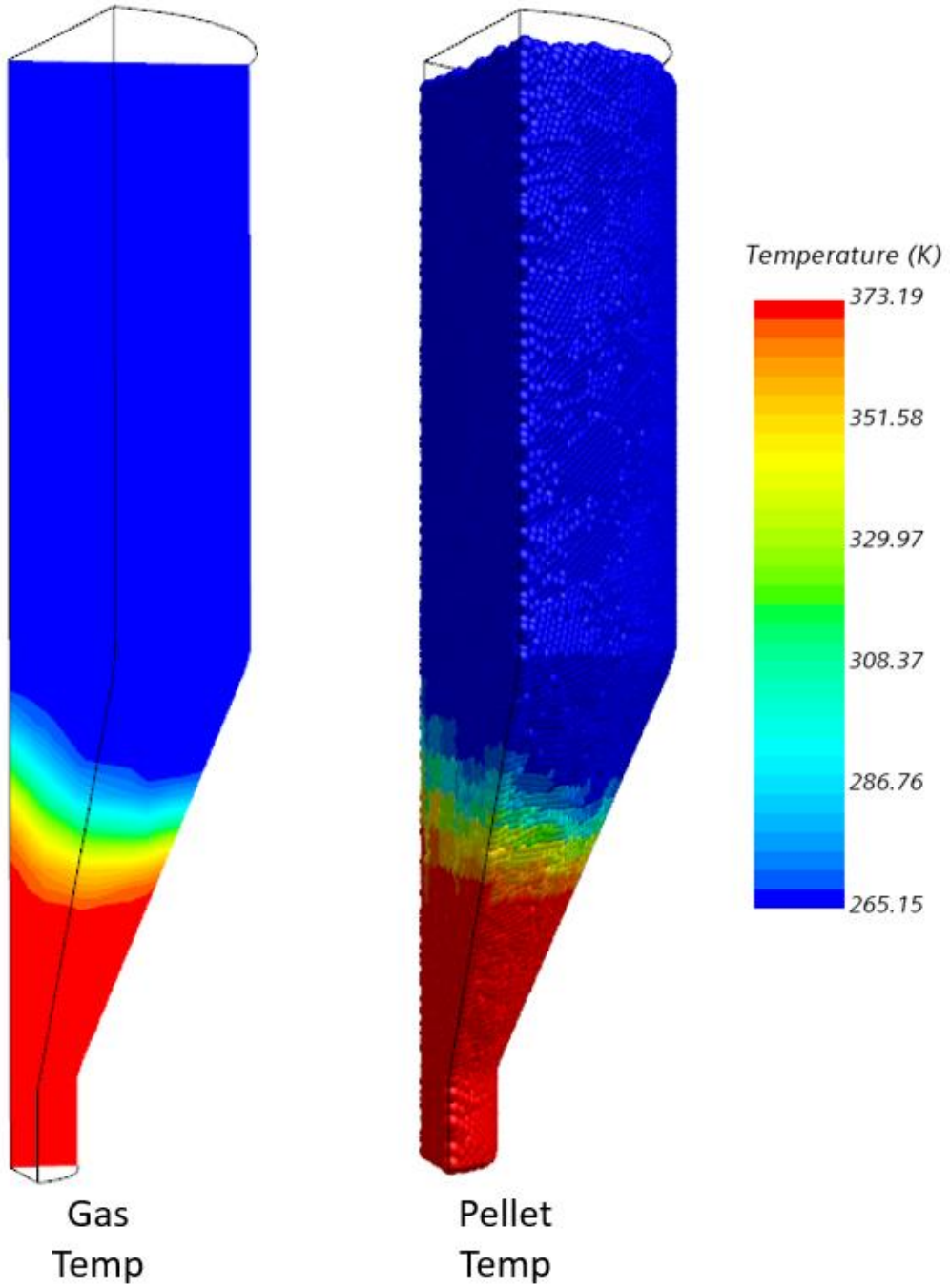

Figure 76. Thermal profile case 3 gas and pellet temperature, temperature profile develops

8.5.3 Discussion

Results for the thermal profile test cases suggest that not enough sensible heat is supplied to the pellets to create a significant thermal profile within the descending bed. This means that icy pellets that are bonded together and are charged into the hopper descend through the system without a phase change of the ice that bonds the material together, and that freezing of wet and icy pellets charged together could occur.

The results suggest that the details of the energy exchange between the gas phase and the solid phase is not a factor impacting the jamming of the flow in the feed system. The pellets charged contain 0 moisture content, and have a lower specific heat value than they would if charged with moisture, and still did not heat.

The results shift the focus of the work from modeling the heating and melting of ice in the system that potentially causes the pellets to form a blockage, to determining how much icy material can be charged before jamming of the flow occurs.

9. MINIMAL ICY/WET CHARGE TO JAM SYSTEM

9.1 Background

Iron ore pellets are stored in large quantities outside before being charged into the DRI shaft furnace feed system. The pellets are exposed to weather conditions, including wet and freezing conditions, and a mix of dry, frozen, and wet pellets are charged into the feed system.

The previous work revealed that not enough energy is supplied through the seal leg gas to produce a temperature profile within the descending bed of pellets. This suggests that the bed of wet, dry, and frozen pellets could be exposed to freezing conditions within the system, causing the pellets to freeze together.

The goal is to now determine the maximal amount of icy and wet material that can be charged before jamming occurs. Once the maximal amount is determined, the minimal percent moisture that, during freezing conditions, jams the flow is determined.

9.2 Methodology

The baseline domain is used, and the domain is filled with 3 additional DEM phases in one case (Case 1), and 6 additional phases in another case (Case 2). The 3 additional phases in case 1 are added in equal amount, so of the total additional phases each of the added phases is ~33% the total. For case 2 the additional phases are added in unequal amounts. The percent of the total additional phases of the six are 5, 10, 10, 10, 30, and 35%.

The additional DEM phases are functionally the same as the pellets, having the same properties and contact parameters, but allow for the controlling of interphase and intraphase bonding when the bond model is applied. The additional phases are charged above the flow aid insert in both cases. Both cases also have a heavy top layer of large pellets to replicate the bed of pellets above them like in the baseline and friction cases. Both cases fully charged with pellets are shown in figure 77.

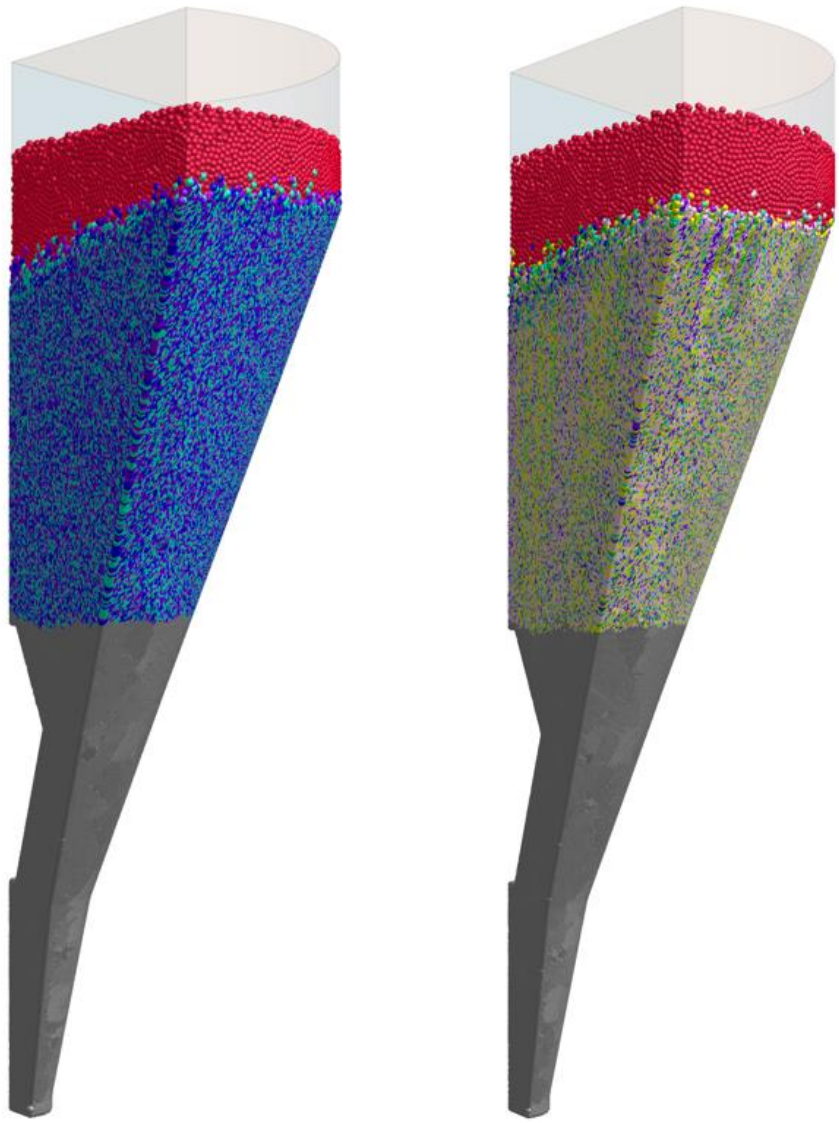

Figure 77. Filled domain of case 1 on the left and case 2 on the right

For both cases the pellets leave the domain out the bottom of the feed system at a controlled rate. Like the baseline case, the forces on the walls and flow aid insert are tracked to determine when the flow reaches steady state. After the cases reach steady state the bond model is applied to one or multiple of the pellet phases. When two pellets come into contact with the bond model applied the pair form a bond at the point of contact with a defined shear and tensile strength. The shear and tensile strength of the bond are set to the value of ice's shear and tensile strength to replicate material that is frozen together.

The amount of material that freezes together within the feed system is parameterized to determine the minimal amount of frozen and wet material that can be charged. For each parametric case three phases are defined, dry, wet, and frozen.

The phases are assigned by setting their ability to bond. Contact between two icy pellets forms a bond and contact between icy and wet pellets form a bond. All other contacts do not form bonds. Figure 78 provides a visual aid for how the defined phases bond.

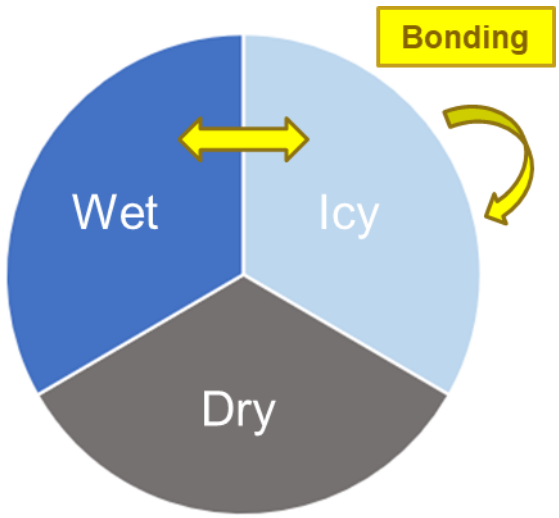

Figure 78. Visual aid for bonding, icy bonds to icy and wet material

Assuming 5.5% the mass of the icy and wet pellets is water, and the dry material contains no moisture content. The minimal amount of moisture, expressed as a percent, within the charge that may lead to jamming conditions during freezing conditions is calculated as:

$$X = 0.055\left(M_{icy} + M_{wet}\right) \tag{43}$$

Where X is the total moisture percentage of the charge, and M_{icy} and M_{wet} are the percent icy pellets and percent wet pellets respectively.

9.3 Physics Models

The Hertz-Mindlin model is used to model the forces acting on the pellets, and the bond model is applied to the pellet contacts that represent material freezing together. No energy model is applied.

The CFD solver is frozen and no drag model is applied to the pellets. The average drag force to weight ratio acting on the pellets from the baseline case was measured and found to be 9.55E-05. The drag force exerted on the pellets is small compared to the weight of the pellet, being on the order of 10^{-5}, and therefore not significant in modeling the bulk flow [51]. Previous work by Boechat et al., has shown that only modeling the solid phase using DEM is capable of predicting flow behavior of iron ore pellets within a DRI shaft furnace [54].

9.4 Pellet Properties

The pellet material properties are the same as the baseline case. The pellet contact parameters are the same as the base case except that a bond formation is introduced between pellets that are designated as icy or wet. The shear and tensile strength of the bond is set equivalent to the shear and bond strength of ice and shown in table 28.

Table 28. Bond model strength between pellets with values equivalent to ice

Bond Model Failure Strength Parameters	
Shear Strength (Pa)	**Tensile Strength (Pa)**
6E+05	7E+05

9.5 Results

Twelve scenarios are run, and 5 of the scenarios jammed the feed system, shown in table 29. The jammed system in scenarios 1 and 2 are shown in figure 79.

Table 29. Scenarios tested and results

Scenario Number	Icy (%)	Wet (%)	Jammed	Flowing
1	33.3	33.3	X	
2	33.3	0	X	
3	25	0	X	
4	15	0	X	
5	10	0		X
6	10	5	X	
7	5	0		X
8	5	10		X
9	5	20		X
10	5	30		X
11	5	40		X
12	5	95		X

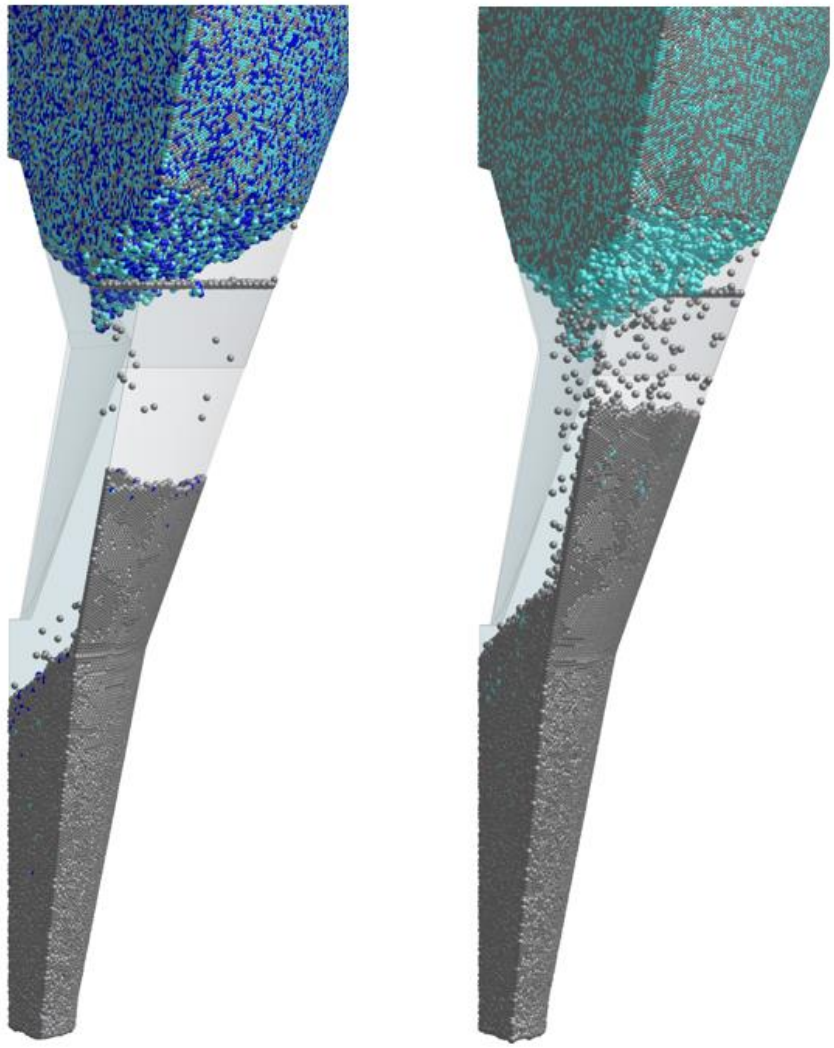

Figure 79. Jammed system for scenarios 1 (left) and 2 (right)

The maximal number of icy pellets that could be charged with dry pellets before jamming occurred was found to be 15% of the pellets. When 10% or less of the pellets are charged icy with dry the rest dry the pellets flow. The average velocity of the pellets in the upper flow aid region for 15% and 10% icy pellets are shown in figure 80.

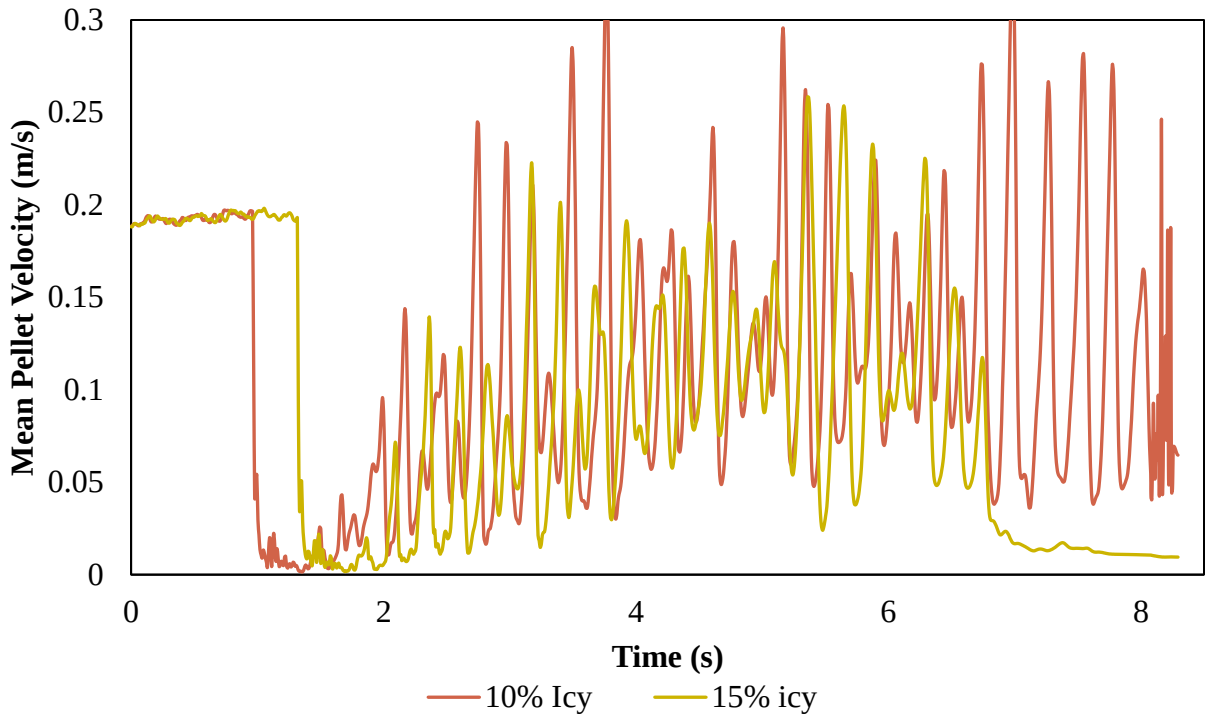

Figure 80. 15% icy pellets vs 10% icy pellets average pellet velocity vs time

When 10% of the pellets are icy and the rest of the material is dry no jamming is observed, however when 5% of the material is also wet with 10% icy charged the system jams. The average pellet velocity in the upper flow aid region between these two cases is shown in figure 81.

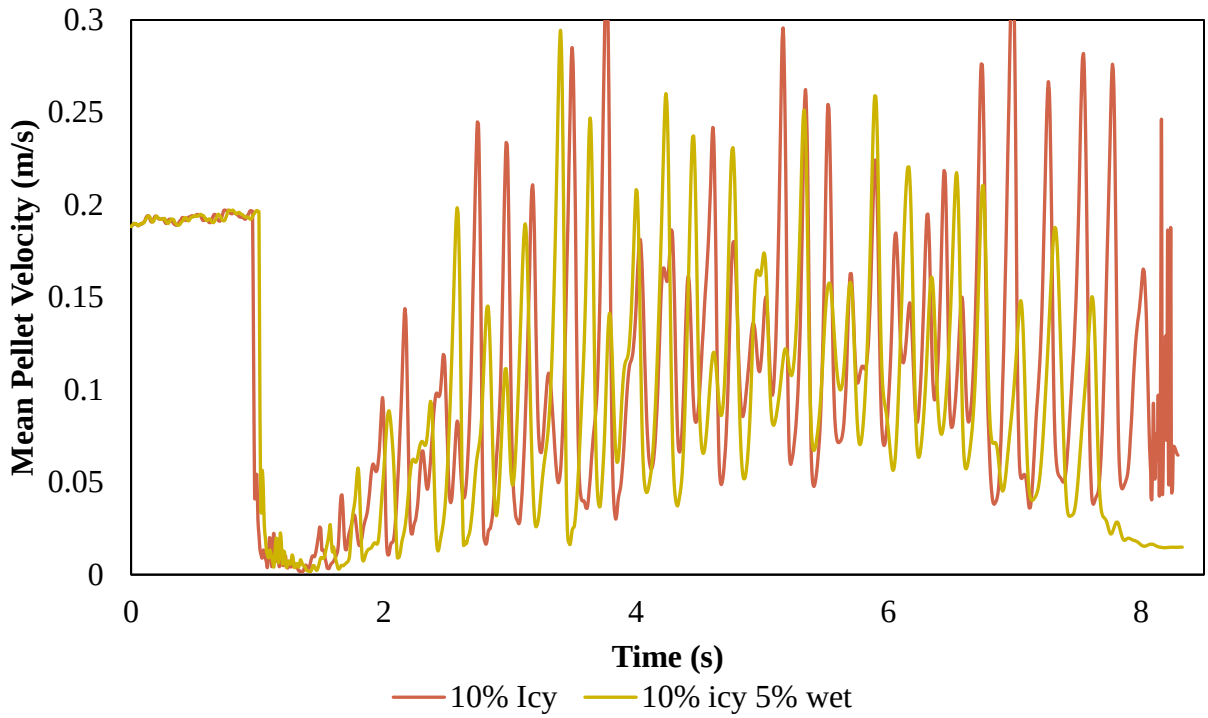

Figure 81. 10% icy pellets vs 10% icy and 5% wet pellets average pellet velocity vs time

When 5% of the pellets are frozen and charged with dry pellets the pellets flow freely. When 5% of the pellets are frozen and the remaining 95% are wet the flow also flows freely. The average velocity of the pellets in the upper flow aid region of the hopper is shown for both cases in figure 82.

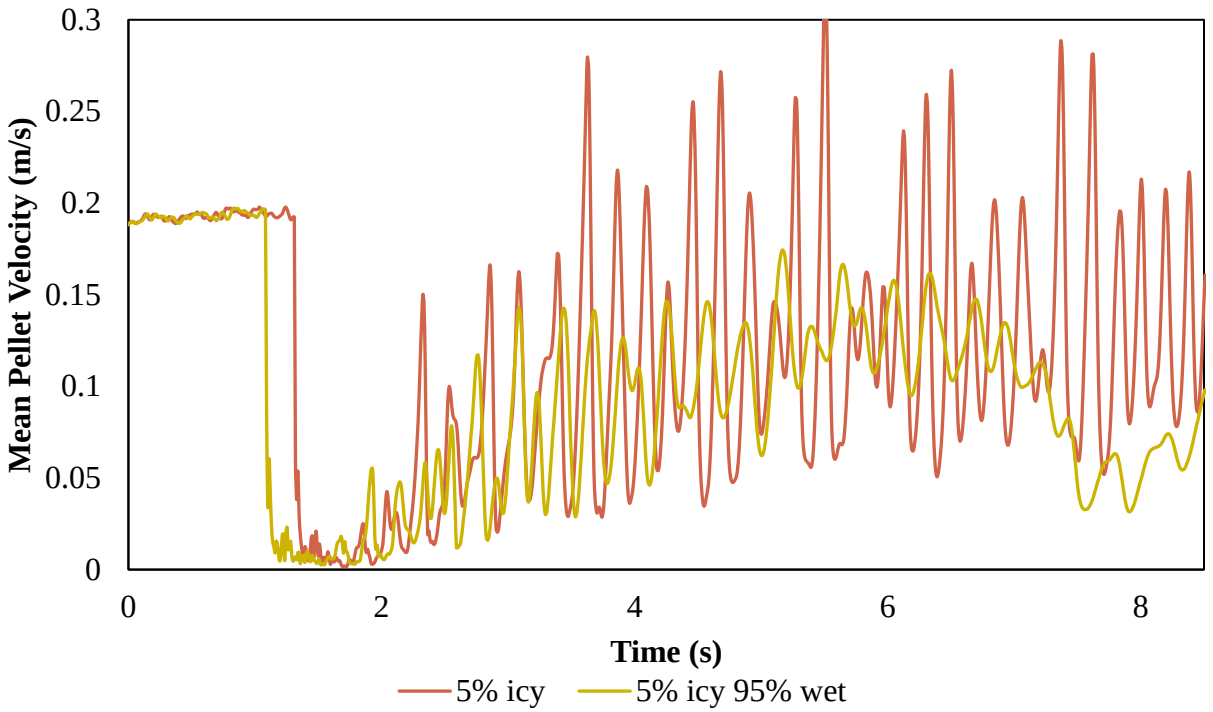

Figure 82. 5% icy pellets vs 5% icy and 95% wet pellets average pellet velocity vs time

Scenarios 4 and 6 and contained the minimal amount of ice and moisture before jamming occurred, and the percent moisture of the total charge is presented in table 30.

Table 30. Jamming scenarios and mass percent moisture of total charge

Scenario Number	Percent Icy Pellets Charged (%)	Percent Wet Pellets Charged (%)	Mass Percent Moisture of Total Charge (%)
4	15	0	0.825
6	10	5	0.825

9.6 Discussion

The work here shows that a plausible reason the feed system is jamming during winter operation is because the pellets are freezing together at a certain moisture level.

The lowest percent of icy pellets charged with dry pellets into the hopper that jams the flow was found to be 15%. When 10% of the pellets are icy and the rest dry the pellets flow. However,

when 5% of the pellets are wet along with the 10% icy jamming occurs. When 5% of the pellets are icy the flow does not jam, even if the other 95% is wet.

The minimal amount of moisture expressed as a percent within the charged pellets that may lead to jamming was found to be 0.825%. This number may not be useful to operators given that the value is low and the distribution of the moisture matters. The moisture distribution assumption is that the dry material is completely dry, and that the icy and wet are completely soaked. Independent of these assumptions, measuring weather or not 0.825 the mass of the charge is water may be challenging. A better metric may simply be what percent of the material is soaked and frozen. In both cases the minimal amount of soaked material was 15% of the pellets, with at least 2/3 of the pellets frozen to jam the flow.

The findings here may be limited as there is no experimental data to compare too. Because of the lack of experimental work many assumptions are made. For example, the strength of the bonds between pellets are assumed to be as strong as ice, and if that is not the case, it would be expected that the minimal amount of icy and wet pellets to jam the flow would change. Another assumption is that all of the contacts between pellets that have the potential to freeze do freeze every time. This may be a reasonable assumption for performing simulation work, but without experimental work showing how much material freezes together, to replicate and calibrate the simulations to, that cannot be known. Icy material could easily hold more or less water as the water is in a solid phase and could be attached to the surface of the pellet, and wet pellets may not need to be holding the maximum amount of moisture to freeze together, so the assumption that icy and wet pellets are holding 5.5% their mass is also limited without some experimental work.

10. DISCUSSION AND CONCLUSIONS

The bulk flow behavior of the iron ore pellets can be represented using spherical DEM particles through calibration of the friction coefficients. The prohibitive computational expense of modeling the entire feed system can be mitigated by modeling the pellets with a uniform diameter distribution at 1.45x the average pellet diameter, and through the implementation of symmetry boundary conditions. These conditions reduce the computational expense by 98.7% while maintaining the relevant flow field variables with respect to jamming, which deviated from the baseline valued by approximately 5%.

Simulation of the baseline operating conditions, which implemented the calibrated friction coefficients and the conditions that lowered computational expense, showed that the simulation region most likely to experience jamming of the flow agreed with where the jam is reportedly occurring. The effect of moisture was modeled and compared to the baseline, assuming that the bulk effect of moisture in the flow is an increase resistance to shear forces, and no jamming was reported. When considering that the system is exposed to moisture year-round, and that the jam occurs only in the winter, the results indicate that moisture is not likely the sole cause of jamming.

Development of a thermal model revealed that not enough heat is supplied by the counterflowing gas to heat the pellets in freezing conditions, suggesting that pellets are exposed to freezing conditions within the feed system during operation. Modeling to determine the minimal amount of icy and wet pellets that can be charged showed that a maximum of 15% icy pellets can be charged, or 10% icy with a maximum of 5% wet pellets, before jamming occurs. The minimal amount of moisture in the charged pellets to jam the flow is 0.825% the mass of the pellets, assuming the icy and wet pellets hold the maximum 5.5% moisture content and the dry pellets contain 0% moisture. The minimal amount of moisture in the total charge to cause jamming may not be useful to operators given those assumptions, and rather focusing on what percent is icy and wet may be more useful, which was found to be 15% of the pellets, assuming 2/3 the pellets are frozen.

The results of this study are limited by lack of data and experimental work. No literature could be found on the freezing of iron ore pellets or the moisture effect on the bulk flow of pellets at the time of this writing. To improve the simulations and validate simulation results, it is recommended that experimental work be carried out to determine the strength of the bonds

between frozen pellets and how much moisture is necessary for them to form. Along with experimental work to determine what percent of pellets freeze together and in what conditions. Work to determine how moisture impacts bulk flow of pellets with and without fines, and how moisture content impacts contact parameters between pellets and steel is also recommended.

REFERENCES

[1] International Energy Agency. *Iron and Steel Technology Roadmap*, IEA Publications, 2020 https://iea.blob.core.windows.net/assets/eb0c8ec1-3665-4959-97d0-187ceca189a8/Iron_and_Steel_Technology_Roadmap.pdf (Accessed: March 13, 2023)

[2] Pardo, Nicolás, and José Antonio Moya. "Prospective scenarios on energy efficiency and CO2 emissions in the European Iron & Steel industry." *Energy* 54 (2013): 113-128.

[3] Fan, Zhiyuan, and S. Julio Friedmann. "Low-carbon production of iron and steel: Technology options, economic assessment, and policy." *Joule* 5.4 (2021): 829-862.

[4] Lu, L., J. Pan, and D. Zhu. "Quality requirements of iron ore for iron production." *Iron Ore*. Woodhead Publishing, 2015. 475-504.

[5] Midrex, https://www.midrex.com/wp-content/uploads/MidrexSTATSBook2021.pdf *World Direct Reduction Statistic.* (Accessed: March 13, 2023)

[6] International Iron Metallics Association "*The use of Hot Briquetted Iron (HBI) in the Blast Furnace (BF) for Hot Metal Production*" https://www.metallics.org/assets/files/Public-Area/Fact-Sheets/_4_HBI_in_BF_Fact_Sheet_-Rev3.pdf (Accessed: March 13, 2023)

[7] Midrex, https://www.midrex.com/technology/midrex-process/midrex-h2/ (Accessed: March 13, 2023)

[8] Petrich, Chris, et al. "Heat Transfer in a Bed of Dry Iron Ore Pellets." *ISIJ international* 53.4 (2013): 723-725.

[9] Goel, R. K., and Bhawani Singh. *Engineering rock mass classification: tunnelling, foundations and landslides*. Elsevier, 2011.

[10] Lanzerstorfer, C., and M. Hinterberger. "Influence of the Moisture Content on the Flowability of Fine-Grained Iron Ore Concentrate." *International Journal of Chemical and Molecular Engineering* 11.3 (2017): 265-268.

[11] Current Results https://www.currentresults.com/Weather/US/average-state-temperatures-in-winter.php (Accessed: March 13, 2023)

[12] Ketterhagen, William R., et al. "Predicting the flow mode from hoppers using the discrete element method." *Powder technology* 195.1 (2009): 1-10.

[13] A.W. Jenike, Bulletin 108: Gravity flow of bulk solids. Salt Lake City, UT, October 1961.

[14] Xiao, Yawen, et al. "Research on clogging mechanisms of bulk materials flowing through a bottleneck." *Powder Technology* 381 (2021): 381-391.

[15] Park, Su-San, and Eung Soo Kim. "Jamming probability of granular flow in 3D hopper with shallow columns: DEM simulations." *Granular Matter* 22.4 (2020): 1-13.

[16] D. Gella, D. Maza, I. Zuriguel, Role of particle size in the kinematic properties of silo flow, Phys. Rev. E 95 (5–1) (2017) 52904.

[17] A.V.K. Reddy, S. Kumar, K.A. Reddy, J. Talbot, Granular silo flow of inelastic dumbbells: clogging and its reduction, Phys. Rev. E 98 (2) (2018)https://doi.org/10. 1103/physreve.98.022904.

[18] E. Goldberg, C. Manuel Carlevaro, L.A. Pugnaloni, Clogging in two-dimensions: effect of particle shape, J. Stat. Mech. 2018 (11) (2018) 113201, https://doi.org/10.1088/ 1742-5468/aae84b.

[19] A. Ashour, S. Wegner, T. Trittel, T. Börzsönyi, R. Stannarius, Outflow and clogging of shape-anisotropic grains in hoppers with small apertures, Soft Matter 13 (2) (2017) 402–414, https://doi.org/10.1039/c6sm02374f.

[20] A. Ashour, T. Trittel, T. Borzsonyi, Silo outflow of soft frictionless spheres, Phys.Rev. Fluids 2 (12) (2017)https://doi.org/10.1103/PhysRevFluids.2.123302.

[21] M. Zaki, M.S. Siraj, Study of a flat-bottomed cylindrical silo with different orifice shapes, Powder Technol. 354 (2019) 641–652, https://doi.org/10.1016/j.powtec. 2019.06. 041.

[22] D. Lopezrodriguez, D. Gella, K. To, D. Maza, A. Garcimartin, I. Zuriguel, Effect of hopper angle on granular clogging, Phys. Rev. E 99 (3) (2019)https://doi.org/10.1103/ physreve.99.032901.

[23] S. Mondal, M.M. Sharma, Role of flying buttresses in the jamming of granular matter through multiple rectangular outlets, Granul. Matter 16 (1) (2014) 125–132.

[24] R. Arevalo, I. Zuriguel, Clogging of granular materials in silos: effect of gravity and outlet size, Soft Matter 12 (1) (2016) 123–130, https://doi.org/10.1039/c5sm01599e.

[25] C.C. Thomas, D.J. Durian, Geometry Dependence of the Clogging Transition in Tilted Hoppers, 2013 87, https://doi.org/10.1103/PhysRevE.87.052201.

[26] E. Gallego, J.M. Fuentes, J. Wiącek, J.R. Villar, F. Ayuga, DEM analysis of the flow and friction of spherical particles in steel silos with corrugated walls, Powder Technol. 355 (2019) 425–437, https://doi.org/10.1016/j.powtec.2019.07.072.

[27] Liu, Hanru, et al. "Numerical analysis of the effect of the contraction rate of the curved hopper on flow characteristics of the silo discharge." *Powder Technology* 356 (2019): 858-870.

[28] D. Gella, D. Maza, I. Zuriguel, A. Ashour, R. Arévalo, R. Stannarius, Linking bottleneck clogging with flow kinematics in granular materials: the role of silo width, Phys. Rev. Fluids 2 (8) (2017) 1–11, https://doi.org/10.1103/PhysRevFluids.2.084304.

[29] T. Borzsonyi, E. Somfai, B. Szabo, S. Wegner, P. Mier, G. Rose, R. Stannarius, Packing, alignment and flow of shape-anisotropic grains in a 3D silo experiment, New J. Phys. 18 (9) (2016) 93017, https://doi.org/10.1088/1367-2630/18/9/093017.

[30] Zuriguel, I., Pugnaloni, L.A., Garcimartín, A., Maza, D.: Jamming during the discharge of grains from a silo described as a percolating transition. Phys. Rev. E 68, 030301 (R) (2003)

[31] . Zuriguel, I., Garcimartín, A., Maza, D., Pugnaloni, L.A., Pastor, J.M.: Jamming during the discharge of granular matter from a silo. Phys. Rev. E 71, 051303 (2005)

[32] Janda, A., Zuriguel, I., Garcimartín, A., Pugnaloni, L.A., Maza, D.: Jamming and critical outlet size in the discharge of a twodimensional silo. EPL 84(4), 44002 (2008)

[33] Sperl, M.: Experiments on corn pressure in silo cells—translation and comment of Janssen's paper from 1895. Granul. Matter 8(2), 59–65 (2006)

[34] Lu, Kevin, Emily E. Brodsky, and H. Pirouz Kavehpour. "A thermodynamic unification of jamming." *Nature Physics* 4.5 (2008): 404-407.

[35] Sen, Maitraye, et al. "A multi-scale hybrid CFD-DEM-PBM description of a fluid-bed granulation process." *Processes* 2.1 (2014): 89-111.

[36] Thakur, Subhash C., Jin Y. Ooi, and Hossein Ahmadian. "Scaling of discrete element model parameters for cohesionless and cohesive solid." *Powder Technology* 293 (2016): 130-137.

[37] Natsui, Shungo, et al. "Gas–solid flow simulation of fines clogging a packed bed using DEM–CFD." *Chemical engineering science* 71 (2012): 274-282.

[38] Zhu, H. P., et al. "Discrete particle simulation of particulate systems: a review of major applications and findings." *Chemical Engineering Science* 63.23 (2008): 5728-5770.

[39] Kinaci, M. E., T. Lichtenegger, and S. Schneiderbauer. "A CFD-DEM model for the simulation of direct reduction of iron-ore in fluidized beds." *Chemical Engineering Science* 227 (2020): 115858.

[40] El-Emam, Mahmoud A., et al. "Theories and applications of CFD–DEM coupling approach for granular flow: A review." *Archives of Computational Methods in Engineering* (2021): 1-42.

[41] Che, Hanqiao, et al. "PEPT validated CFD-DEM model of aspherical particle motion in a spouted bed." *Chemical Engineering Journal* 453 (2023): 139689

[42] Wang, Shuai, et al. "CFD-DEM simulation of heat transfer in fluidized beds: Model verification, validation, and application." *Chemical Engineering Science* 197 (2019): 280-295.

[43] Markauskas, D., et al. "Comparative study on mesh-based and mesh-less coupled CFD-DEM methods to model particle-laden flow." *Powder Technology* 305 (2017): 78-88.

[44] Patil, Amit V., et al. "A study of heat transfer in fluidized beds using an integrated DIA/PIV/IR technique." *Chemical Engineering Journal* 259 (2015): 90-106.

[45] Di, Shaocheng, et al. "Discrete element simulation of ice loads on narrow conical structures." *Ocean Engineering* 146 (2017): 282-297.

[46] Jou, Oriol, et al. "A bonded discrete element method for modeling ship–ice interactions in broken and unbroken sea ice fields." *Computational Particle Mechanics* 6 (2019): 739-765.

[47] Siemens Digital Industries Software. Simcenter STAR-CCM+, version 2021.3. In *Contact Force*, Seimens, 2021.

[48] Zhou, ZYa, A. B. Yu, and Paul Zulli. "Particle scale study of heat transfer in packed and bubbling fluidized beds." *AIChE Journal* 55.4 (2009): 868-884.

[49] Volk, Annette. *Quantification and Assessment of Numerical Error in Coupled Computational Fluid Dynamics-Discrete Element Method Simulations of Gas Flow through Granular Solids*. Diss. University of Cincinnati, 2018.

[50] Li, Chengzhi, et al. "The angle of repose and size segregation of iron ore granules: DEM analysis and experimental investigation." *Powder Technology* 320 (2017): 257-272.

[51] Nott, Prabhu, and S. Sundaresan. “1.2.2 Liquid Bridge or Capillary Forces.” *An Introduction to Granular Flow*, Cambridge Univ. Press, New York, 2008, pp. 14–15, 36-40.

[52] Härtl, Johannes, and Jin Y. Ooi. "Numerical investigation of particle shape and particle friction on limiting bulk friction in direct shear tests and comparison with experiments." *Powder Technology* 212.1 (2011): 231-239.

[53] Rao, Vandana. "Thermal conductivity and diffusivity of iron ore pellet having low porosity." *ISIJ international* 42.7 (2002): 800-802.

[54] Boechat, Fernando O., Rodrigo M. de Carvalho, and Luís Marcelo Tavares. "Simulation of mechanical degradation of iron ore pellets in a direct reduction furnace." *KONA Powder and Particle Journal* 35 (2018): 216-225.